Sensor and actuator selection for feedback control of fluid flows

by

Stephan Friedrich Oehler

Submitted in total fulfilment of the requirements
of the degree of Doctor of Philosophy

October 2019

Department of Mechanical Engineering

UNIVERSITY OF MELBOURNE

Abstract

The present thesis regards linear estimation and control for two fluid flows, with a particular focus on the placement of sensors and actuators. In the first part of the thesis, we study the complex Ginzburg-Landau equation, a simple model for spatially developing flows such as jets, wakes and cavities. (This equation can be seen as a low-dimensional substitute for the Navier-Stokes equations.) The specific focus is on the extent to which estimation and control are (i) fundamentally difficult and (ii) limited by having only a single sensor and a single actuator. To answer these questions, we study three problems. First, we consider the optimal estimation problem in which a single sensor is used to estimate the entire flow field (without any control). Second, we consider the full information control problem in which the whole flow field is known, but only a single actuator is available for control. Third, we consider the overall input-output control problem in which only a single sensor is available for measurements; and only a single actuator is available for control. By considering the optimal sensor placement, optimal actuator placement or both while varying the stability of the system, fundamental placement trade-offs are made clear. We discuss implications for effective feedback control with a single sensor and a single actuator and compare the results to previous placement studies. In the second part of this thesis, we look at an incompressible turbulent channel flow at a friction Reynolds number of $\mathrm{Re}_\tau = 2000$. A linear Navier-Stokes operator is formed about the turbulent mean and augmented with an eddy viscosity. Velocity perturbations are then generated by stochastically forcing the linear Navier-Stokes operator. The objective is to estimate and control these perturbations. The estimation and control problems perform best for the largest scales that (i) are high in energy when stochastically forced, (ii) exhibit large transient growth and (iii) are coherent over large wall-normal distances. We determine the locations of sensors and actuators for which estimation and control are most effective by looking at two arrangements: (i) placing them at the wall; and (ii) placing them some distance off the wall. Finally, it is shown that a control arrangement with a well-placed sensor and actuator performs comparably to either measuring the flow everywhere (while actuating it at a single wall height) or actuating it everywhere (while measuring it at a single wall height). In this way, we gain insight (at low computational cost) into how specific scales of turbulence are most effectively estimated and controlled.

Declaration of Authorship

I hereby declare that except where specific reference is made to the work of others, the contents of this dissertation are original towards the total fulfilment for the Degree of Doctor of Philosophy and have not been submitted in whole or in part for consideration for any other degree or qualification in this, or any other university. This dissertation is my own work and contains nothing which is the outcome of work done in collaboration with others, except as specified in the text and Acknowledgements. This dissertation contains fewer than 100,000 words including appendices, bibliography, footnotes, tables and equations.

Stephan F. Oehler
October 2019

Preface

The format of this document is *thesis with publication*[1]. It contains submitted and published articles as individual chapters.

The outcomes of **chapter 3** have been previously published in the following article:
Oehler S. F. and Illingworth, S. J. (2018), 'Sensor and actuator placement trade-offs for a linear model of spatially developing flows', *J. Fluid Mech.* **854**, 34–55.

Early results of this article were published in:
Oehler, S., Ooi, A. and Illingworth, S. J. (2016), 'Actuator and sensor selection for feedback control of the linearised Ginzburg-Landau equation', *in* '20th Australasian Fluid Mechanics Conference', AFMS.

The outcomes of **chapter 4** have been previously published in the following peer-reviewed proceedings:
Oehler, S., Garcia-Gutiérrez, A. and Illingworth, S. (2018), 'Linear estimation of coherent structures in wall-bounded turbulence at $\mathrm{Re}_\tau = 2000$', *J. Phys. Conf. Ser.* **1001**, 012006.

Most of the outcomes of **chapter 5** have been previously published in the following peer-reviewed conference proceedings:
Oehler, S. F., and Illingworth, S. J. (2018), 'Linear estimation and control of coherent structures in wall-bounded turbulence at $\mathrm{Re}_\tau = 2000$', *in* '21st Australasian Fluid Mechanics Conference', AFMS.

The outcomes of **chapter 6** are in the following article submitted for publication to *Physical Review Fluids*:
Oehler, S. F., and Illingworth, S. J. (2019), 'Linear control of coherent structures in wall-bounded turbulence at $\mathrm{Re}_\tau = 2000$', *in* 'arXiv preprint arXiv:1906.07462'.

I am the first author of all the publications listed above and contributed more than 80% of the content of the publications. Chapters 4 and 6 are written in American English because they are either published or under review in American Journals. All other chapters are written in British/Australian English. There is an overlap in the method sections of chapters 3-6, but redundant method sections are not removed because chapters 3-6 are based on independent publications. Chapter 5 contains extra results that are not included in the original publication it is based on.

[1] In accordance with the University of Melbourne's Graduate Research Training Policy (MPF1321).

This research was primarily funded by the University of Melbourne Graduate Research Scholarships. Attendance at various conferences during the creation of this thesis was supported by the Australian Research Council, The University of Melbourne and the European Research Council:

1. 20th Australasian Fluid Mechanics Conference in Perth, Australia (2016)
2. Third Madrid Turbulence Summer School at the Polytechnic University of Madrid, Spain (2017)
3. 70th Annual Meeting of the American Physical Society Division of Fluid Dynamics in Denver, United States (2017)
4. 56th IEEE Conference on Decision and Control in Melbourne, Australia (2017)
5. 12th European Fluid Mechanics Conference in Vienna, Austria (2018)
6. 21st Australasian Fluid Mechanics Conference in Adelaide, Australia (2018)
7. 9th European Postgraduate Fluid Dynamics Conference in Ilmenau, Germany (2019)

Acknowledgements

I want to first and foremost acknowledge and thank my supervisor Dr Simon Illingworth for his time, guidance and patience during my PhD, for which I will always be grateful. By setting high standards while also providing excellent support, Simon has helped me grow as a researcher, academic writer and as a person. Giving me the opportunity to attend many conferences has developed my communication and networking skills tremendously and broadened my horizon. I would also like to thank my other advisor Prof Andrew Ooi, as well as my committee members A/Prof Daniel Chung and Dr Jimmy Philip for their support. Another thank you goes to the professional staff at the University of Melbourne, including Carolyn Barrie, Jan May, Christine Selby, Kim Robinson, and many others. A special thanks to all the members of the Fluid Mechanics Research Group for their feedback, especially Anagha Madhusudanan, Dr Sean Symon, Jiwen Gong, Dr Reza Abbassi and Bo Jin.

During the second year of my PhD, I had the opportunity to attend the Third Madrid Turbulence Workshop at Polytechnic University of Madrid (UPM) for five weeks. Attending this workshop was one of the highlights of my PhD. The hospitality and support in Madrid were incredible, giving my research a significant boost. Thank you to Prof Javier Jiménez, Dr Adrián García–Gutiérrez, Aurora García–Sarrión and everybody else who was involved in the workshop's organisation.

Thank you to my undergraduate supervisors at the University of Bristol and the University of Melbourne Dr Kazem Alemzadeh, A/Prof Denny Oetomo, Dr Shou Han Zhou and Prof Bruce Drinkwater.

Many people in my personal life have guided and encouraged me during my PhD studies. First of all, I need to thank my sister Annalisa and my parents Helmuth and Annette for always supporting, championing and believing in me. I also want to thank Rabbi Dr Aviva Kipen, Peter Kubas, Claire Baxter, Leo Zennon and all my friends. They have given me inspiration and much-needed encouragement during my studies at University.

Finally, I would like to thank three important people who have laid the groundwork for this PhD journey: Andrew Pomeroy and Mark Campion, my math teachers in Dublin; and Dr Volker Wipprecht, who recognised my mathematical abilities when I was 15 years old.

Contents

List of Tables

List of Figures

Chapter 1

Introduction

1.1 Background and motivation

Manipulating a fluid flow towards a desired behaviour is known as flow control. Tasks in flow control include the reduction of drag, improvement of lift, delay of vortex shedding, suppression of noise and the enhancement of mixing. For example, in the transport industry, flow control has the potential to save fuel and increase vehicular speeds. Annually, the ocean shipping, airline and trucking industries consume 2.1 billion, 1.5 billion and 1.2 billion barrels of oil respectively. A reduction of fuel consumption by flow control of 1/3 could result in savings of $160 billion annually (based on $100 per barrel) (Kim and Bewley, 2007; Kim, 2011; McKeon et al., 2013; Luhar et al., 2014).

The history of flow control, which has existed for millennia, is described by Gad-el-Hak (Gad-el-Hak, 1996; Gad-el Hak, 2001; Gad-el-Hak et al., 2003). The science of flow control originates with Prandtl (1904) who, while introducing boundary layer theory, conducted experiments in which he controlled boundary layers. Today, flow control theory is split up into passive and active manipulation of a flow (figure 1.1).

In passive flow control, we manipulate a flow without using any energy. There are two types of passive control:

(i) *Open-loop passive control*, where we favourably alter the geometry of the flow or some property of the flow itself. Historical examples of passive open-loop control include boomerangs, streamlined spears and fin-stabilised arrows (Gad-el-Hak, 1996). Modern examples include the addition of heavy polymers (Lumley,

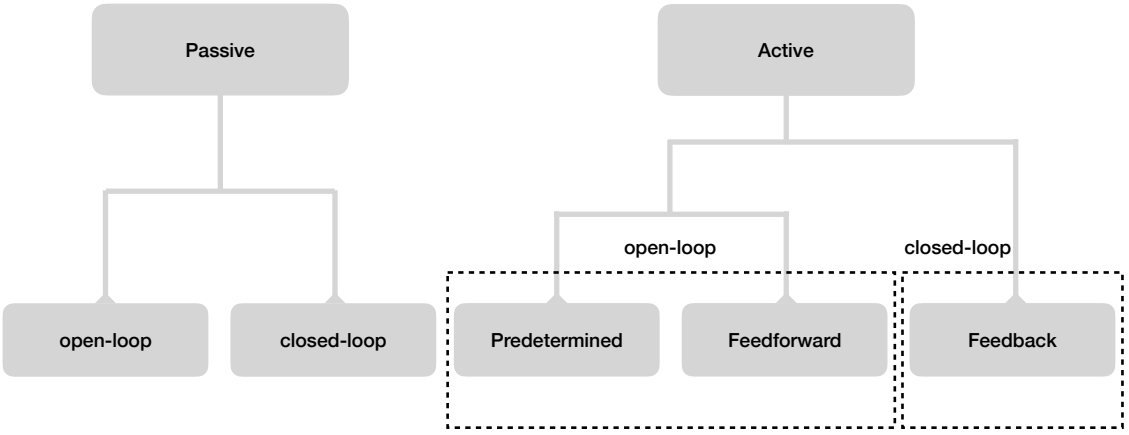

FIGURE 1.1: Overview: flow control.

1973; White and Mungal, 2008) into a flow and riblets (Walsh, 1983; García-Mayoral and Jiménez, 2011).

(ii) *Closed-loop passive control*, where we employ a compliant surface or object which deforms in response to the action of the flow and in turn alters the behaviour of the flow (Luhar et al., 2015). An example of passive closed-loop control is pliable skin (Lang et al., 2008).

In active flow control, we manipulate the flow with energy-consuming actuators that are driven by controllers. There are three types of active control (Gad-el-Hak, 1996).

(i) *Predetermined open-loop control*, where an actuator with predetermined settings forces a flow blindly. This technique is prone to both uncertainties in the flow and modelling errors. An example is boundary layer suction at the wall (Antonia et al., 1995).

(ii) *Feedforward open-loop control*, where a controller drives an actuator based on measurements (usually taken upstream of the actuator). The controller responds to the measurements, but in a predetermined way and as a consequence, cannot correct itself. This technique considers the state of the flow but does not compensate for modelling errors. An example is open-loop control in turbulent boundary layers utilising synthetic jet actuators and shear sensors (Rathnasingham and Breuer, 2003).

(iii) *Feedback closed-loop control*, where a controller drives an actuator based on measurements relative to a reference (the measurements are usually taken downstream of the actuator). This technique considers the state of the flow and provides robustness to modelling errors. An example is the delay of vortex shedding behind a bluff body (Choi et al., 2008).

One of the great challenges in flow control is the high dimensionality of most fluid-flow problems. McKeon et al. (2013) approximated (based on assumptions by Gad-el Hak (2006)) that to suppress all near-wall streaks for an Airbus A380 one would require 20×10^6 micro-sensors and -actuators, which is comparable to the number of neurons in a human brain (Herculano-Houzel, 2009). As a result, it is impractical to apply flow control at this scale in the foreseeable future due to the high manufacturing cost, the manufacturing challenges and the high-frequency requirements of the sensors and actuators. Additionally, the computational load of the controller for set-ups at this scale can also pose a challenge but could potentially be overcome by de-centralised control.

As a consequence, current flow control problems focus on modelling and controlling the most pertinent flow features to lower the dimensionality of the problem significantly. For free shear problems, such as the cylinder wake, control schemes exist which target the dynamic behaviour of a recurring process such as limit cycles and bifurcations (Gillies, 1998). For wall-bounded problems, such as the channel flow, control schemes exist which only consider large structures that can be captured by a low-resolution model (typically of order $N \in 10^2$) (Bewley and Liu, 1998; Kim and Bewley, 2007). Feedback control is the best choice when utilising low-order approximate models as it has a degree of robustness to modelling errors.

The design process of model-based feedback controllers considers six components (figure 1.2): (i) sensors, (ii) actuators, (iii) a model of the flow, (iv) a model of the flow's uncertainties (v) the control objective, (vi) and the controller itself.

(i) *Sensors* measure the flow state and provide feedback to the controller. Measurable quantities include shear stress, pressure, temperature and velocity (Cattafesta III and Sheplak, 2011).

(ii) *Actuators* force the flow based on instructions the controller provides. Examples of actuation include oscillations (displacement), blowing and suction

(mass and momentum), sound and body forces (Cattafesta III and Sheplak, 2011).

(iii) *Flow model:* the design of model-based feedback controllers requires a representation of the flow dynamics. Preferably, a linear model is used to enable the whole range of control tools (Taira et al., 2017).

(iv) *Uncertainty model:* the flow model will behave according to a set of external uncertainties. Hence, to design and simulate the feedback control loop, we require a representation of the uncertainty model. Examples of uncertainties include uncertain disturbances, sensor noise and a mismatch between the flow model and the flow itself.

(v) *Objectives* in flow control include the reduction of drag (e.g. to increase the flow rate in a pipeline), the reduction of skin friction at the wall (e.g. to create faster, more efficient vehicles), and the delay of transition (Gad-el Hak, 2001; Brunton and Noack, 2015). A common way to mathematically represent and quantify a control objective is with a cost function.

(vi) *Controller:* its design, behaviour and performance depend on the control objective, the flow and uncertainty models, the sensors and the actuators employed. Examples of model-based controllers include $\mathcal{H}_2$-optimal and $\mathcal{H}_\infty$ control, dynamic phasors, adjoint methods, and model predictive control (Bewley, 2001; Bewley et al., 2001; Kim and Bewley, 2007; Brunton and Noack, 2015).

Most of the literature on feedback flow control focuses on improving the design process incrementally. However, there is a notable paucity of studies that seek to identify the limits of a given type of control set-up. Some set-ups, no matter how well we design a controller, cannot be controlled effectively due to fundamental limitations of the set-up (Stein, 2003). These limitations can be imposed by the sensors, by the actuators or by the flow itself. Some of these constraints may be improved upon in the future with advanced technology, but most of them cannot.

1.2 This study

In this study, we seek to identify the limits of feedback control for two convection-dominated flows: (i) a free-shear flow in the laminar-transitional regime (complex

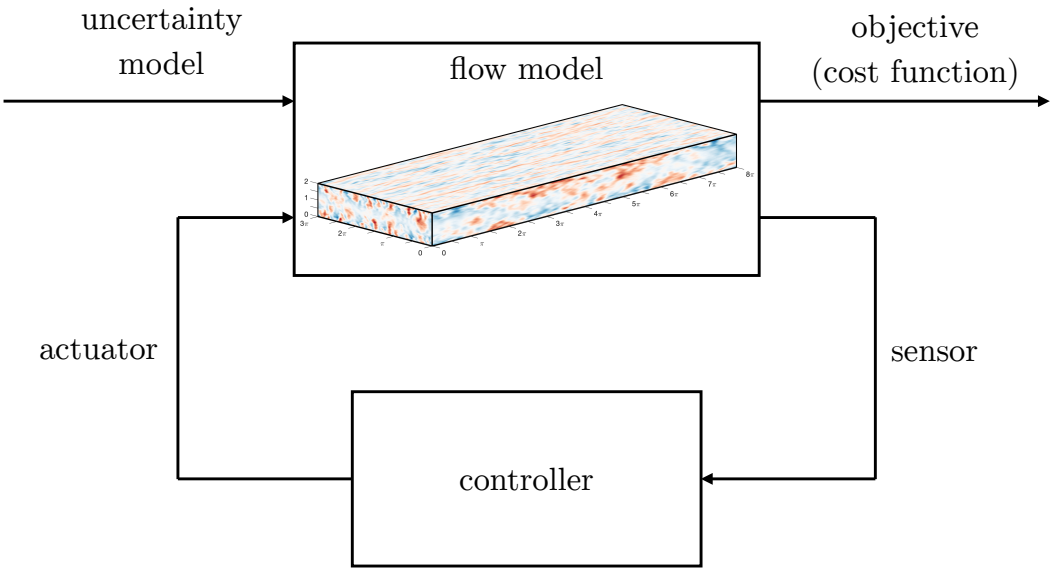

FIGURE 1.2: Feedback flow control.

Ginzburg-Landau equation); and (ii) a wall-bounded turbulent flow (Orr-Sommerfeld Squire equations). While free-shear flows mainly describe the flow behind objects, and wall-bounded flows revolve around boundary layers, the control objectives, tools and theory for both problems are similar.

The particular focus is on a well-established control method (introduced in chapter 2) to reduce velocity perturbations. We determine the best overall control performance that we can expect with a single sensor and single actuator set-up.

1.2.1 Ginzburg-Landau equation

In the first part of this thesis (chapter 3), we will introduce the $\mathcal{H}_2$-optimal control problem and apply it to the complex Ginzburg Landau equation, a model of spatially developing flows. The complex Ginzburg Landau equation has been the subject of many flow control studies (for example: Monkewitz, 1989; Park et al., 1993; Lauga and Bewley, 2003, 2004; Bagheri et al., 2009; Chen and Rowley, 2011). Its stability characteristics are similar to those of some shear flows, and it is therefore often used as a less demanding substitute.

These stability characteristics cause transient growth in stable flows and self-sustained oscillations in unstable flows; they are described by hydrodynamic stability

theory (Huerre and Monkewitz, 1990; Trefethen et al., 1993; Chomaz, 2005; Schmid, 2007; Schmid and Henningson, 2012). Mathematically, non-orthogonal eigenmodes characterise this behaviour that contributes to the challenges of flow control (Reddy et al., 1993).

1.2.2 Turbulent channel

In the second part of the thesis, we will look at linear estimation (chapter 4); sensor and actuator placement (chapter 5); and linear feedback control (chapter 6) of a wall-bounded turbulent channel flow. We design the estimators and controllers with a mathematical representation of the linear flow dynamics, which we derive from the Navier-Stokes equations and limited experimental data (del Alamo and Jiménez, 2006; Pujals et al., 2009; Hwang and Cossu, 2010*a*,*b*,*c*; McKeon and Sharma, 2010).

Linear models have been utilised in wall-bounded flows for both estimation studies (e.g. at laminar (Joshi et al., 1997; Hœpffner et al., 2005; Naguib et al., 2010), transitional (McKernan et al., 2007; Bagheri and Henningson, 2011; Jones et al., 2011) and turbulent (Chevalier et al., 2006; Illingworth et al., 2018; Oehler et al., 2018b) Reynolds numbers) and for control studies (e.g. at laminar (Bewley and Liu, 1998; Högberg and Bewley, 2000; Juillet et al., 2014; Chen and Rowley, 2014, 2015), transitional (Högberg et al., 2003*a*,*b*; Sharma et al., 2011; Semeraro et al., 2013; Belson, 2014) and turbulent (Cortelezzi et al., 1998*a*,*b*; Koumoutsakos, 1999; Kim, 2003; Stroh et al., 2015) Reynolds numbers). These estimation and control studies were successful because linear mechanisms play an important role in wall-bounded turbulent shear flows, especially for the maintenance of near-wall turbulence (Henningson and Reddy, 1994; Kim and Lim, 2000).

Near-wall turbulence, which significantly contributes to skin-friction drag, is sustained by a continuous cycle of generation and regeneration (Jiménez and Moin, 1991). Breaking the cycle at any point prevents the regeneration of new near-wall structures (Hamilton et al., 1995). Consequently, many turbulence flow control studies focus on structures in the near-wall region to directly reduce the drag at the wall (Moin and Bewley, 1994; Rathnasingham and Breuer, 1997, 2003; Karniadakis and Choi, 2003; Kasagi et al., 2009; Gouder et al., 2013; Bai et al., 2014). However, with increasing Reynolds number, these near-wall coherent structures become smaller (Cantwell, 1981; Head and Bandyopadhyay, 1981; Robinson, 1991; Gad-el Hak and

Bandyopadhyay, 1994; Park et al., 1994; Pope, 2000; Smits et al., 2011), and the control performance reduces (Chang et al., 2002; Iwamoto et al., 2002; Gatti and Quadrio, 2013; Hurst et al., 2014).

In contrast, there has been significantly less focus on the control of large-scale structures. These have shown to be important, particularly at high Reynolds numbers (Adrian et al., 2000; Guala et al., 2006; Balakumar and Adrian, 2007; Hutchins and Marusic, 2007*a*; Monty et al., 2007; Jiménez, 2012). Large-scale structures contribute significantly to the turbulent kinetic energy and Reynolds stresses in the outer region (Komminaho et al., 1996; Tomkins and Adrian, 2005; Guala et al., 2006), and there is evidence that these large-scale structures affect the near-wall cycle (Abe et al., 2004; Hutchins and Marusic, 2007*b*; Mathis et al., 2009).

1.3 Contributions and outline

The contributions of this thesis are as follows:
Ginzburg-Landau equation:

- The identification of trade-offs present when placing a single sensor and a single actuator in the complex Ginzburg-Landau system for a range of stabilities.
- Application of the iterative minimisation algorithm developed by Chen and Rowley (2011) to the estimation and full information control problems.
- Publication in the Journal of Fluid Mechanics: Oehler S. F. and Illingworth, S. J. (2018), 'Sensor and actuator placement trade-offs for a linear model of spatially developing flows', *J. Fluid Mech.* **854**, 34–55. .

Turbulent channel flow

- Linear estimation and control of fully developed turbulence at a relatively high Reynolds number ($\mathrm{Re}_\tau = 2000$).
- Application of the iterative minimisation algorithm to DNS data in the turbulent channel flow (estimation only).
- Comparison between at-wall placements and off-wall placements.

- Comparison between three set-ups where (i) we are limited to a single-plane sensor (but actuate everywhere), (ii) we are limited to a single-plane actuator (but measure everywhere), and (iii) where we are limited to a single-plane sensor and actuator.

- Identification of the scales for which control is most effective.

Chapter 2 describes $\mathcal{H}_2$-optimal control theory. We will introduce three problems that are used throughout this thesis.

In chapter 3, we consider feedback control of the linearised complex Ginzburg-Landau equation with a particular focus on the best placement of a single sensor and a single actuator. By varying the stability of the system, fundamental trade-offs between conflicting requirements for the placement are revealed.

In chapter 4, we introduce the estimation problem for the turbulent channel-flow. The estimator uses streamwise shear stress or velocity information at a single wall-normal location to estimate the streamwise velocity field at other locations. The measurement data either comes from DNS or is predicted by the linear model itself.

In chapter 5, we consider the best placement of a single-plane sensor and single-plane actuator for model-based estimation and control of a fully-developed turbulent channel flow. Specifically, we compare an approach where sensors and actuators are placed at the wall to an approach where sensors and actuators are placed inside the flow itself.

In chapter 6, three different control problems for the turbulent channel are compared: (i) we measure the flow at one wall-normal location but actuate it perfectly everywhere else; (ii) we know the entire flow field but actuate it at one wall-normal location; and (iii) we measure and actuate the flow at one wall-normal location.

Chapter 7 summarises and concludes the presented work.

Chapter 2

Methods

Fluid flows are categorised as distributed-parameter systems, which means they have an infinite number of dimensions. (For example, the analytical solution of the Ginzburg-Landau equation is described by an infinite number of Hermite polynomials (chapter 3).) Hence, there is an unlimited number of sensor and actuator locations. From this, the natural question arises: how many sensors and actuators do we need, and where should we place them? In an ideal case, we can measure and actuate the flow at all locations. In the worst case, we only have a single sensor and a single actuator available. If we want to compare the ideal case to the worst case, then four possible $\mathcal{H}_2$-optimal control problems arise (figure 2.1):

OE: Optimal Estimation: given knowledge of a single sensor measurement, we estimate the flow-field everywhere.

FIC: Full information control: given knowledge of the entire flow field, we control the flow with a single actuator.

IOC: Input-output control: given knowledge of a single sensor measurement, we control the flow with a single actuator.

FIAC: Full information and actuation control: given knowledge of the entire flow field, we control the flow with actuation everywhere.

Studying OE and FIC removes the challenges of having sensors and actuators at the same time. It helps to isolate the limitations of sensing and actuating and it

flow input / flow output	single actuator	no or perfect actuation of the flow
single sensor	*IOC*	*OE*
perfect sensing of the flow	*FIC*	*FIAC*

FIGURE 2.1: The four potential $\mathcal{H}_2$-optimal control problems.

helps to understand optimal placement. IOC is applicable in practical control, i.e. in an experiment, it is unlikely that we know the entire flow field. FIAC requires unbounded energy and as a consequence is an idealised set-up. We do not consider FIAC in this study, as it neither requires an estimator nor a controller and instantly sets the flow to the desired state.

We now summarise each problem and explain their design in more detail. This Chapter's purpose is to supplement the methods sections of Chapters 3-6 and will also provide some additional insight into the estimator and controller design process.

2.1 Optimal estimation

In the optimal estimation (OE) problem (also known as the filtering problem) quantities at one or multiple locations are measured to predict quantities at other locations. Problems can scale from small one-dimensional model flows with grid points of order ≈ 10 to very high-dimensional problems of order $\gtrapprox 10^6$. Mathematically small linear problems are often solved with a Kalman filter (Aström and Murray, 2010) and non-linear problems with the extended Kalman filter. Large problems (both linear and non-linear) utilise the more cost-efficient Ensemble-based Kalman filter (Evensen, 2009; Colburn, 2011; Fowler, 2012; da Silva and Colonius, 2018). In

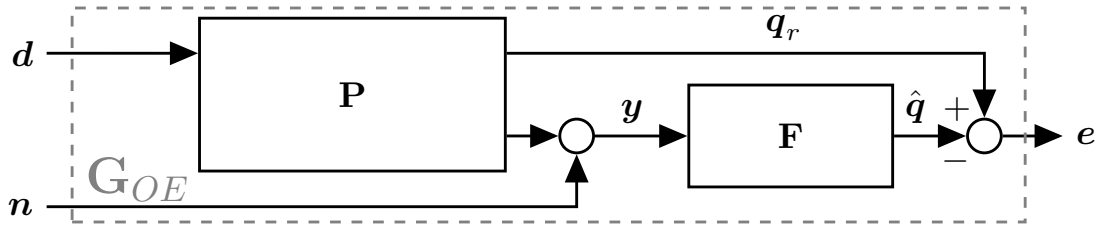

FIGURE 2.2: The block diagram for the optimal estimation problem. See figures 3.5, 4.1 and 5.1 for alternative versions.

this thesis, we employ the Kalman filter throughout as the systems we consider are relatively low-dimensional.

Optimal estimation (OE): we have a sensor at a single location (it could also be multiple sensors at various locations). The measurement $\boldsymbol{y}$, which is contaminated by noise $\boldsymbol{n}$, is used to estimate the reference flow-field $\boldsymbol{q}_r$. The estimate $\hat{\boldsymbol{q}}$ is generated using a Kalman filter. (*Thus we only have one sensor to measure the flow, and we want to use it to estimate the flow everywhere.*) We aim to minimise the estimation error signal $\boldsymbol{e} = \mathbf{C}_z(\boldsymbol{q}_r - \hat{\boldsymbol{q}})$ in the presence of disturbances (inputs) $\boldsymbol{d}$ and $\boldsymbol{n}$. A summary of the problem is shown in figure 2.2.

We can combine the flow model $\mathbf{P}$ with the Kalman filter $\mathbf{F}$ to form the linear fractional transform (LFT), which is the state-space model of the overall (input-output) system ($\mathbf{G}_{OE}$):

$$\begin{bmatrix} \dot{\boldsymbol{q}}_r \\ \dot{\hat{\boldsymbol{q}}} \end{bmatrix} = \begin{bmatrix} \mathbf{A} & \mathbf{0} \\ \mathbf{L}\mathbf{C}_y & \mathbf{A} - \mathbf{L}\mathbf{C}_y \end{bmatrix} \begin{bmatrix} \boldsymbol{q}_r \\ \hat{\boldsymbol{q}} \end{bmatrix} + \begin{bmatrix} \mathbf{B}_d & \mathbf{0} \\ \mathbf{0} & \mathbf{L}\mathbf{V}^{1/2} \end{bmatrix} \begin{bmatrix} \boldsymbol{d} \\ \boldsymbol{n} \end{bmatrix}, \tag{2.1}$$

$$\begin{bmatrix} \boldsymbol{e} \end{bmatrix} = \begin{bmatrix} \mathbf{C}_z & -\mathbf{C}_z \end{bmatrix} \begin{bmatrix} \boldsymbol{q}_r \\ \hat{\boldsymbol{q}} \end{bmatrix}, \tag{2.2}$$

where $\mathbf{A}$ is the dynamics matrix, $\mathbf{B}_d$ is the disturbance input matrix, $\mathbf{C}_y$ is the sensor matrix, $\mathbf{V}^{1/2}$ is the noise magnitude, $\mathbf{C}_z$ relates the states to the output and $\mathbf{L}$ is the Kalman filter gain matrix. The gain matrix $\mathbf{L}$ is designed by solving the following Ricatti equation (Zhou and Doyle, 1998):

$$\boldsymbol{A}\boldsymbol{Y} + \boldsymbol{Y}\boldsymbol{A}^* - \boldsymbol{Y}\boldsymbol{C}_y^*\boldsymbol{V}^{-1}\boldsymbol{C}_y\boldsymbol{Y} + \boldsymbol{B}_d\boldsymbol{B}_d^* = 0, \tag{2.3}$$

$$\mathbf{L} = \mathbf{Y}\mathbf{C}_y^*\mathbf{V}^{-1}, \tag{2.4}$$

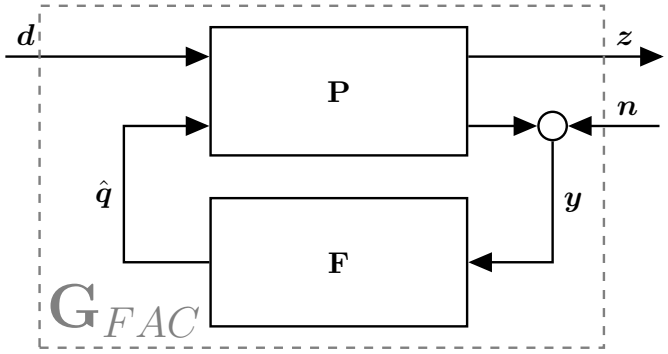

FIGURE 2.3: The block diagram for the full actuation control problem. See figure 6.2 for an alternative version.

where $()^*$ is the complex conjugate transpose.

2.1.1 Full actuation control

In Chapter 6, we introduce the full actuation control (FAC) problem: given knowledge of a single sensor measurement, we control the flow by applying body forces everywhere. In theory, the FAC problem is equivalent to the OE problem. The only difference is that we subtract the state estimate from the flow field to represent actuation of the flow everywhere:

$$\dot{\boldsymbol{q}} = \dot{\boldsymbol{q}}_r - \dot{\hat{\boldsymbol{q}}}. \tag{2.5}$$

Since actuation occurs instantly, FAC requires unbounded energy and as a consequence is an idealised set-up.

The block diagram for $\mathbf{G}_{FAC}$ is shown in figure 2.3 and the LFT for FAC is:

$$\begin{bmatrix}\dot{\boldsymbol{q}}\end{bmatrix} = \begin{bmatrix}\mathbf{A} - \mathbf{L}\mathbf{C}_y\end{bmatrix}\begin{bmatrix}\boldsymbol{q}\end{bmatrix} + \begin{bmatrix}\mathbf{B}_d & -\mathbf{L}\mathbf{V}^{1/2}\end{bmatrix}\begin{bmatrix}\boldsymbol{d}\\ \boldsymbol{n}\end{bmatrix}, \tag{2.6}$$

$$\begin{bmatrix}\boldsymbol{z}\end{bmatrix} = \begin{bmatrix}\mathbf{C}_z\end{bmatrix}\begin{bmatrix}\boldsymbol{q}\end{bmatrix}, \tag{2.7}$$

where $\boldsymbol{z}$ is the output that we want to minimise.

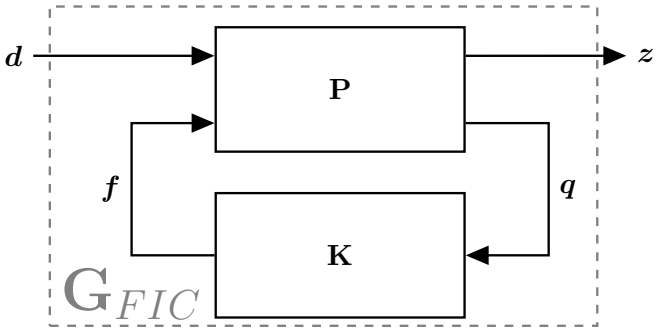

FIGURE 2.4: The block diagram for the full information control problem. See figures 3.5, 5.1 and 6.2 for alternative versions.

2.2 Full information control

In the full information control problem (FIC), we have perfect knowledge of the flow state everywhere; but we only have access to a single actuator to modify it. This problem follows naturally from the estimation problem: instead of estimating the state of the flow based on current and past measurements, we try to control the future state of the flow based on current and future forcing. We will observe similar results and challenges in the estimation and control problems.

Full information control (FIC): we have an actuator at a single location (it could also be multiple actuators at various locations), and we are given knowledge of the entire system state $\boldsymbol{q}$. A controller generates the actuator force $\boldsymbol{f}$. (*Thus we know everything about the flow, but we only have one actuator to control the flow.*) We aim to minimise the energy of the flow-field $\boldsymbol{q}$ while keeping $\boldsymbol{f}$ small ($\boldsymbol{z} \in [\boldsymbol{q}, \boldsymbol{f}]$) in the presence of disturbances (inputs) $\boldsymbol{d}$. The task of minimising the energy of the flow is chosen because it mathematically relates to the estimation problem. It is also directly related to the Reynolds stresses, and we hope that by reducing the Reynolds stresses we can reduce drag (in the turbulent channel flow). A summary of the problem is shown in figure 2.4.

We can combine the flow model $\mathbf{P}$ with the controller $\mathbf{K}$ to form the linear fractional transform (LFT), which is the state-space model of the overall (input-output) system ($\mathbf{G}_{FIC}$):

$$\begin{aligned}\left[\dot{\boldsymbol{q}}\right] &= \left[\mathbf{A} - \mathbf{B}_f\mathbf{K}\right]\left[\boldsymbol{q}\right] + \left[\mathbf{B}_d\right]\left[\boldsymbol{d}\right], \\ \left[\boldsymbol{z}\right] &= \begin{bmatrix}\mathbf{C}_z \\ -\mathbf{R}^{1/2}\mathbf{K}\end{bmatrix}\left[\boldsymbol{q}\right],\end{aligned}$$

where $\mathbf{B}_f$ represents the actuator, $\mathbf{R}^{1/2} = \alpha$ the actuation cost, and $\mathbf{K}$ is the controller gain matrix. The gain matrix is designed by solving the following Ricatti equation (Zhou and Doyle, 1998):

$$\mathbf{A}^*\mathbf{X} + \mathbf{X}\mathbf{A} - \mathbf{X}\mathbf{B}_y\mathbf{R}^{-1}\mathbf{B}_y^*\mathbf{X} + \mathbf{C}_z^*\mathbf{C}_z, \tag{2.8}$$

$$\mathbf{K} = \mathbf{R}^{-1}\mathbf{B}_f^*\mathbf{X}. \tag{2.9}$$

2.3 Input-output control

In the input-output control problem (IOC), we measure the flow at only one location and use this information to actuate the flow at only one location. The IOC problem consists of two subsystems: an estimator, which predicts the state of the flow $\hat{\boldsymbol{q}}$, and a controller which drives the actuator force $\boldsymbol{f}$. The principle of separation for estimation and control states that independently designed optimal estimators and controllers are still optimal when combined (Aström and Murray, 2010). Therefore, the estimator from OE ($\mathbf{F}$) and controller from FIC ($\mathbf{K}$) can be combined to form the IOC controller ($\mathbf{C}$).

Input-output control (IOC): we only have one sensor to estimate the flow, and we only have one actuator available to control the flow (it could also be multiple sensors and actuators at various locations). The measurement $\boldsymbol{y}$, which is contaminated by noise $\boldsymbol{n}$, is used to estimate the flow-field $\boldsymbol{q}$. The estimate $\hat{\boldsymbol{q}}$ is generated using the estimator. The actuator force $\boldsymbol{f}$ is generated by a controller which uses the estimate $\hat{\boldsymbol{q}}$. We aim to minimise the energy of the flow-field $\boldsymbol{u}$ while keeping $\boldsymbol{f}$ small ($\boldsymbol{z} \in [\boldsymbol{u}, \boldsymbol{f}]$) in the presence of disturbances (inputs) $\boldsymbol{d}$ and $\boldsymbol{n}$. A summary of the problem is shown in figure 2.5.

We can combine the flow model $\mathbf{P}$ (equation A.3) with the controller $\mathbf{C}$ to form the linear fractional transform (LFT), which is the state-space model of the overall

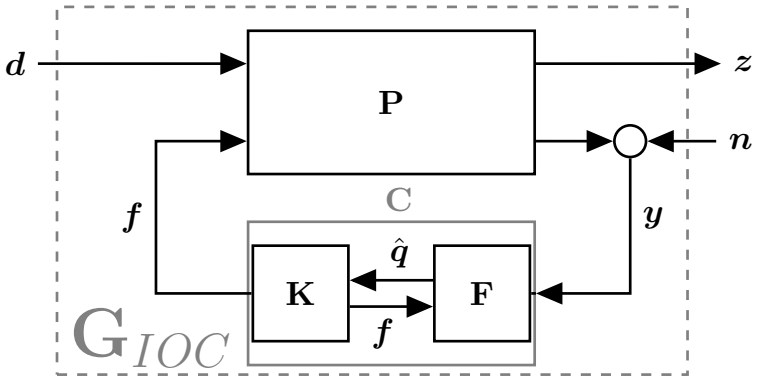

FIGURE 2.5: The block diagram for the input-output control problem. See figures 3.5, 5.1 and 6.2 for alternative versions.

(input-output) system ($\mathbf{G}_{IOC}$):

$$\begin{bmatrix} \dot{\boldsymbol{q}} \\ \dot{\hat{\boldsymbol{q}}} \end{bmatrix} = \begin{bmatrix} \mathbf{A} & -\mathbf{B}_f\mathbf{F} \\ \mathbf{L}\mathbf{C}_y & \mathbf{A} - \mathbf{B}_f\mathbf{F} - \mathbf{L}\mathbf{C}_y \end{bmatrix} \begin{bmatrix} \boldsymbol{q} \\ \hat{\boldsymbol{q}} \end{bmatrix} + \begin{bmatrix} \mathbf{B}_d & \mathbf{0} \\ \mathbf{0} & \mathbf{L}\mathbf{V}^{1/2} \end{bmatrix} \begin{bmatrix} \boldsymbol{d} \\ \boldsymbol{n} \end{bmatrix},$$
$$\begin{bmatrix} \boldsymbol{z} \end{bmatrix} = \begin{bmatrix} \mathbf{C}_z & 0 \\ 0 & -\mathbf{R}^{1/2}\mathbf{K} \end{bmatrix} \begin{bmatrix} \boldsymbol{q} \\ \hat{\boldsymbol{q}} \end{bmatrix}.$$

The estimator and controller gain matrices $\mathbf{L}$ and $\mathbf{K}$ can be obtained from equations 2.4 and 2.9.

Chapter 3

Sensor and actuator placement trade-offs for a linear model of spatially developing flows[1]

3.1 Abstract

We consider feedback flow control of the linearised complex Ginzburg–Landau system. The particular focus is on any trade-offs present when placing a single sensor and a single actuator. The work is presented in three parts. First, we consider the estimation problem in which a single sensor is used to estimate the entire flow field (without any control). Second, we consider the full information control problem in which the entire flow field is known, but only a single actuator is available for control. By considering the optimal sensor placement and optimal actuator placement while varying the stability of the system, a fundamental trade-off for both problems is made clear. Third, we consider the overall feedback control problem in which only a single sensor is available for measurement; and only a single actuator is available for control. By varying the stability of the system, similar fundamental trade-offs are made clear. We discuss implications for effective feedback control with a single sensor and a single actuator and compare it to previous placement methods.

[1]Based on Oehler S. F. and Illingworth, S. J. (2018), 'Sensor and actuator placement trade-offs for a linear model of spatially developing flows', *J. Fluid Mech.* **854**, 34–55.

3.2 Literature review

Flow control is either passive (for example through the modification of a surface profile), or active via actuators. Examples of flow control include the delay of vortex shedding, the reduction of drag and the enhancement of lift (see Gad-el-Hak, 1996; Gad-el-Hak et al., 2003; Brunton and Noack, 2015, for extensive reviews). In the more specific case of feedback flow control, the actuators rely on sensor readings to adjust their behaviour. Early experimental studies employed *ad hoc* feedback control schemes. For example, Wehrmann (1965) and Berger (1967) placed a piezo-electric transducer device into an air flow, which served as a cylinder and actuator simultaneously. The transducer was excited by an amplified signal from a hot-wire probe to suppress vortex shedding and delay transition. Similar approaches have been used for feedback flow control, such as cancelling Tollmien-Schlichting waves in a boundary layer with flush-mounted heating elements (Liepmann and Nosenchuck, 1982) or delaying the onset of the wake instability in the flow past a cylinder using a loudspeaker (Williams and Zhao, 1989; Roussopoulos, 1993).

Subsequent studies have considered some mathematical description of the flow dynamics to implement controllers (see for example Kim and Bewley, 2007; Choi et al., 2008; Bagheri et al., 2009; Noack et al., 2011; Brunton and Noack, 2015; Taira et al., 2017). These mathematical descriptions can be operator based, i.e. derived from the underlying physics, or data based, i.e. derived from numerical or experimental data (Taira et al., 2017); and sometimes they use a combination of both operators and data (Reynolds and Hussain, 1972).

One can employ a mathematical description to design a suitable feedback controller, test a designed feedback controller before implementing it or both. There are various controller designs available: (i) we can select dynamics for the flow, or we can cancel specific dynamics of the flow, examples of which include pole placement (Litrico and Georges, 1999) and dynamic phasors (Rowley and Juttijudata, 2005; Illingworth et al., 2012); (ii) we can manually tune a controller, examples of which include proportional (Monkewitz, 1989; Park et al., 1993; Son et al., 2011), proportional–integral (Joshi et al., 1997; Son et al., 2011), proportional–derivative (Son et al., 2011), and proportional–integral–derivative control (Cohen et al., 2003, 2005), as well as fuzzy logic control (Cohen et al., 2003, 2005), and loop shaping

(Illingworth, 2014, 2016); and (iii) we can implement a control scheme which optimises control objectives, while being able to model specific disturbances, examples include $\mathcal{H}_2$-optimal and $\mathcal{H}_\infty$-robust control (Bewley and Liu, 1998; Lauga and Bewley, 2003, 2004), neural network control (Gillies, 1998) and model predictive control (Bewley et al., 2001).

We can improve the performance of feedback flow control by finding the optimal locations for the sensors and actuators employed. Optimal placement is a challenging problem for flow control (and indeed for any control problem) because of the following predicament: we can neither design a controller without placement nor determine the placement performance before designing a controller. Therefore, most placements are based on experience or a flow's physical characteristics. Åkervik et al. (2007) placed sensors according to the least stable eigenmode, which provides the best detectability for that mode; and placed actuators according to the least stable adjoint mode, which provides the best stabilisability for that mode. Mons et al. (2017) placed sensors through an adjoint-based sensitivity analysis, which identifies regions most susceptible to changes in initial conditions, boundary conditions or flow parameters. The more specific structural sensitivity was used by Natarajan et al. (2016) to place collocated actuator–sensor pairs. Structural sensitivity identifies locations which are "characterized by *both* a high sensitivity of and a strong response in the most unstable mode" (Schmid and Brandt, 2014). The region of high structural sensitivity is also known as the wavemaker region, which describes the overlap between eigenmodes and adjoint eigenmodes (Chomaz, 2005; Giannetti and Luchini, 2007). Other placement approaches consider the regions where instabilities are present (e.g. Gillies, 2001; Bagheri et al., 2009).

While each of these placement approaches is sensible, none of them can alone provide the whole picture concerning the placement problem. To find the optimal placement, one has to first quantify the control performance and then search for the optimal locations (e.g. Chen and Rowley, 2011; Juillet et al., 2013; Hu et al., 2016). Efficiently searching for the optimal locations originated in the applied mathematics community (see Bensoussan, 1972; Yu and Seinfeld, 1973; Chen and Seinfeld, 1975; Kumar and Seinfeld, 1978) where it has been applied to a more general class of distributed-parameter systems (e.g. Burns and King, 1994; Reinschke, 1999; Reinschke and Smith, 2003; Morris, 2011; Kasinathan and Morris, 2013). Recent feedback

flow control studies have considered optimal placement for a boundary layer (Belson et al., 2013) and the flow past a cylinder (Akhtar et al., 2015). Related estimation studies investigated optimal placement for the dispersive wave equation (Khan et al., 2015), and the Boussinesq equation (Hu et al., 2016).

The current work considers the sensor and actuator placement problems for convection-dominated spatially developing flows, such as wall-bounded and free shear flows. These types of flows are subject to spatially varying instabilities, which cause perturbations to be amplified as they are convected downstream (Chomaz et al., 1987, 1988, 1990, 1991). Spatially varying instabilities lead to transient growth in stable flows, and to self-sustained oscillations in unstable flows, both of which can be described using hydrodynamic stability theory (Huerre and Monkewitz, 1990; Trefethen et al., 1993; Cossu and Chomaz, 1997; Chomaz, 2005). Convection-dominated flows are mathematically characterised by non-orthogonal eigenmodes, which affects the sensor and actuator placement.

One such convection-dominated system suitable for studying the placement problem is the complex Ginzburg-Landau equation (introduced in §3.3). It has been the subject of various feedback control studies (e.g. Monkewitz, 1989; Park et al., 1993; Lauga and Bewley, 2003, 2004; Cohen et al., 2005; Bagheri et al., 2009; Chen and Rowley, 2011; Colburn, 2011; Illingworth, 2015). Since the complex Ginzburg-Landau equation has similar stability characteristics as the Navier-Stokes equations, it can be seen as a computationally less demanding substitute. Chen and Rowley (2011, 2014, 2015) used the complex Ginzburg-Landau equation to study the optimal placement problem using an $\mathcal{H}_2$ controller. They modified an iterative-gradient minimisation algorithm developed by Hiramoto et al. (2000) to solve for the optimal placement at two stabilities: (i) a system with one unstable mode; and (ii) a transiently unstable system. The optimal placement of up to five sensors and five actuators was considered. For a single sensor and single actuator set-up, neither placement based on the eigenmode and adjoint eigenmode, nor on the wavemaker region, resulted in the optimal solution. It was concluded that placement based on the eigenmodes and adjoint eigenmodes fails because the underlying dynamics is non-normal, and that excessive time lag had a detrimental effect on perturbation control.

Simulation parameters

U	c_u	c_d	μ_0	μ_2	U_{max}	N	L	v	α
2	0.2	-1	-0.01 to 0.9	-0.01	1.6	150	25	10^{-3}	$1/7$

TABLE 3.1: Considered parameters for the complex Ginzburg–Landau equation.

The contribution of the current work is to study any trade-offs present when placing a single sensor and a single actuator in the complex Ginzburg-Landau system for a range of stabilities. (The selected stabilities range from stable systems to systems with up to four unstable modes.) We will see that the trade-offs we study become increasingly important as we decrease the stability of the system. This work is significant and timely for flow control: by using a simple system and reducing the number of variables (we only use a single sensor, a single actuator or both), we can show and discuss fundamental trade-offs which make the placement problem a challenging one.

The current work considers three problems, which are defined in §3.4 and studied §3.5. First, we will look at the placement of a single sensor in the optimal estimation (OE) problem. Second, we will look at the placement of a single actuator in the full information control (FIC) problem. This keeps the number of variables small to provide insight into the individual sensor and actuator performances. Third, we will study the combined single sensor and single actuator placement of the input–output control (IOC) problem, which is more applicable to experimental applications. In §3.6 we will further analyse the results and discuss the trade-offs which determine the optimal location for a single sensor and single actuator.

3.3 The complex Ginzburg-Landau equation

This section introduces the linearised complex Ginzburg-Landau equation (CGLE). A comprehensive review of the CGLE is given by Bagheri et al. (2009). Table 3.1 summarises the simulation parameters considered in this study (to be introduced), which follow the work of Bagheri et al. (2009), Chen and Rowley (2011) and Oehler et al. (2016).

3.3.1 The continuous equation

The linearised CGLE subject to unknown disturbances $d(x,t)$ is:

$$\frac{\partial q(x,t)}{\partial t} = \left(-\nu\frac{\partial}{\partial x} + \kappa\frac{\partial^2}{\partial x^2} + \mu(x)\right) q(x,t) + d(x,t), \tag{3.1a}$$

$$= Aq(x,t) + d(x,t), \tag{3.1b}$$

where A is the Ginzburg-Landau operator which governs the evolution of the flow's perturbations $q(x,t)$. The operator is defined on an infinite interval: $-\infty < x < \infty$, with initial conditions $q(x,0) = q_0(x)$ and boundary conditions $q(x,t) < \infty$, as $x \to \pm\infty$. The complex terms $\nu = U + 2\mathrm{j}c_u$ and $\kappa = 1 + \mathrm{j}c_d$ represent the convective and the dissipative nature of the flow, where U is the mean advection velocity, c_u the most unstable wavenumber and c_d the dispersion parameter. The overall group velocity of the perturbations is $U_{max} = U + 2c_u c_d$. A parabolic function $\mu(x) = \mu_0 - c_u^2 + \mu_2 x^2/2$ introduces the flow's non-parallel nature and instabilities, where $\mu_2 < 0$. The flow's instabilities cause the natural occurrence of amplification when $\omega_{i,max}(x) > 0$, and decay when $\omega_{i,max}(x) < 0$, where $\omega_{i,max}(x) = \mu_0 + \mu_2 x^2/2$ is the growth rate of the most unstable wavenumber (Chomaz et al., 1987, 1988; Bagheri et al., 2009). The natural amplification creates an unstable region which spans the region: $-\sqrt{-2\mu_0/\mu_2} < x < \sqrt{-2\mu_0/\mu_2}$; we refer to the unstable region's upstream and downstream limits as X_I and X_{II}.

An analytical solution exists for the complex Ginzburg-Landau equation, from which the eigenvalues (λ_n), eigenmodes (ϕ_n), adjoint eigenmodes (ψ_n) and the wavemaker region (ζ_n) can be generated:

$$\lambda_n = \mu_0 - c_u^2 - \nu^2/(4\kappa) - (n+0.5)h, \tag{3.2a}$$

$$\phi_n(x) = \exp\left(0.5\left(\nu x/\kappa - (\chi x)^2\right)\right) H_n(\chi x), \tag{3.2b}$$

$$\psi_n(x) = \exp\left(-\bar{\nu}x/\bar{\kappa}\right) \bar{\phi}_n(x), \tag{3.2c}$$

$$\zeta_n(x) = \frac{\phi_n(x)\bar{\psi}_n(x)}{\langle \phi_n, \psi_n \rangle}, \tag{3.2d}$$

where $h = \sqrt{-2\mu_2\kappa}$, $\chi = (-\mu_2/(2\kappa))^{0.25}$, $n = \{0, 1, ...\}$, H_n is the nth Hermite polynomial and $\bar{(\cdot)}$ is the complex conjugate. The eigenmodes and adjoint eigenmodes are symmetric with respect to each other. The wavemaker region represents the

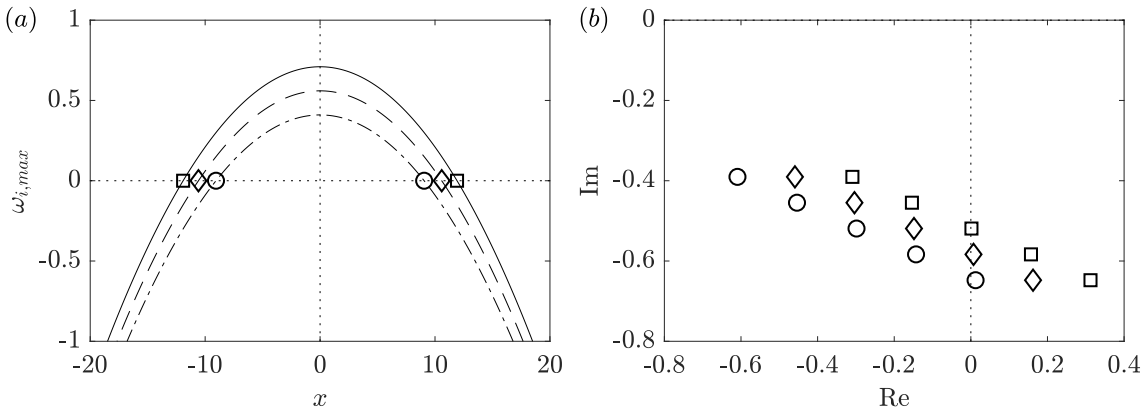

FIGURE 3.1: (a) The growth rate of the most unstable wavenumber $\omega_{i,max}(x)$ for $\mu_0 = (0.41(-\cdot), 0.56(--), 0.71(—))$, at which: $X_{II} = (9.1(\bigcirc), 10.6(\diamond), 11.9(\square))$ and $X_I = -X_{II}$. (b) The five most unstable eigenvalues λ_n for $\mu_0 = (0.41(\bigcirc), 0.56(\diamond), 0.71(\square))$.

degree of overlap between the eigenmodes and adjoint eigenmodes (Giannetti and Luchini, 2007).

In §4 we will consider sensor and actuator placement over a range of μ_0, but investigate in more detail only the cases: $\mu_0 = 0.41$, $\mu_0 = 0.56$ and $\mu_0 = 0.71$, all of which are globally unstable. These three cases correspond to there being one, two and three unstable modes, respectively. We will now look at some characteristics of the CGLE for the three cases. This will become important later when we look at sensor and actuator placement. Figure 3.1(a) shows the growth rate of the most unstable wavenumber $\omega_{i,max}(x)$, together with the upstream X_I and downstream X_{II} limits of the unstable region for the three cases; figure 3.1(b) shows the first five eigenvalues λ_n for the three cases. We see that increasing μ_0 causes $\omega_{i,max}(x)$, X_I, X_{II}, and the real part of λ_n all to increase in magnitude. However, increasing μ_0 does not change the shape of the eigenmodes ϕ_n and the shape of the adjoint eigenmodes ψ_n themselves. We have included the three most unstable eigenmodes (ϕ_0, ϕ_1, ϕ_2) and adjoint eigenmodes (ψ_0, ψ_1, ψ_2) in figure 3.2. The first three eigenmodes' global maxima occur at $x = 7.3$, $x = 9.3$ and $x = 10.9$. For the second eigenmode ϕ_1 a global minimum exists at $x = 0$, and for the third eigenmode, ϕ_2, two local minima exist at $x \approx -3.0$ and $x \approx 2.7$. Symmetric maxima and minima are obtained for the adjoint eigenmodes.

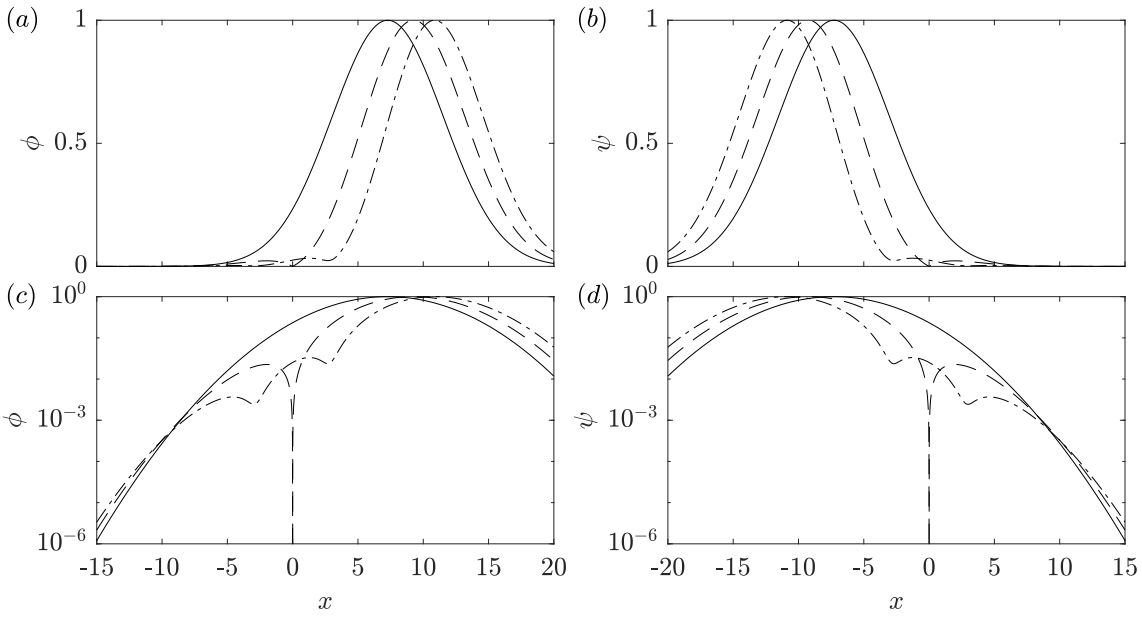

FIGURE 3.2: (a,c) The three most unstable eigenmodes (normalised): $\phi_0(—)$, $\phi_1(--)$, and $\phi_2(-\cdot)$. (b,d) The three most unstable adjoint eigenmodes (normalised): $\psi_0(—)$, $\psi_1(--)$, and $\psi_2(-\cdot)$. Figures are on a linear (a,b) and logarithmic (c,d) scale.

3.3.2 The discretised time-invariant model

Until now, we have treated the Ginzburg-Landau equation as a continuous system, but to control the flow we need to discretise it and then express it in state-space form. This section describes how to do so.

The first step is to discretise the operator A in the spatial domain. Instead of employing the naturally occurring Hermite interpolates for this task, we choose the Chebyshev collocation method (Trefethen, 2000) because it converges at a lower order (see Appendix A.1). We choose an order of $N+1 = 151$ with suitable boundary conditions and scaling L, such that the domain is defined between $-25 < x < 25$. A convergence and scaling study showed convergence for all set-ups considered in this paper. The second step is to discretise the unknown disturbances $d(x,t)$. (More details are given in Appendix A.1.)

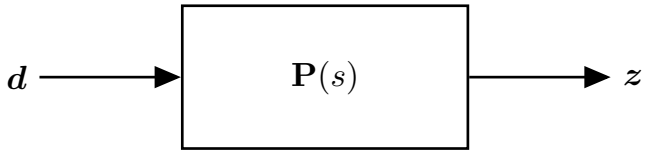

FIGURE 3.3: Single transfer function $\mathbf{P}(s)$ of the state-space model.

Having discretised the continuous CGLE, we can express it as a linear time-invariant state-space model (3.3):

$$\dot{\boldsymbol{q}}(t) = \mathbf{A}\boldsymbol{q}(t) + \mathbf{B}_d\boldsymbol{d}(t), \tag{3.3a}$$
$$\boldsymbol{z}(t) = \mathbf{C}_z\boldsymbol{q}(t), \tag{3.3b}$$

where $\boldsymbol{q}$ is the system state and $\boldsymbol{z} = \mathbf{C}_z\boldsymbol{q}$ an output of interest. (For example, we might be interested in $\boldsymbol{q}$ at every location in the domain, in which case $\mathbf{C}_z = \mathbf{I}$, or only in some smaller region, in which case $\mathbf{C}_z$ will be zero outside the region of interest.) We can combine (3.3) into a single transfer function $\mathbf{P}(s)$ by taking the Laplace transform (figure 3.3).

3.4 Estimator and controller design

The CGLE is subject to disturbances $\boldsymbol{d}$, which introduce perturbations into the flow. We will first look at how to detect these perturbations using a single sensor placed at x_s; and second, how to then reduce their effect using a single actuator placed at x_a. We, therefore, update the state-space model (3.3) to include an actuator and a sensor (3.4):

$$\dot{\boldsymbol{q}}(t) = \mathbf{A}\boldsymbol{q}(t) + \mathbf{B}_d\boldsymbol{d}(t) + \mathbf{B}_u\boldsymbol{u}(t), \tag{3.4a}$$
$$\boldsymbol{z}(t) = \mathbf{C}_z\boldsymbol{q}(t) + \mathbf{D}_u\boldsymbol{u}(t), \tag{3.4b}$$
$$\boldsymbol{y}(t) = \mathbf{C}_y\boldsymbol{q}(t) + \boldsymbol{n}(t). \tag{3.4c}$$

The sensor measurement $\boldsymbol{y}$ is given by $\mathbf{C}_y\boldsymbol{q}$, which is contaminated by noise $\boldsymbol{n}$. (We treat $\boldsymbol{n}$ as an unknown forcing which is white in space and time with covariance $v = \mathbb{E}(\boldsymbol{n}\boldsymbol{n}^*) = 10^{-3}$, where $\mathbb{E}$ is the expected value) Note that, in general, the quantity we measure ($\boldsymbol{y}$) is not the same as the quantity we want to keep small ($\boldsymbol{z}$).

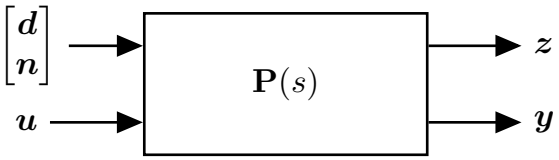

FIGURE 3.4: Single transfer function $\mathbf{P}(s)$ of the updated state-space model.

Actuation is represented by $\mathbf{B}_u\boldsymbol{u}$, which introduces perturbations into the system. The input $\boldsymbol{u}$ is also a signal of interest, i.e. something we want to monitor, and therefore, $\boldsymbol{z}$ includes $\boldsymbol{u}$, which is scaled by $\mathbf{D}_u$. As in (3.3), we can combine the updated state-space model (figure 3.4) into a single transfer function $\mathbf{P}(s)$.

3.4.1 The estimation and control problems

We now want to use the extended plant model (3.4) to investigate three different problems: (i) estimating the entire flow with one sensor (without any control), (ii) controlling the flow with one actuator (when the entire system state is known) and (iii) controlling the flow with one actuator when only provided with a single sensor reading. Figure 3.5 shows a summary of the three problems. Each problem has a secondary system $\mathbf{R}(s)$ which needs to be designed (OE: estimator, FIC: controller and IOC: controller.)

3.4.1.1 The optimal estimation (OE) problem

Given a single sensor measurement $\boldsymbol{y}$, which is contaminated by noise $\boldsymbol{n}$, our task in the optimal estimation (OE) problem is to estimate the entire state $\boldsymbol{q}$, which is subject to disturbances $\boldsymbol{d}$. The estimate $\hat{\boldsymbol{q}}$ is generated using an estimator. (*Thus we only have one sensor to measure the flow; and we want to use it to estimate the flow everywhere.*) Our aim is to minimise the energy of the estimation error signal $\boldsymbol{z} = \boldsymbol{e} = \mathbf{C}_z(\boldsymbol{q} - \hat{\boldsymbol{q}})$ in the presence of inputs $\boldsymbol{d}$ and $\boldsymbol{n}$. The following cost function can be derived from the error signal $\boldsymbol{e}$:

$$J_{OE} = \mathbb{E}\left\{\lim_{t\to\infty}\frac{1}{T}\int_0^T\left(\int_{-\infty}^{\infty}(q(x,t)-\hat{q}(x,t))^*(q(x,t)-\hat{q}(x,t))dx\right)dt\right\}. \tag{3.5}$$

System	quantity measured	quantity actuated	quantity minimised
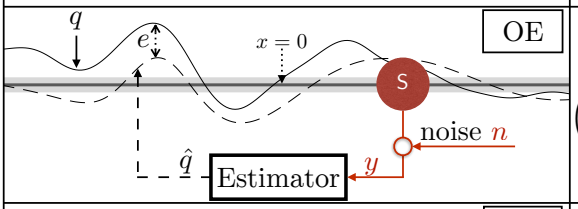	$\boldsymbol{q}$ at x_s (contaminated by noise $\boldsymbol{n}$)	no actuation	error $\boldsymbol{q} - \hat{\boldsymbol{q}}$
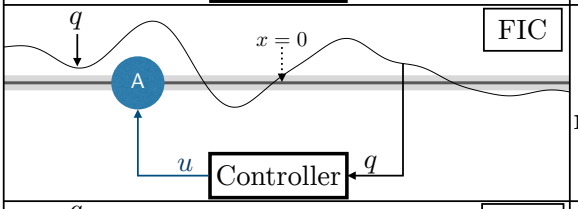	no measurement	body force $\boldsymbol{u}$ at x_a	cost $\boldsymbol{q} + \alpha\boldsymbol{u}$
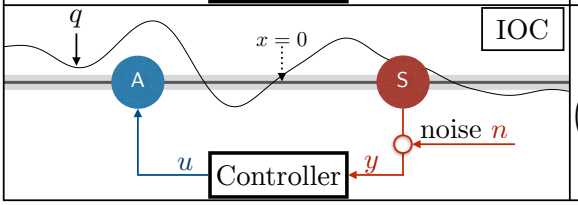	$\boldsymbol{q}$ at x_s (contaminated by noise $\boldsymbol{n}$)	body force $\boldsymbol{u}$ at x_a	cost $\boldsymbol{q} + \alpha\boldsymbol{u}$

FIGURE 3.5: Summary of the OE, FIC, and IOC problems.

3.4.1.2 The full information control (FIC) problem

Given knowledge of the entire state $\boldsymbol{q}$, our task in the full information control (FIC) problem is to control the entire $\boldsymbol{q}$ field, which is subject to disturbances $\boldsymbol{d}$, using a single actuator. The actuator force $\boldsymbol{u}$ is generated by a controller. (*Thus we know everything about the flow; but we only have one actuator to control the flow.*) Our aim is to minimise the energy of the cost signal $\boldsymbol{z}$ in the presence of input $\boldsymbol{d}$. The following cost function can be derived from the cost signal $\boldsymbol{z}$:

$$J = \mathbb{E}\left\{\lim_{t\to\infty}\frac{1}{T}\int_0^T\left(\int_{-\infty}^{\infty} q(x,t)^* q(x,t)dx + \alpha^2 u(t)^* u(t)\right)dt\right\}, \tag{3.6}$$

where α is a penalisation of the actuator force.

3.4.1.3 The input–output control (IOC) problem

Given a single sensor measurement $\boldsymbol{y}$, which is contaminated by noise $\boldsymbol{n}$, our task in the input–output control (IOC) problem is to control the entire $\boldsymbol{q}$ field, which is subject to disturbances $\boldsymbol{d}$, using a single actuator. The actuator force $\boldsymbol{u}$ is generated

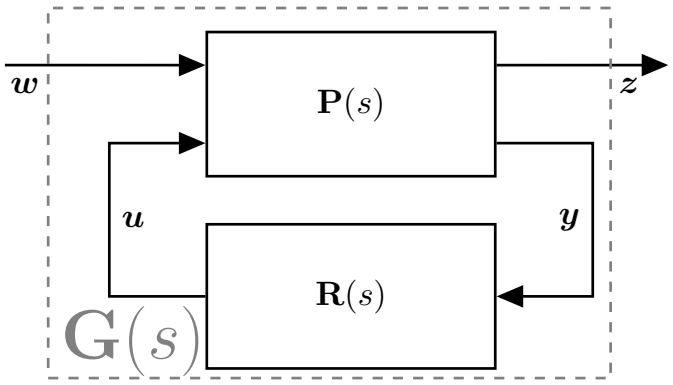

FIGURE 3.6: Block diagram of the full model containing the dynamics of the flow $\mathbf{P}(\mathbf{s})$ and secondary system $\mathbf{R}(s)$.

by a controller. Full-state information is required for the controller, but since $\boldsymbol{q}$ is not available, we estimate it using an estimator. (*Thus we only have one sensor to estimate the flow; and we only have one actuator available to control the flow.*) Our aim is to minimise the energy of the cost signal $\boldsymbol{z}$ in the presence of inputs $\boldsymbol{d}$ and $\boldsymbol{n}$. The cost function defined in equation 3.6 can be derived from the cost signal $\boldsymbol{z}$.

3.4.2 Optimising the performance

We couple the secondary system $\mathbf{R}(s)$ with the plant model $\mathbf{P}(s)$ into an overall transfer function $\mathbf{G}(s)$, defined such that $\boldsymbol{z} = \mathbf{G}(s)\boldsymbol{w}$. All three stated problems have two things in common: an unknown input $\boldsymbol{w}$ ($\boldsymbol{d}$ and $\boldsymbol{n}$; or $\boldsymbol{d}$); and an output $\boldsymbol{z}$ that we want to keep small. The general design problem can now be stated as follows: given $\mathbf{P}(s)$, design $\mathbf{R}(s)$ such that $\mathbf{G}(s)$ is small. Thus, we first need to quantify the size of $\mathbf{G}(s)$.

A common way to quantify the size of $\mathbf{G}(s)$ is to use the $\mathcal{H}_2$-norm, which is defined as:

$$\gamma \triangleq \|\mathbf{G}(s)\|_2 = \sqrt{\frac{1}{2\pi}\int_{-\infty}^{\infty} \text{Trace}[\mathbf{G}^*(\mathrm{j}\omega)\mathbf{G}(\mathrm{j}\omega)]d\omega} = \sqrt{\frac{1}{2\pi}\int_{-\infty}^{\infty} \sum_i (\sigma_i(\mathbf{G}(\mathrm{j}\omega)))^2 d\omega}, \tag{3.7}$$

where σ_i are the singular values of $\mathbf{G}(s)$ at frequency ω. Since the singular values can be considered a generalisation of a transfer function's gain when there are multiple

inputs and multiple outputs, we can consider the $\mathcal{H}_2$-norm as an average gain over all frequencies and all directions. We refer to the $\mathcal{H}_2$-norm generated by the OE problem as γ_{OE}, the FIC problem as γ_{FI} and IOC problem as γ_{IO}.

The problem of how to then design $\mathbf{R}(s)$ to make $\mathbf{G}(s)$ small is a well-understood problem, and hence can be solved using standard tools. However, the locations of the sensor and actuator form part of the system $\mathbf{P}(s)$, and therefore, we can only obtain the best possible $\mathbf{R}(s)$ for a given sensor location x_s, a given actuator location x_a or both. To obtain the optimal sensor and actuator locations we have to either solve γ for a set of x_s and x_a, known as brute force solving, or use an iterative-gradient minimisation algorithm. We employ an iterative-gradient minimisation algorithm which was developed by Chen and Rowley (2011), where it was successfully applied to the IOC problem for two values of μ_0.

It is important to consider the effect of v and α for three reasons: (i) the optimal placement problem, (ii) the estimation performance, and (iii) the control performance. Previous studies have looked at the effect of v and α for the IOC problem (Lauga and Bewley, 2004; Chen and Rowley, 2011). Based on these studies, we have chosen $\alpha = 1/7$ and $v = 10^{-3}$. The actuation cost α is a compromise between a reasonably sized actuator signal and an effective reduction in the perturbation magnitude. The noise covariance v is a compromise between a negligibly sized sensor noise and the well-posedness of the system. The optimal sensor and actuator locations are insensitive to the choice of α and v for all systems and μ_0 considered in this study.

For more information on the estimator design, the controller design and the optimal placement see Appendices A.2 and A.3. Further details on the control tools used in this section (and the appendices) can be found in Kim and Bewley (2007); Skogestad and Postlethwaite (2007); Bagheri et al. (2009); Aström and Murray (2010); Chen and Rowley (2011).

3.5 Results

We will now look at optimal placement, and the effect that varying the stability of the system has on optimal placement. This section consists of three parts: first, we consider the optimal estimation (OE) problem, then the full information control

(FIC) problem and finally the input–output control (IOC) problem. We study the OE and FIC problems together for better comparison.

3.5.1 The OE and FIC problems

We start by looking at the OE problem for a single value of $\mu_0 = 0.41$ when random disturbances are applied everywhere in the domain. The estimation error norm γ_{OE} is generated as a function of sensor location x_s in figure 3.7(a), which reveals the optimal sensor location to be at $x_{s-opt} \approx 2.10$, for which $\gamma_{OE} \approx 5.70$. Placing the sensor downstream of x_{s-opt} is penalised less than placing it upstream of x_{s-opt}.

We now repeat the same analysis for the FIC problem. The energy norm γ_{FI} is generated as a function of actuator location x_a in figure 3.7(b), which reveals the optimal actuator location to be at $x_{a-opt} \approx -2.01$, where $\gamma_{FI} \approx 5.85$. Analogous to the OE problem, placing the actuator upstream of x_{a-opt} is penalised less than placing it downstream of x_{a-opt}.

Having found the optimal sensor and actuator locations for a single value of μ_0, it is now interesting to look at how placement varies with μ_0. Results for two higher values of μ_0 are also shown figure 3.7(a,b): $\mu_0 = 0.56$, for which there are two unstable modes, and $\mu_0 = 0.71$, for which there are three unstable modes. When $\mu_0 = 0.56$, the optimal sensor location shifts downstream and γ_{OE} increases; a local maximum occurs at $x_s = 0$ and γ_{OE} changes rapidly within the vicinity of the maximum. When $\mu_0 = 0.71$, the optimal sensor location shifts even further downstream, and the local maximum at the centre increases in magnitude. Rapid changes of γ_{OE} now also occur at $x_s \approx -3$ and $x_s \approx 2.7$ (figure 3.7(a)). In all three cases, it is better to place the sensor too far downstream than too far upstream. Similar results are obtained for the FIC problem (figure 3.7(b)).

So far, we considered three distinct values of μ_0. We now look in more detail at how x_{s-opt} and x_{a-opt} vary with μ_0; this is computationally expensive, and so we employ the gradient minimisation algorithm of Chen and Rowley (2011). Figure 3.7(c) shows that, as μ_0 is varied over the range $-0.01 \leq \mu_0 \leq 0.9$, x_{s-opt} shifts downstream from 0.92 to 5.36, while x_{a-opt} shifts upstream from -0.80 to -5.34. In addition to plotting x_{s-opt} and x_{a-opt} with μ_0, it is also interesting to look at the optimal positions' energy norms, which provide information on the difficulty of estimation and control. In figure 3.7(d,e) the optimal OE energy norm $\gamma_{OE}(x_{s-opt})$

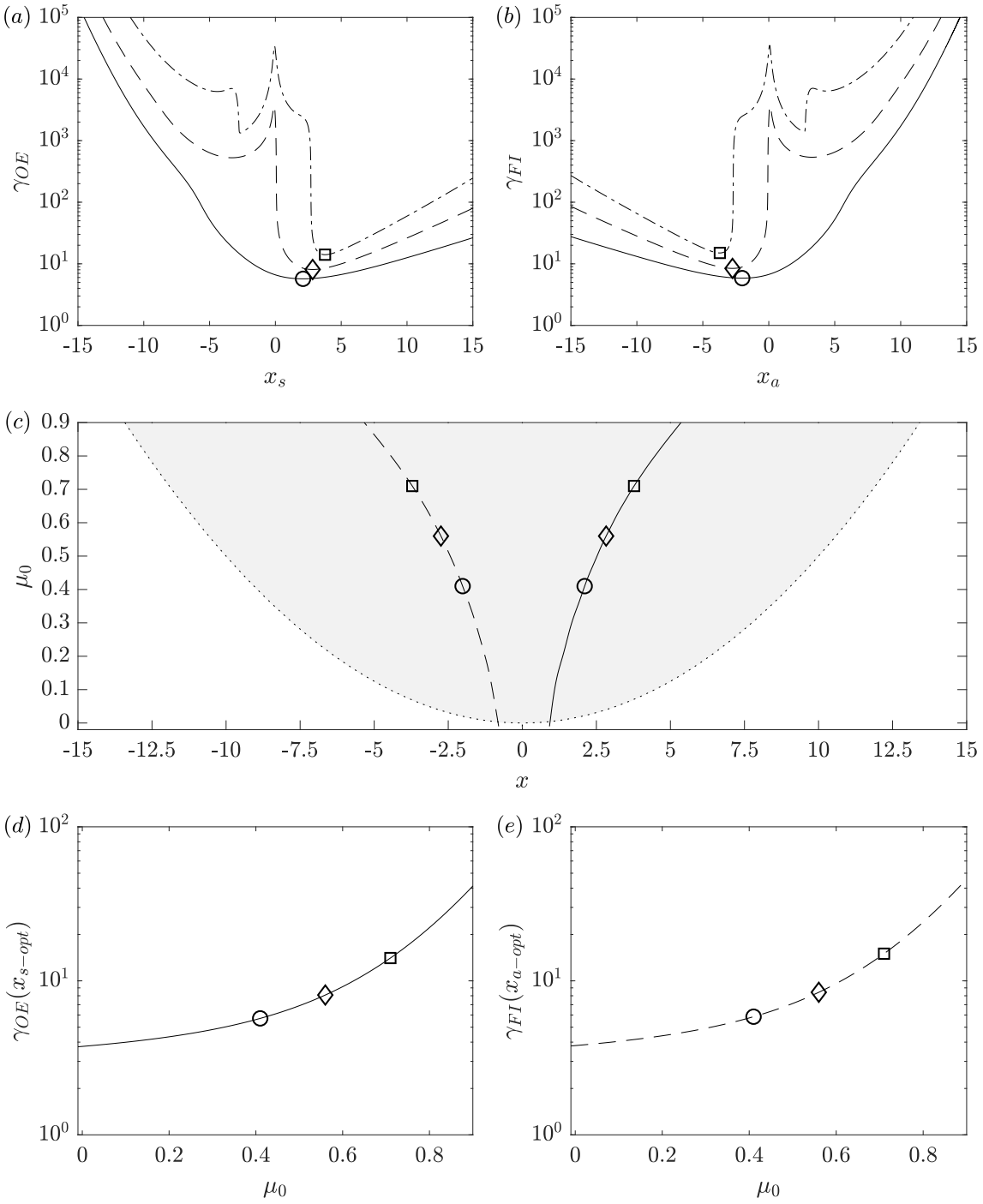

FIGURE 3.7: (a) The OE norm γ_{OE} as a function of sensor location x_s and (b) the FIC norm γ_{FI} as a function of actuator location x_a for stability parameters $\mu_0 = (0.41(—), 0.56(--), 0.71; (-\cdot))$. (c) The OE optimal sensor location $x_{s-opt}(—)$ and the FIC optimal actuator location $x_{a-opt}(--)$, and the unstable region's limits (:) as a function of μ_0. The unstable region is shaded grey; it only exists when $\mu_0 > 0$. (d) The OE norm $\gamma_{OE}(x_{s-opt})$ and (e) the FIC norm $\gamma_{FI}(x_{a-opt})$ as a function of μ_0. (a-e) The optimal locations and energy norms for $\mu_0 = (0.41(\bigcirc), 0.56(\diamond), 0.71(\square)$ are indicated.

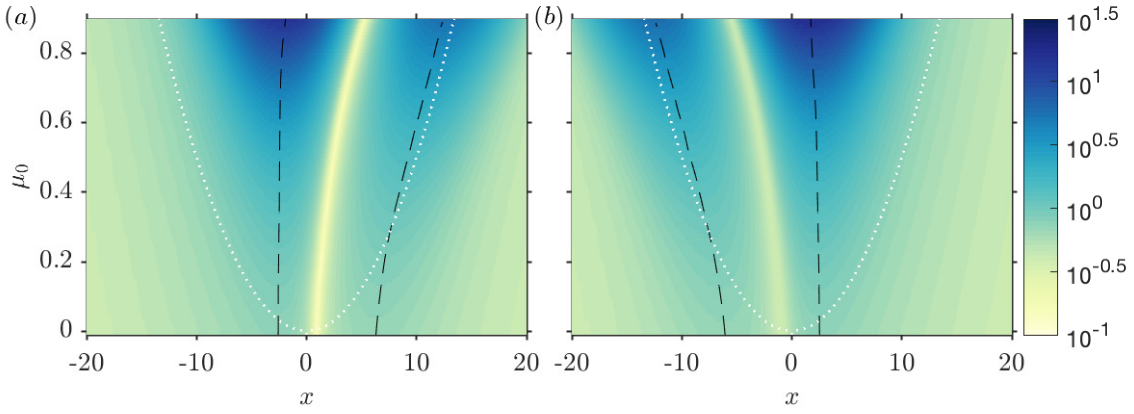

FIGURE 3.8: (a) ϵ_{OE} and (b) ϵ_{FI} as a function of x for a range of μ_0. Optimal placements from Figure 3.7(c) are used. The locations corresponding to the two peak values of ϵ_{OE} and ϵ_{FI} $(--)$ and the downstream boundary of the unstable region $(\cdots)$ are also shown.

and the optimal FIC energy norm $\gamma_{FI}(x_{a-opt})$ are shown as a function of μ_0. Over the chosen range γ_{OE} increases from 3.7 to 41.3, and γ_{FI} increases from 3.8 to 45.9.

It is now insightful to see how contributions to those norms are distributed throughout the domain. To do so, we use the root mean square (rms) value ϵ (see Appendix A.4 and Bagheri et al., 2009), defined such that

$$\gamma^2 = \int_{-\infty}^{\infty} \epsilon^2(x) dx. \tag{3.8}$$

The term ϵ_{OE} shows the effect of the estimation error on γ_{OE} throughout the domain. Figure 3.8(a) uses the optimal sensor locations from figure 3.7(c) to calculate ϵ_{OE} for a range of μ_0. As expected, the smallest ϵ_{OE} occurs at the location of the sensor for all μ_0. The most significant contributions to the estimation error are concentrated in two regions: near the centre of the domain and near X_{II}.

Similarly, the term ϵ_{FI} shows the effect of the disturbances on γ_{FI} throughout the domain. Figure 3.8(b) uses the optimal actuator locations from figure 3.7(c) to calculate ϵ_{FI} for a range of μ_0. The results of figure 3.8(b) are approximately symmetric to figure 3.8(a). It is interesting to note that the estimator is the *dual* of the state feedback controller (Aström and Murray, 2010). Therefore equating the control weight with the sensor noise ($v = \alpha$, instead of $v = 10^{-3}$ and $\alpha = 1/7$) would result in $x_{s-opt} = -x_{a-opt}$ and an exact symmetry between ϵ_{OE} and ϵ_{FI}.

3.5.2 The IOC problem

The results of the OE and FIC problems are relevant for understanding the challenges of sensing and actuating each on their own. However, we cannot use the OE problem for control itself, and in most fluid flows the full-state information needed for FIC is unavailable. Therefore, we now combine OE with FIC to form the input–output control (IOC) problem. We will see that similar results to the OE and the FIC problems are obtained.

As in §3.5.1, we start with a single value of $\mu_0 = 0.41$ with random disturbances applied everywhere in the domain. This time we must consider the sensor (x_s) and actuator (x_a) location together, which adds an extra dimension to the problem. The energy norm γ_{IO} is therefore obtained over a range of sensor locations (x_s) and actuator locations (x_a) and mapped out on a contour plot in figure 3.9(a). A minimum of $\gamma_{IO} = 6.68$ is achieved for $x_s = 1.09$ and $x_a = -1.12$. (These results are consistent with Chen and Rowley (2011).) As before, placing the sensor upstream of its optimal location is penalised more severely than placing it downstream. Similarly, placing the actuator downstream of its optimal location is penalised more severely than placing it upstream. These behaviours match those seen for the OE and FIC problems. We repeat the brute force result for $\mu_0 = 0.56$ and $\mu_0 = 0.71$ in figure 3.9(b,c), where a minimum of $\gamma_{IO} = 12.64$ and $\gamma_{IO} = 52.11$ is achieved. Local maxima and rapid changes of γ_{IO} are observed at the same locations as for the OE problem and the FIC problem.

Finding the optimum via brute force is computationally expensive – particularly now that the optimisation problem is two-dimensional (with both the sensor and actuator to be chosen simultaneously). Therefore we use the gradient minimisation algorithm of Chen and Rowley (2011) to find the optimal sensor x_{s-opt} location and the optimal actuator x_{a-opt} location – each as a function of μ_0.

Figure 3.9(d) shows that x_{s-opt} shifts downstream from 0.24 to 5.13, while x_{a-opt} shifts upstream from -0.33 to -5.13, over the chosen range of $-0.01 \leq \mu_0 \leq 0.9$. (The sensor and actuator are closer together in IOC than in OE and FIC.) The corresponding optimal positions' γ_{IO} are shown in figure 3.9(e). We can see that γ_{IO} increases from 3.8 to 1177.5, which is significantly larger than for either OE or FIC.

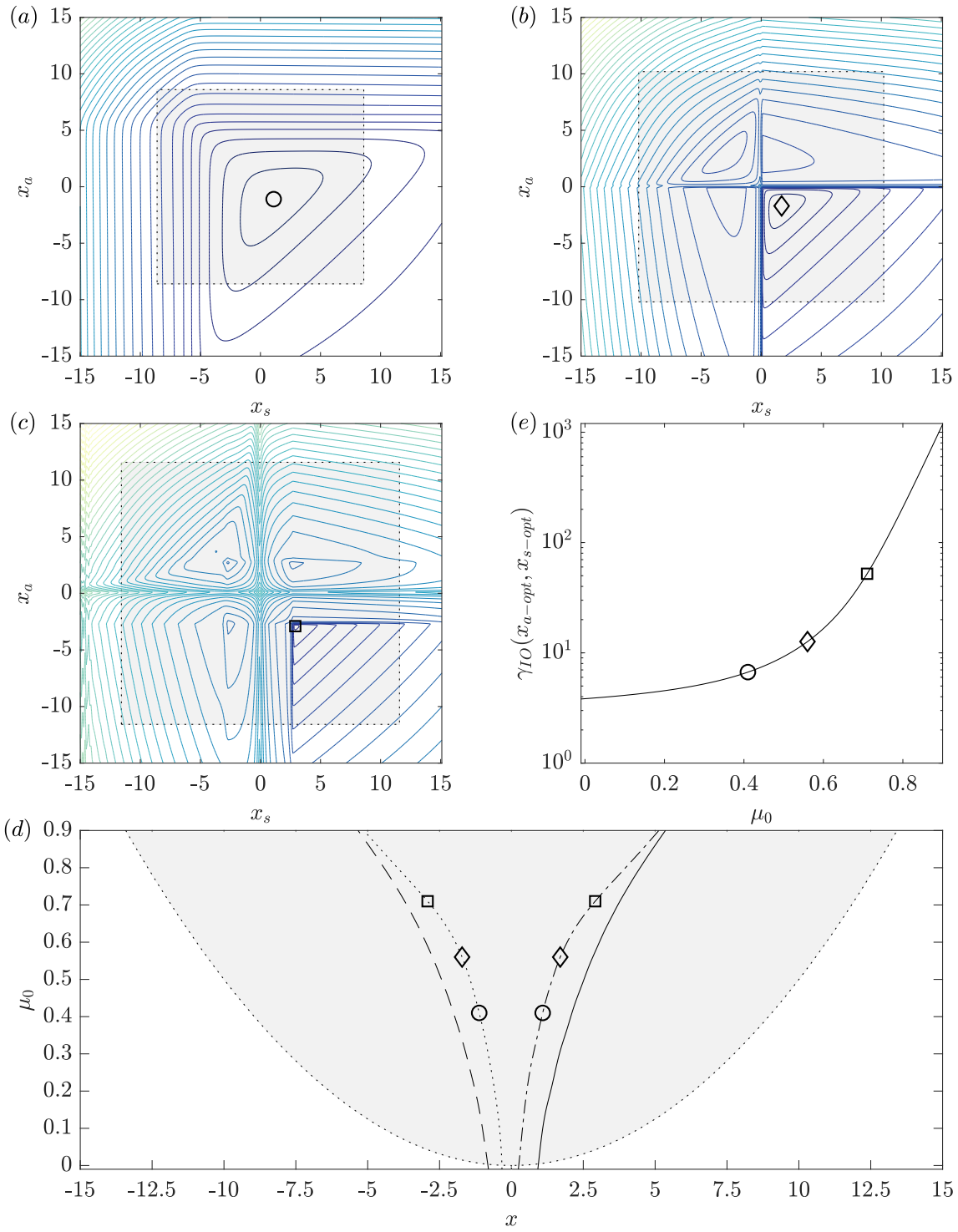

FIGURE 3.9: (a-c) Contours of the IOC norm γ_{IO} (Chen and Rowley, 2011), for $\mu_0 = (0.41(a), 0.56(b), 0.71(c))$, where the innermost contour is $\gamma_{IO} = (10^1(a), 10^{1.25}(b), 10^{1.75}(c))$, and each subsequent contour increments by $\times 10^{0.25}$. (d) the IOC optimal sensor $x_{s-opt}(-\cdot)$ and actuator $x_{a-opt}(:)$ location as a function of μ_0. The OE and FIC optimal locations are included $(—, --)$. (a-d) the unstable region is shaded grey (outer limits (:)); it only exists when $\mu_0 > 0$. (e) The IOC norm $\gamma_{IO}(x_{s-opt}, x_{a-opt})$ as a function of μ_0. (a-e) The optimal locations and energy norms for $\mu_0 = (0.41(\bigcirc), 0.56(\diamond), 0.71(\square)$ are indicated.

3.5.3 Discussion

We will now summarise and discuss the main findings.

We first used a brute force approach to generate the energy norm γ over a range of sensor and actuator locations. This was done for the OE and FIC problems in figure 3.7(a,b); and for the IOC problem in figure 3.9(a-c). Relating the results of figure 3.7(a,b) to the eigenmodes and adjoint eigenmodes, we see that the energy norm γ_{OE} is large at locations where an unstable eigenmode is small (see figure 3.2(a,c)), and that the energy norm γ_{FI} is large at locations where an unstable adjoint eigenmode is small (see figure 3.2(b,d)). A similar pattern is seen when comparing figure 3.9(a-c) with figure 3.2: that γ_{IO} is large at locations where either an unstable eigenmode or an unstable adjoint eigenmode is small. At these locations, the detectability or stabilisability is low, which limits estimation and control (see for example Skogestad and Postlethwaite, 2007; Chen and Rowley, 2015).

We are interested in the optimal sensor and actuator locations to achieve the best estimation and control performance possible. The brute force approach is inefficient when searching for the optimal sensor and actuator locations. Instead, we found them by employing the iterative minimisation algorithm of Chen and Rowley (2011). At first, we considered the OE and FIC problems in figure 3.7(c): as the stability decreases (μ_0 increases) the optimal sensor location x_{s-opt} shifts downstream, while the optimal actuator location x_{a-opt} shifts upstream. At the same time, the norms γ_{OE} and γ_{FI} in figure 3.7(d,e) rise sharply. Thus, there is a direct relationship between the stability, optimal location and the energy norm. (The behaviour of x_{a-opt} shifting upstream in the FIC problem is also observed by Lauga and Bewley (2003).) The IOC problem shows the same behaviour, although x_{s-opt} and x_{a-opt} are now closer together (figure 3.9(d)) and γ_{IO} is larger (figure 3.9(e)) relative to OE and FIC at a given stability.

An objective of this study is to better understand the optimal sensor and actuator locations we found, with a particular focus on any trade-offs. Therefore, we generated rms values (ϵ) of γ_{OE} and γ_{FI} throughout the domain for a set of stabilities in figure 3.8, placing the sensor and actuator at the respective optimal locations. This provides insight into the relationship between the optimal location, stability, and corresponding energy norm. Two peaks in ϵ_{OE} can be seen in figure 3.8(a): one near the centre of the domain and another near X_{II}. As μ_0 increases, the peak near

X_{II} shifts downstream. The sensor needs to be placed further downstream as well, to ensure that the two peaks are kept as small as possible. Keeping both peaks small is a trade-off in OE, which we further discuss in §3.6.1. Two peaks in ϵ_{FI} can be seen in figure 3.8(b): one near the centre of the domain and another near X_I. As μ_0 increases, the peak at X_I shifts further upstream. The actuator needs to be placed further upstream as well, to ensure that the two peaks are kept as small as possible. Just as in OE, keeping both peaks small is a trade-off in FIC. The two trade-offs we see in OE and FIC also exist in the IOC problem.

3.6 Trade-offs in optimal placement

We will now relate the optimal locations found in §3.5 to previous studies. This will highlight trade-offs that have to be considered, which were briefly mentioned in §3.5.3. Then, we explore some key factors limiting the sensor and actuator placement for effective estimation and control: the eigenmodes, adjoint eigenmodes, and time lag. Investigating the effect of time lag is particularly important due to the convective nature of the flow, and it will further highlight the effect of the trade-offs that have to be considered. Finally, we discuss the differences seen in the optimal placement results between OE, FIC and IOC.

3.6.1 Placement prediction

We now consider the optimal placements for OE and FIC at $\mu_0 = 0.41$ along with three placements based on previous literature: the most unstable eigenmode $\left(\phi_0\right)$ and adjoint eigenmode $\left(\psi_0\right)$, the wavemaker region (ζ_0) and the downstream (X_{II}) and upstream (X_I) branches of the unstable region. These are shown in figure 3.10 (see Åkervik et al., 2007; Giannetti and Luchini, 2007; Bagheri et al., 2009; Chen and Rowley, 2011, 2015). We see in figure 3.7(a,b) that the wavemaker region (ζ_0) provides the best prediction of the optimal placement. Still, the placement based on the wavemaker region does not perform as well as the optimal placement. To understand why, we will now study the ϵ_{OE} and ϵ_{FI} values for each of the four placements, which we display in figure 3.11.

In figure 3.11(a), for every placement case, there exist two peaks of ϵ_{OE}: one upstream of the sensor and one downstream of the sensor. The downstream peak

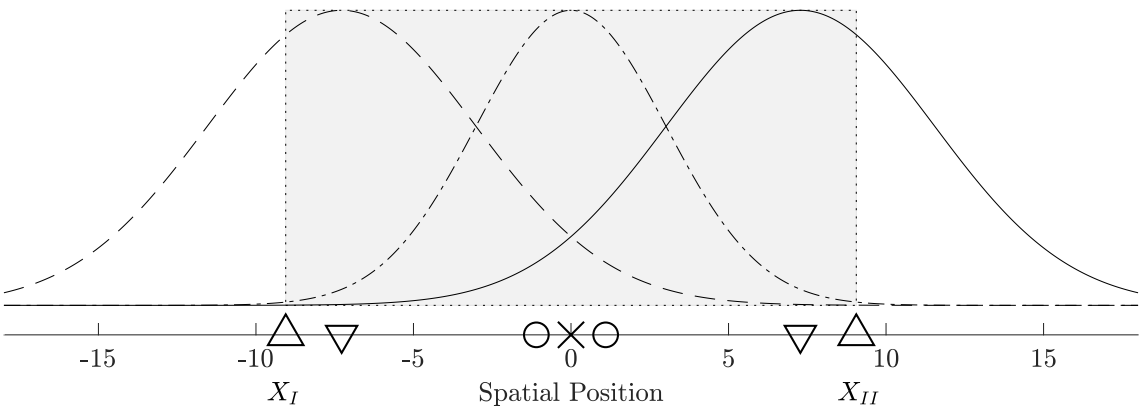

FIGURE 3.10: Selected actuator (upstream) and sensor (downstream) placements for $\mu_0 = 0.41$ based on previous literature: X_I and X_{II} ($\triangle$), ψ_0 and ϕ_0 ($\triangledown$), ζ_0 ($\times$), and $\mathcal{H}_2$-optimal ($\bigcirc$). The normalised most unstable eigenmode ϕ_0(—), the normalised most unstable adjoint-eigenmode ψ_0(−−), and their corresponding wavemaker region ζ_0(−·) are included. The unstable region, with upstream (X_I) and downstream (X_{II}) branch, is shown.

for the sensor placement at X_{II} is the smallest. However, the trade-off is that the upstream peak is the largest. The converse is true for wavemaker-based placement: the downstream peak is the largest, while the upstream peak is the smallest. The best trade-off is given by the $\mathcal{H}_2$-optimal placement. The optimal location provides the best compromise between keeping the upstream peak small and keeping the downstream peak small, which agrees with findings of Colburn (2011). At the optimal location, 59% of the energy contributed to γ_{OE} is from upstream of the sensor, and the remainder from downstream.

We can draw similar observations for FIC in 3.11(b): the optimal location provides the best compromise between keeping the upstream and downstream peak of ϵ_{FI} small.

3.6.2 The effect of eigenmodes and adjoint eigenmodes

We saw in §3.6.1 that the eigenmodes and adjoint eigenmodes fail to predict the optimal placement for estimation and control. They fail because of the non-normal, convective nature of the CGLE (e.g. Bagheri et al., 2009; Schmid and Henningson, 2012). Yet, they do show locations where a particular mode can be measured and actuated effectively. For example, both the second eigenmode $\left(\phi_1\right)$ and adjoint

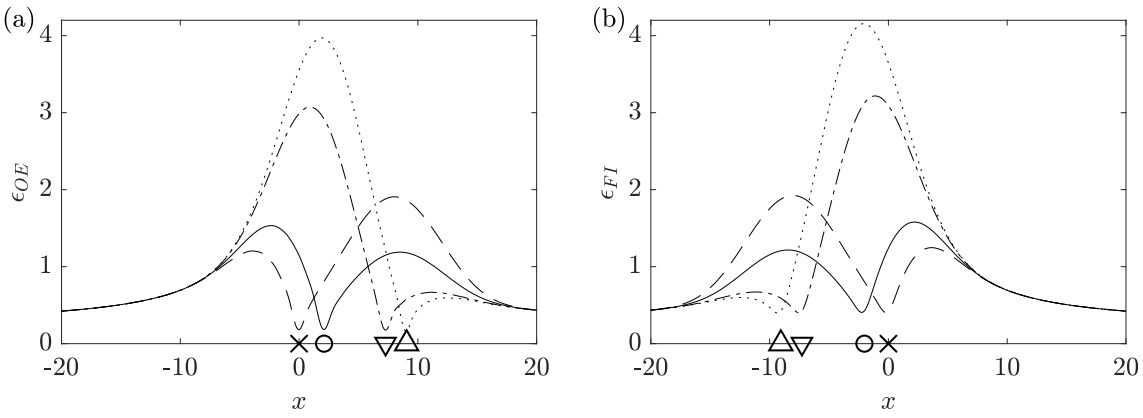

FIGURE 3.11: (a) ϵ_{OE}, and (b) ϵ_{FI}, as a function of x, for the four placements based on: X_{II} and X_I (:), ϕ_0 and ψ_0 ($\cdot-$), ζ_0 ($--$), and $\mathcal{H}_2$-optimal (—). The respective norms are: $\gamma_{OE} = (11.0, 8.7, 6.6, 5.7)$ and $\gamma_{FI} = (11.5, 9.1, 6.7, 5.9)$.

eigenmode (ψ_1) are zero at the domain's centre (figure 3.2). Therefore placement at the domain's centre ($x_s = x_a = 0$) results in poor performance when the second mode is unstable (see figures 3.7(a,b) and 3.9(a-c)). We illustrate this in figure 3.12, where we plot γ_{IO} as a function of μ_0 for $x_s = x_a = 0$ and compare it to γ_{IO} for the optimal placements. The placement at $x_s = x_a = 0$ performs similarly to the optimal placement as long as only one mode is unstable. There is a sharp increase in γ_{IO} when the second mode becomes unstable. Changing μ_0 from 0.55 to 0.56 increases γ_{IO} from 50.8 to 4949.1. (Similar changes are observed for OE and FIC.) One may ask why control does not become impossible in this case? The answer is that both the sensor and actuator have Gaussian profiles in space (see equation A.4), and therefore, sensing and actuation occur not just at $x = 0$, but also in its vicinity. This somewhat severe example helps to highlight the importance of the eigenmodes and adjoint eigenmodes. Placement without their consideration leads to poor performance.

3.6.3 The effect of time delay

Chen and Rowley (2011, 2015) pointed out the detrimental effect of excessive time lag, which causes the wavemaker region to be the best predictor of the optimal placement in section §3.6.1. To better understand and quantify the time-lag effect, we now introduce an artificial delay τ to either the sensor signal $\boldsymbol{y}$ (OE and IOC)

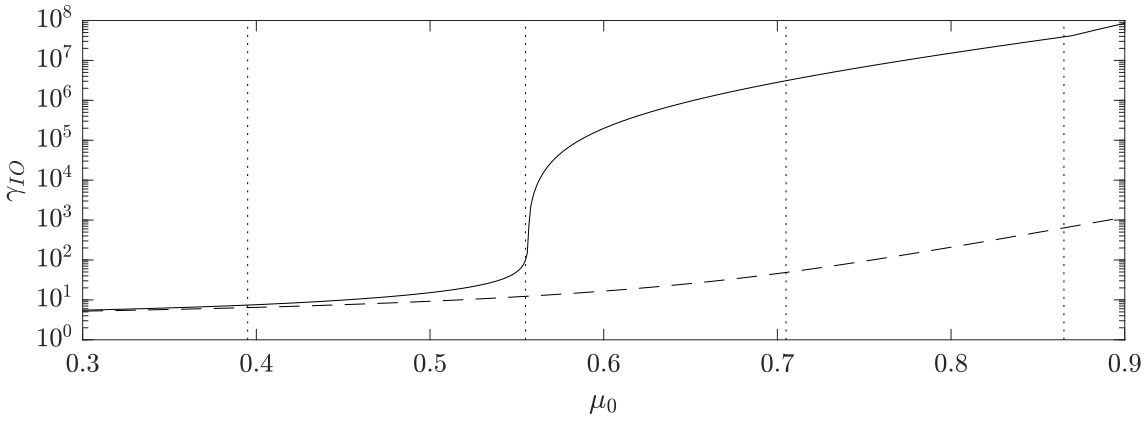

FIGURE 3.12: (a): Variation of γ_{IO} as a function of μ_0 when (x_s, x_a) is: $(0,0)(—)$ and $(x_{s-opt}, x_{a-opt})(--)$. The threshold of instability for the first four modes is indicated by $(\cdots)$ from left to right.

or the actuator signal $\boldsymbol{u}$ (FIC). The delay is introduced into the signals via a Padé approximation of order ten. Figure 3.13 shows the optimal sensor locations, the optimal actuator locations and the corresponding energy norms as a function of τ at $\mu_0 = 0.41$. The delay τ is normalised with U_{max} (the overall group velocity of the perturbations, see §3.3.1) to represent distance travelled by perturbations during the delay. With increasing τ the optimal sensor locations shift upstream, and the optimal actuator locations downstream, while the amount of spatial shift relative to $U_{max}\tau$ is similar. At the same time, the energy norms increase by 193% for OE, 196% for FI and 250% for IO over the given time-lag range.

The optimal sensor location moves further upstream to compensate for the artificial time lag in the measurement signal. The actuator moves further downstream to compensate for the delay in the feedback loop. These shifted optimal locations provide the best compromise between keeping the upstream and downstream peaks of the corresponding ϵ small (as discussed in §3.6.1) when subject to an artificial time lag. For a particular delay, the optimal sensor and actuator locations coincide with the peak of the wavemaker region.

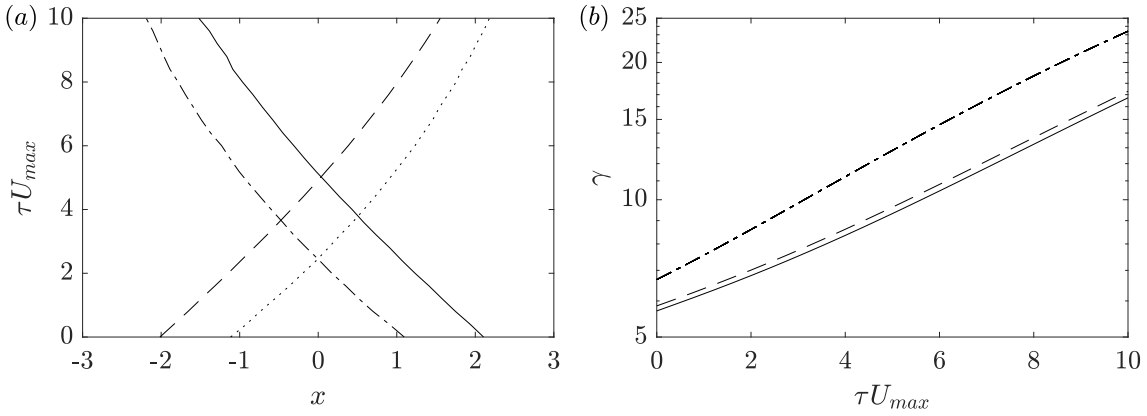

FIGURE 3.13: (a) The optimal sensor location (OE: $x_{s-opt}(—)$, IOC: $x_{s-opt}(-\cdot)$) and the optimal actuator location (FIC: $x_{a-opt}(--)$, IOC: $x_{a-opt}(\cdots)$) as a function of τU_{max} (delay scaled by the group velocity); (b) the corresponding, $\gamma_{OE}(—)$, $\gamma_{FI}(--)$, and $\gamma_{IO}(-\cdot)$.

3.6.4 The difference between the optimal placements of OE, FIC and IOC.

The separation principle of estimation and control states that when combining the independently designed optimal estimator, with the full information controller, the resulting input–output controller is still optimal. However, figure 3.9(d) shows that the optimal sensor and actuator locations for OE and FIC do not match the optimal sensor and actuator locations for IOC. This mismatch is because the separation principle only affects the estimator and controller design problem, but not the placement problem itself. It is essential to estimate perturbations which improve the control decision, hence the optimal sensor location for the IOC problem is closer to the centre of the domain than for OE problem. Similarly, it is essential to control perturbations which reduce the estimation error, and therefore, the optimal actuator location for the IOC problem is closer to the centre of the domain than for the FIC problem. Mathematically, the differences in optimal sensor and actuator placements can be explained by the gradients of γ^2 with respect to either the sensor or the actuator location. The gradients for IOC (Chen and Rowley, 2011) are different compared to the equivalent gradients for OE and FIC (equation A.5); therefore, the optimal placements must also be different.

3.7 Conclusion of chapter

Previous feedback flow control studies have placed sensors and actuators based on physical characteristics, such as eigenmodes. These physical characteristics are useful for understanding the limitations of effective estimation and control, but by themselves, they do not provide the whole picture. Instead, one has to search for the optimal locations iteratively, as done by Chen and Rowley (2011). We have studied the single sensor and single actuator placement problem in the complex Ginzburg-Landau equation over a range of stabilities. Specifically, we investigated any trade-offs present when searching for the optimal sensor and actuator locations.

The current study has made plain conflicting trade-offs. The sensor needs to be placed far enough downstream to estimate the most perturbed region of the domain; and far enough upstream to estimate the remaining domain. This trade-off causes the optimal sensor location to move downstream as the stability decreases. The actuator needs to be placed far enough upstream to control the region of the domain where the external disturbances have the greatest potential for amplification; and far enough downstream to control the remaining domain. This trade-off causes the optimal actuator location to move upstream as the stability decreases. When considering the sensor and actuator placement problem together, both trade-offs will also interact with each other, resulting in a slight shift in the optimal locations. Despite these relatively small differences between the optimal locations, we have observed a consistent trend in which the optimal sensor location moves downstream, and the optimal actuator location moves upstream with decreasing stability; conversely, these trade-offs cause a consistent trend in which the sensor moves upstream, and the actuator moves downstream with increasing time lag in measurement and actuation. It would be interesting to see if these trends are also observed in other convection-dominated spatially developing flows, such as jets and wakes. A future study could consider optimal sensor and actuator placement for control of vortex shedding over a range of Reynolds numbers.

Chapter 4

Linear estimation of coherent structures in wall-bounded turbulence at $\mathrm{Re}_\tau = 2000$[1]

4.1 Abstract

The estimation problem for a fully-developed turbulent channel flow at $\mathrm{Re}_\tau = 2000$ is considered. Specifically, a Kalman filter is designed using a Navier-Stokes-based linear model. The estimator uses time-resolved velocity measurements at a single wall-normal location (provided by DNS) to estimate the time-resolved velocity field at other wall-normal locations. The estimator is able to reproduce the largest scales with reasonable accuracy for a range of wavenumber pairs, measurement locations and estimation locations. Importantly, the linear model is also able to predict with reasonable accuracy the performance that will be achieved by the estimator when applied to DNS. A more practical estimation scheme, which uses the shear stress at the wall as measurement, is also considered. The estimator is still able to estimate the largest scales with reasonable accuracy, although the estimator's performance is reduced.

[1]Based on Oehler, S., Garcia-Gutiérrez, A. and Illingworth, S. (2018), 'Linear estimation of coherent structures in wall-bounded turbulence at $\mathrm{Re}_\tau = 2000$', *J. Phys. Conf. Ser.* **1001**, 012006.

4.2 Introduction

Linear estimation has been used to successfully detect perturbations and coherent structures in wall-bounded shear flows at laminar (Joshi et al., 1997; Hœpffner et al., 2005; Naguib et al., 2010), transitional (McKernan et al., 2007; Jones et al., 2011; Bagheri and Henningson, 2011), and turbulent (Chevalier et al., 2006; Illingworth et al., 2018) Reynolds numbers. Estimation is useful for obtaining information about quantities that cannot be measured directly and can provide feedback in a control set-up. The design of a linear estimator is a well-understood topic in control theory, and therefore, the implementation is relatively straightforward. However, a model of the flow is required. A suitable model for this purpose is the linearized Navier-Stokes equations.

Previous studies have analyzed the linearized Navier-Stokes equations to understand the growth and decay of perturbations. The majority of studies have focused on *laminar* shear flows by considering the temporal development of small perturbations about the laminar velocity profile; and the response to external forcing (Farrell and Ioannou, 1993, 1996; Jovanović and Bamieh, 2001; Jovanović and Bamieh, 2005). Of particular significance was the realization that, even for stable flows, perturbations can experience significant transient growth before ultimately decaying (Gustavsson, 1991; Schmid and Henningson, 2012). Linear modeling for *fully-developed* turbulent shear flows, although able to claim a relatively long history (Malkus, 1956; Reynolds and Hussain, 1972), has received less attention. In recent years, though, there has been a renewed interest in linear models for turbulent shear flows, motivated by increasing evidence that linear mechanisms play an important role here as well.

Existing research on linear mechanisms in fully-developed turbulent shear flows can be divided into two broad camps: those that, following earlier work (Reynolds and Tiederman, 1967), include an eddy viscosity in the linear operator (del Alamo and Jiménez, 2006; Pujals et al., 2009; Hwang and Cossu, 2010*b*,*a*); and those that do not (McKeon and Sharma, 2010; McKeon et al., 2013; Moarref et al., 2013, 2014).

This study investigates model-based estimation of channel flow at $Re_\tau = 2000$ using a linear, Navier-Stokes-based model (introduced in §2). The estimator uses time-resolved velocity measurements (or shear-stress measurements) at a single wall-normal location to estimate the time-resolved velocity field at other wall-normal

locations. Like many previous studies (Reynolds and Tiederman, 1967; del Alamo and Jiménez, 2006; Pujals et al., 2009; Hwang and Cossu, 2010*a*,*b*) the model includes an eddy viscosity in the linear operator; but in contrast to them it does not discard the remaining nonlinear terms, instead absorbing them into an unknown (but non-zero) forcing term following McKeon and Sharma (2010).

The work is composed of three parts. The first part of the study serves to consolidate earlier results (Illingworth et al., 2018) that were obtained for channel flow at $\mathrm{Re}_\tau = 1000$. The present study builds on that work in three ways. First, applying the techniques to a different dataset at a different Reynolds number provides an important consolidation and confirmation of those earlier results. Second, with access to significantly more time-resolved data at $\mathrm{Re}_\tau = 2000$, we obtain significantly better convergence in the results. This will be of particular importance when comparing the results obtained in DNS with those predicted by the linear model. Third, with access to all wall-normal locations, we can compare velocity fields not only in single wall-normal planes (as done in Illingworth et al. (2018)) but also across all wall-normal heights. This allows us to qualitatively assess the structures that are estimated by the linear model when it knows only the time-resolved velocity field at a single wall-normal height. In the second part of the study, we look at making the measurement scheme more practical. Measuring the velocity in the interior of a flow is difficult to achieve experimentally. For this reason, wall-mounted shear stress measurements have been used in a number of previous studies on flow estimation and flow control (e.g. Joshi et al., 1997; Bewley and Liu, 1998; Hœpffner et al., 2005; Chevalier et al., 2006; Bagheri and Henningson, 2011; Åkervik et al., 2007; McKernan et al., 2007; Naguib et al., 2010; Jones et al., 2011, 2015). Therefore, in the second part of the study, we replace the (less practical) velocity measurements used in the first part with (more practical) wall shear stress measurements. Having looked at estimator performance at individual wall-normal heights in the first two parts, the third and final part looks at estimator performance over a range of estimation and measurement planes (for velocity measurements only). Specifically, we quantify the estimator performance for all pairs of measurement and estimation locations over the entire channel half-height. Although less practical (since the sensor could be anywhere), this is interesting because it shows us what is possible with a single sensor.

4.3 Methods

4.3.1 Linear model

We consider a fully developed turbulent channel flow at $\mathrm{Re}_\tau = 2000$. Here, Re_τ is the friction Reynolds number defined as $u_\tau h/\nu$, where ν is the kinematic viscosity, $h = 1$ the channel half height, $u_\tau = \sqrt{\tau_w/\rho}$ the friction velocity, τ_w the wall shear stress, and ρ the density. Thus, the spatial variables are normalised by h, wavenumbers by $1/h$, velocities by u_τ, time by h/u_τ and the pressure p by ρu_τ^2. The streamwise, spanwise, and wall-normal spatial coordinates of the flow are represented by $[x, y, z]$ and velocities by $\boldsymbol{u} = [u, v, w]$. We assume zero initial conditions and apply no-slip boundary conditions.

The channel flow dynamics are represented by a linear model for perturbations ($\boldsymbol{u}$) about a fully-developed mean velocity profile ($\boldsymbol{U} = \big(U(z), 0, 0\big)$, as done in del Alamo and Jiménez (2006) and Pujals et al. (2009)):

$$\frac{\partial \boldsymbol{u}}{\partial t} = -\left(\boldsymbol{U}\cdot\nabla\right)\boldsymbol{u} - \left(\boldsymbol{u}\cdot\nabla\right)\boldsymbol{U} - \nabla p + \nabla\cdot\left[\frac{\nu_T}{\nu}\left(\nabla\boldsymbol{u} + \nabla\boldsymbol{u}^T\right)\right] + \boldsymbol{d}, \quad \boldsymbol{u}\cdot\nabla = 0, \tag{4.1}$$

where $\nu_T(z)$ is the eddy viscosity profile, $\boldsymbol{d} = -(\boldsymbol{u}\cdot\nabla)\boldsymbol{u} + \overline{(\boldsymbol{u}\cdot\nabla)\boldsymbol{u}}$ contains all non-linear terms and $\bar{(\cdot)}$ represents the time-averaged mean. An analytical approximation of the eddy viscosity profile, as used in (del Alamo and Jiménez, 2006; Pujals et al., 2009; Moarref et al., 2013; Illingworth et al., 2018) is given by the relation:

$$\nu_T(z) = \frac{\nu}{2}\left(1 + \frac{\kappa^2\mathrm{Re}_\tau^2}{9}(2z - z^2)^2(3 - 4z + 2z^2)^2\left[1 - \exp\left(\frac{-\mathrm{Re}_\tau z}{A}\right)\right]^2\right)^{\frac{1}{2}} + \frac{\nu}{2}. \tag{4.2}$$

Integrating $\mathrm{Re}_\tau(1-z)\nu/\nu_T(z)$ provides the mean velocity profile $U(z)$ at Re_τ. The constants $\kappa = 0.426$ and $A = 25.4$ give the best fit to the mean velocity profile at $Re_\tau = 2003$ (Cess, 1958; Reynolds and Tiederman, 1967; Reynolds and Hussain, 1972).

4.3.2 Linear state-space model

We require a linear time-invariant state-space model, which allows us to design and implement a Kalman filter. We begin with the linear model introduced in §4.3.1, take the Fourier transforms in the homogeneous directions (x and y), and transform it into the Orr-Sommerfeld Squire form. The wall-normal direction is then discretised using Chebyshev collocation of order 151 (Weideman and Reddy, 2000). Convergence has been checked by doubling the number of grid points; this results in an error of 0.19% when measuring the energy of a randomly excited, uncontrolled flow. The state-space model at a single wavenumber pair is thus obtained as:

$$\dot{\boldsymbol{x}}(t) = \mathbf{A}\boldsymbol{x}(t) + \mathbf{B}_d\boldsymbol{d}(t), \tag{4.3a}$$

$$\boldsymbol{y}(t) = \mathbf{C}_y\boldsymbol{u}(t) + \boldsymbol{n}(t), \tag{4.3b}$$

$$\boldsymbol{z}(t) = \mathbf{C}_z\boldsymbol{u}(t), \tag{4.3c}$$

where $\boldsymbol{x} = [\hat{\boldsymbol{w}}, \hat{\boldsymbol{\eta}}]^T$ represents the wall-normal velocity and wall-normal vorticity, $\boldsymbol{u} = [\hat{\boldsymbol{u}}, \hat{\boldsymbol{v}}, \hat{\boldsymbol{w}}]^T$ the streamwise, spanwise, and wall-normal velocity, $\boldsymbol{y}$ a sensor reading contaminated by noise $\boldsymbol{n}$, $\boldsymbol{z}$ a quantity of interest, and $\boldsymbol{d} = \left[\hat{\boldsymbol{d}}_x, \hat{\boldsymbol{d}}_y, \hat{\boldsymbol{d}}_z\right]^T$ represents the non-linear effects (see §4.3.1). The boundary conditions are: $\hat{\boldsymbol{w}}_{wall}(t) = \hat{\boldsymbol{w}}'_{wall}(t) = \hat{\boldsymbol{\eta}}_{wall}(t) = 0$. For the purpose of the linear estimator design, the disturbances $\boldsymbol{d}$ and $\boldsymbol{n}$ are treated as unknown forcing that is white in space and time. It has been shown by Illingworth et al. (2018) that this assumption is realistic in conjunction with the eddy viscosity model. The sensor noise is chosen to be small enough (relative to the size of disturbances) that the estimation results are insensitive to it. The state-space model (equation (4.3)) can be expressed as a transfer function by using the Laplace transform:

$$\begin{bmatrix} \boldsymbol{y} \\ \boldsymbol{z} \end{bmatrix} = \mathbf{P}(s) \begin{bmatrix} \boldsymbol{d} \\ \boldsymbol{n} \end{bmatrix}. \tag{4.4}$$

See B.1 for a full definition of the state-space model.

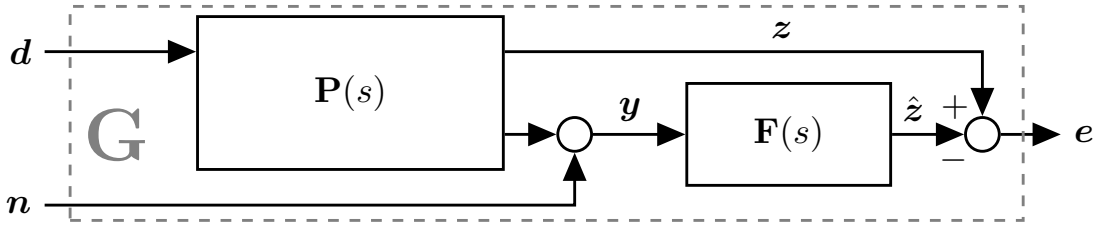

FIGURE 4.1: The combined Plant $\mathbf{P}(s)$ and Filter model $\mathbf{F}(s)$. The overall transfer function $\mathbf{G}(s)$ describes the input-output relationship of the estimation problem.

4.3.3 Linear estimator design

The linear time-invariant model, introduced in the previous section, allows us to design an estimator using common tools from control theory. We begin the estimator design process by stating the optimal estimation problem: given sensor measurements $\boldsymbol{y}$, which are contaminated by noise $\boldsymbol{n}$, estimate a quantity of interest $\boldsymbol{z}$. We use the plant model $\mathbf{P}(s)$ and the $\mathcal{H}_2$-optimal control framework to design the Kalman filter, which is denoted as $\mathbf{F}(s)$ in figure 4.1 (for example, see Seron et al. (1997)). The filter generates the estimate $\hat{\boldsymbol{z}}(s)$:

$$\hat{\boldsymbol{z}}(s) = \mathbf{F}(s)\boldsymbol{y}(s). \tag{4.5}$$

Combining $\mathbf{F}(s)$ with $\mathbf{P}(s)$ forms a new transfer function, $\mathbf{G}(s)$, as shown in figure 4.1. The estimation task can be summarized as: minimize the estimation error $\boldsymbol{e}(s)$ (equation (4.6)) in the presence of the exogenous inputs $\begin{bmatrix}\boldsymbol{d}(s) & \boldsymbol{n}(s)\end{bmatrix}^T$:

$$\boldsymbol{e}(s) = \boldsymbol{z}(s) - \hat{\boldsymbol{z}}(s) = \mathbf{G}(s)\begin{bmatrix}\boldsymbol{d}(s)\\ \boldsymbol{n}(s)\end{bmatrix}. \tag{4.6}$$

Now, the estimation design procedure can now be summarized as: given $\mathbf{P}(s)$, design $\mathbf{F}(s)$ such that $\mathbf{G}(s)$ is small. Thus, we quantify the size of $\mathbf{G}(s)$ via an $\mathcal{H}_2$-norm, which is defined as:

$$\|\mathbf{G}\|_2 = \sqrt{\frac{1}{2\pi}\int_{-\infty}^{\infty} \mathrm{Trace}[\mathbf{G}^*(\mathrm{j}\omega)\mathbf{G}(\mathrm{j}\omega)]d\omega} = \sqrt{\frac{1}{2\pi}\int_{-\infty}^{\infty} \sum_i (\sigma_i(\mathbf{G}(\mathrm{j}\omega)))^2 d\omega}, \tag{4.7}$$

TABLE 4.1: The $\mathrm{Re}_\tau = 2000$ channel flow spatial dimension.

	Size	Spacing	Resolved data	Smallest wavelength	Range
x:	8π	$\Delta k_x = 1/4$	65 wavenumbers	$\lambda_x \geq 2\pi h/8 \approx 0.785$	$\lvert k_x\rvert \leq 8$
y:	3π	$\Delta k_y = 2/3$	33 wavenumbers	$\lambda_y \geq 6\pi h/64 \approx 0.295$	$0 \leq k_y \leq 64/3$

TABLE 4.2: The $\mathrm{Re}_\tau = 2000$ channel flow temporal dimension used for estimation.

Re_τ	Δt	t_{max}	U_c	$U_c\Delta t$	$t_{max}U_c/(8\pi)$
2000	0.0111	12.72	24.37	0.272	12.33

where σ_i are the singular values of $\mathbf{G}$ at frequency ω. The singular values represent a transfer function's gain when there are multiple inputs and multiple outputs, and hence the $\mathcal{H}_2$-norm can be considered as an average gain over all frequencies and all directions.

4.3.4 DNS dataset

We require two sets of time-resolved DNS data: first, the velocity or shear stress fields in the measurement plane(s) to provide the input for the estimator, and second the velocity field in the estimation plane(s) to compare the estimates with the truth. These data sets are provided by the Polytechnic University of Madrid (UPM). They were generated by direct numerical simulations (DNS) performed for a channel flow at $Re_\tau = 2000$. The streamwise and spanwise directions are discretized by Fourier expansion, and the wall-normal direction is discretized using a compact difference scheme of 7th order. See table 4.1 for the details on the spatial dimensions and wavenumbers considered. Only positive spanwise wavenumbers (k_y) are considered, because the data is real-valued in physical space, and therefore, the coefficients for modes $(+k_x, +k_y)$ are the same as those for $(+k_x, -k_y)$ (Hoyas and Jiménez, 2006). The largest temporal frequency is approximated using Taylor's hypothesis as: $\omega_{max} = \max(|k_x|)U_c = 195$, where U_c is the velocity at the channel center, and $\max(|k_x|)$ the largest streamwise wavenumber considered in this study. We, therefore, have $2\pi/(\omega_{max}\Delta t) = 3$ samples per period for the highest frequency, which fulfills the Nyquist criterion. Refer to table 4.2 for the temporal dimensions. Full details of the DNS dataset can be found in (Hoyas and Jiménez, 2006; Encinar et al., 2018).

4.3.5 Estimator performance

The filter uses the sensor measurements $\boldsymbol{y}(t)$ from the DNS data set at a chosen wall-normal height and provides estimates $\hat{\boldsymbol{z}}(t)$ at different wall-normal heights by simulating the filter in time. The error $\boldsymbol{e}(t) = \boldsymbol{z}(t) - \hat{\boldsymbol{z}}(t)$ is then formed by comparing the true flow fields $\boldsymbol{z}(t)$ at the estimated wall-normal heights with their estimates $\hat{\boldsymbol{z}}(t)$. The 2-norm quantifies the performance, which is obtained by integrating the error in time: $\|\boldsymbol{e}\|_2 = [\int_0^{t_{max}} \boldsymbol{e}^*(t)\boldsymbol{e}(t)dt]^{1/2}$. It is normalised by $\|\boldsymbol{z}\|_2 = [\int_0^{t_{max}} \boldsymbol{z}^*(t)\boldsymbol{z}(t)dt]^{1/2}$ to form the performance parameter:

$$\gamma = \frac{\|\boldsymbol{e}\|_2}{\|\boldsymbol{z}\|_2} \tag{4.8}$$

We can also generate performance predictions γ_{pred} of the filter by taking $\|\mathbf{G}\|_2$ (equation (4.7)) and normalising it with $\|\mathbf{P}\|_2$. This is equivalent to taking sensor readings $\boldsymbol{y}(t)$ from the linear model itself, obtain estimates $\hat{\boldsymbol{z}}(t)$ with the filter, and then subtract the estimates from $\boldsymbol{z}(t)$.

4.4 Results

We now provide the linear estimator (described in §4.3.3) with time-resolved DNS data at a single wall-normal height and use it to estimate the time-resolved velocity at other wall-normal heights. In practice, this means forming an estimator for each of the $33 \times 65 = 2145$ wavenumber pairs of interest (see table 4.1).

4.4.1 Estimation in Physical space

We begin by looking at the estimator performance in physical space by comparing the estimate of the streamwise velocity with the true field from DNS. The filter is supplied with all three velocity components at a single wall height of $z = 0.2$ ($z^+ = 400$). Figure 4.2 compares the estimated streamwise velocity with the true field at $z = 0.1$ ($z^+ = 200$) at a single instant in time (parts (a) and (b)); and as a function of time for a single point in the plane (part (c)). Figure 4.3 repeats the analysis of figure 4.2, this time for a wall height of $z = 0.3$ ($z^+ = 600$). In

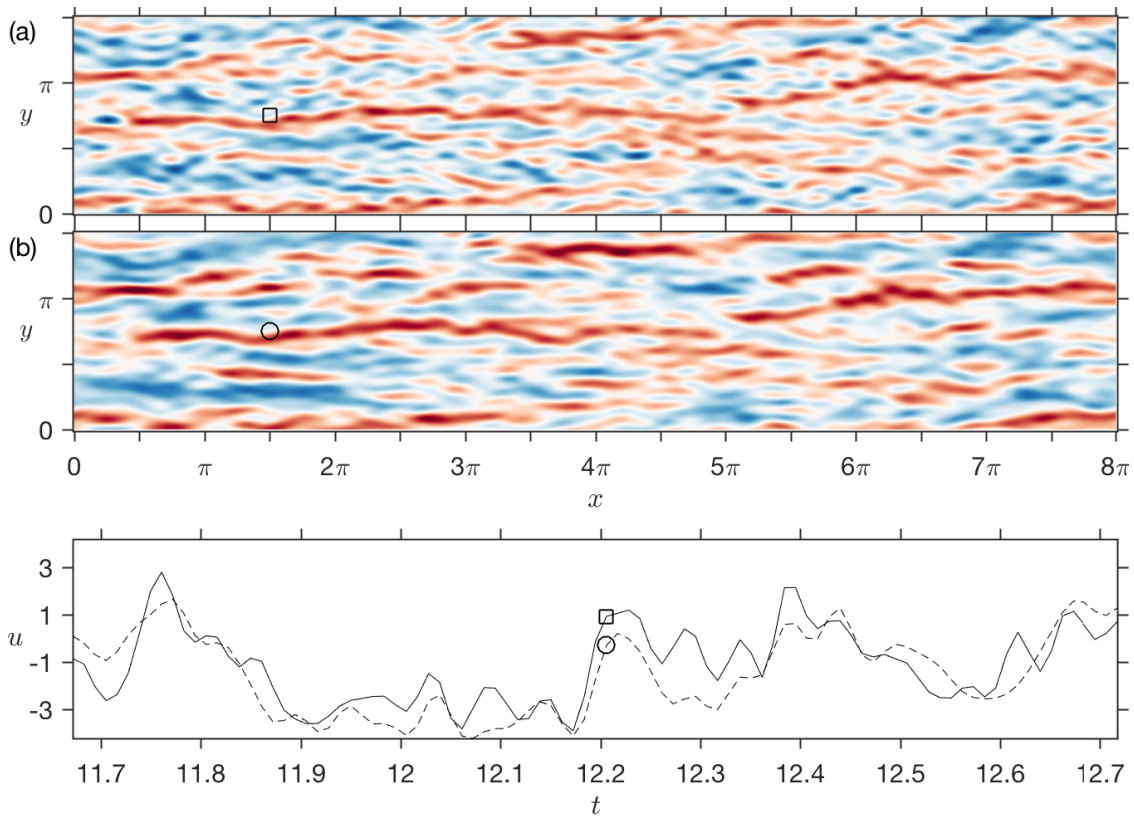

FIGURE 4.2: Estimation of the streamwise velocity perturbation at $z = 0.1$ ($z^+ = 200$) using the linear filter: (a) DNS data; and (b) linear estimate using measurements of all three velocity components at $z = 0.2$ ($z^+ = 400$); (c) time history at $x = 3\pi/2$, $y = 3\pi/4$ ($\square, \bigcirc$) for the DNS data (—) and for the linear estimate ($--$). Sixty-five contour levels are shown from $u = -5.5$ (red) to $u = +5.5$ (blue).

both figures, we see good agreement between the model-based estimate and the true velocity field.

To show how estimation performance varies with wall-normal distance in physical space, we have also included the streamwise velocity perturbations at $y = 3\pi/4$ in figure 4.4 and at $x = 3\pi/2$ in figure 4.5. Good agreement is seen between the model-based estimate and the true velocity field, but it reduces with distance from the sensor. The average magnitude of the streamwise velocity component is over-predicted when estimating near the wall. Similarly, it is under-predicted when estimating near the channel centre.

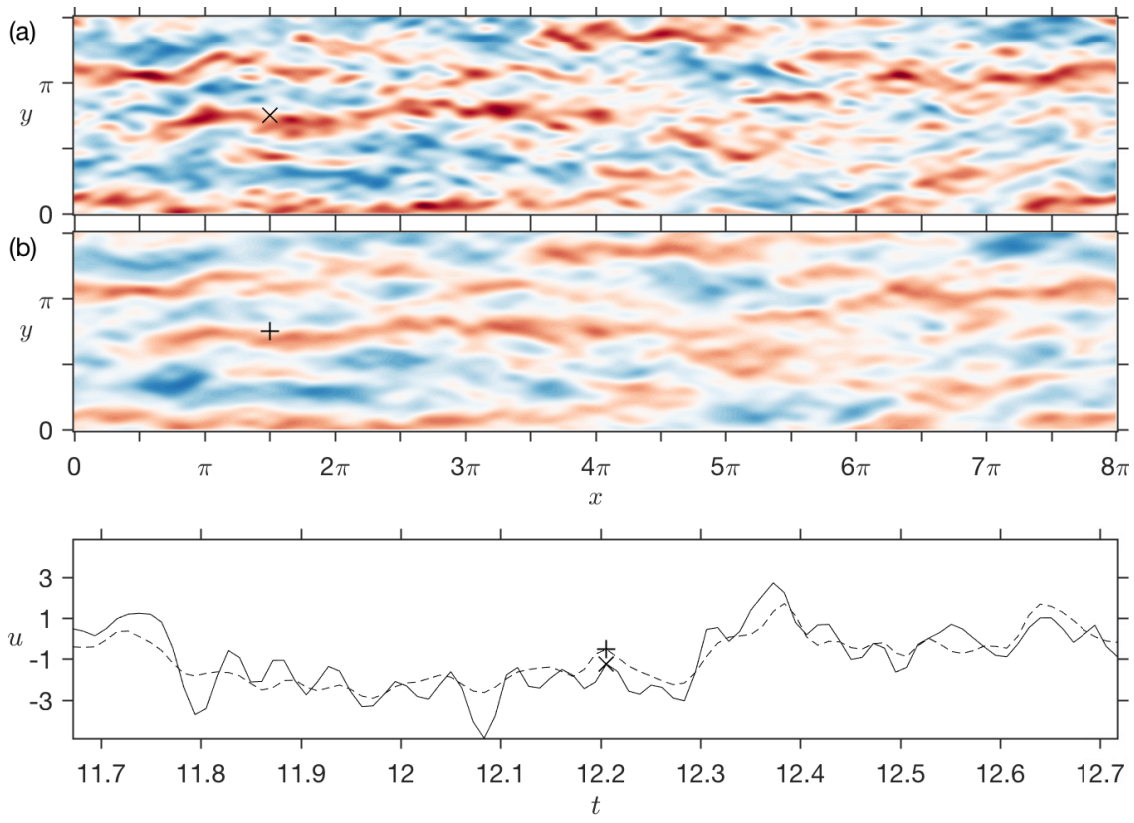

FIGURE 4.3: Estimation of the streamwise velocity perturbation at $z = 0.3$ ($z^+ = 600$) using the linear filter: (a) DNS data; and (b) linear estimate using measurements of all three velocity components at $z = 0.2$ ($z^+ = 400$); (c) time history at $x = 3\pi/2$, $y = 3\pi/4$ ($\times, +$) for the DNS data (—) and for the linear estimate ($--$). Sixty-five contour levels are shown from $u = -5.5$ (red) to $u = +5.5$ (blue).

4.4.2 Estimation in wavenumber space

We now provide a more quantitative assessment of the estimator by examining its performance across all wavenumber pairs of interest (see table 4.1). As in § 4.4.1, the estimator receives all three velocity components at $z = 0.2$ and uses them to estimate all three velocity components at $z = 0.1$ and $z = 0.3$.

Figure 4.6(a) plots γ as a function of the streamwise (k_x) and spanwise (k_y) wavenumber. In order to achieve better convergence, we calculate γ in each of the two halves of the channel and average over the two. The color scale is chosen to cover the range $[0, 0.7]$ to focus on the region over which the estimator performs

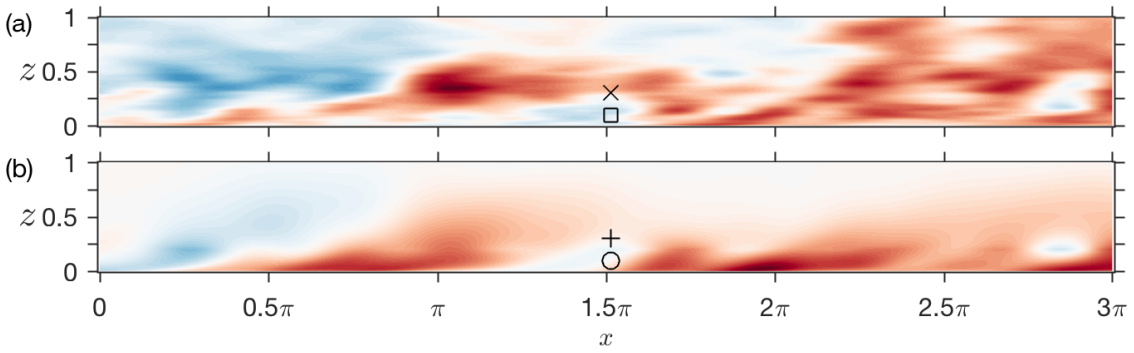

FIGURE 4.4: Estimation of the streamwise velocity perturbation at $y = 3\pi/4$ ($y^+ = 4712$) using the linear filter: (a) DNS data; and (b) linear estimate using measurements of all three velocity components at $z = 0.2$ ($z^+ = 400$). Sixty-five contour levels are shown from $u = -5.5$ (blue) to $u = +5.5$ (red).

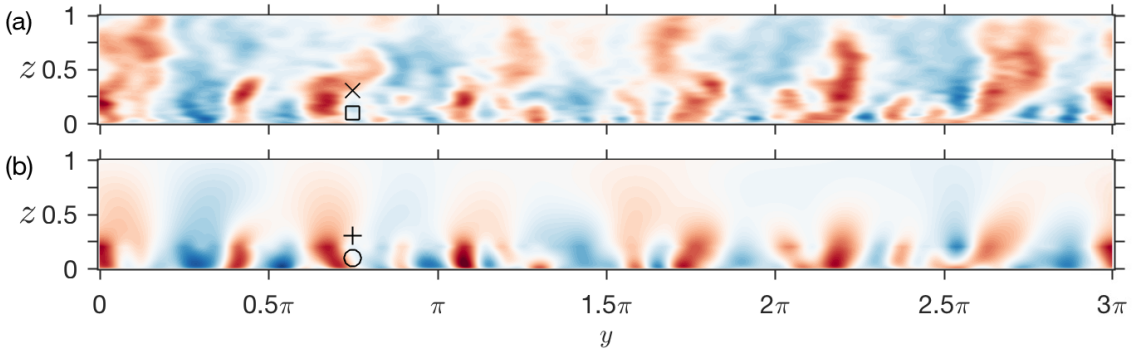

FIGURE 4.5: Estimation of the streamwise velocity perturbation at $x = 3\pi/2$ ($y^+ = 9425$) using the linear filter: (a) DNS data; and (b) linear estimate using measurements of all three velocity components at $z = 0.2$ ($z^+ = 400$). Sixty-five contour levels are shown from $u = -5.5$ (blue) to $u = +5.5$ (red).

well. (The maximum value of γ across all wavenumber pairs is 0.94.) We see that the estimator performs best for wavenumbers satisfying approximately $\|k_x\| \leq 2$ and $k_y \leq 10$.

By assuming that the unknown disturbances d are stochastic forces that are white in space and white in time, we can also calculate the *predicted* estimator performance, which we label γ_{pred}. For this predicted estimator performance, the filter is *designed* for the linear model, but also *applied* to the linear model, and thus the DNS data is not needed at all. The predicted estimator performance γ_{pred} is shown in figure 4.6(b), from which we see good agreement with the performance

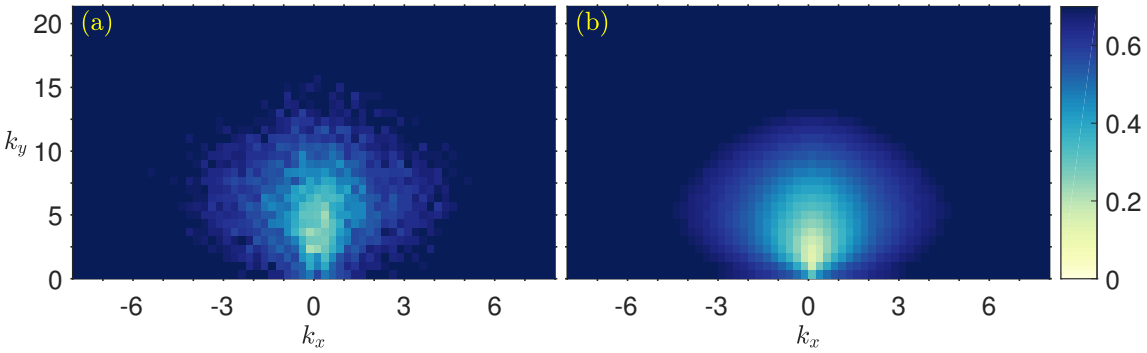

FIGURE 4.6: (a) Normalized estimation error γ as a function of (k_x, k_y) and (b) the prediction of the estimation error γ_{pred}. The estimator receives all three velocity components at $z = 0.2$ and uses them to estimate all three velocity components at $z = 0.1$ and $z = 0.3$. The same color scale $\gamma \in [0, 0.7]$ is used for both plots.

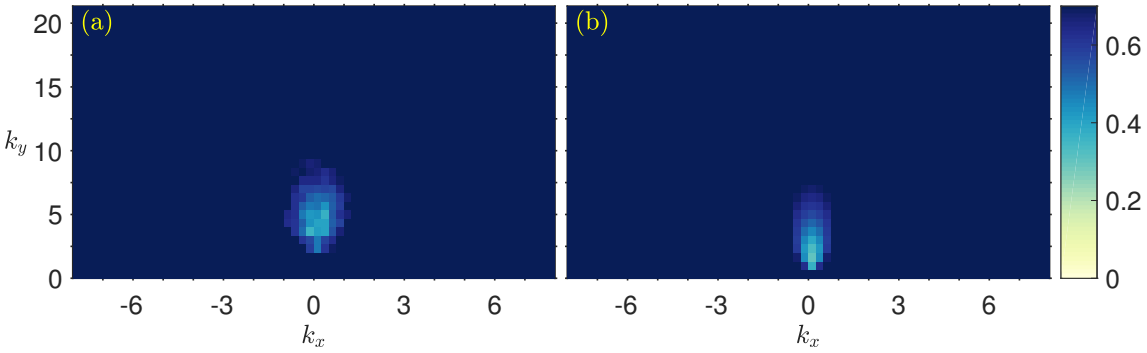

FIGURE 4.7: (a) Normalized estimation error γ as a function of (k_x, k_y) and (b) the prediction of the estimation error γ_{pred}. The estimator receives the streamwise shear stress component at the wall and uses it to estimate all three velocity components at $z = 0.1$ and $z = 0.3$. The same color scale $\gamma \in [0, 0.7]$ is used for both plots.

that is achieved in DNS. This is an encouraging result because it suggests that the physics of the largest scales are well-captured by the linear model.

4.4.3 Shear stress measurements

Velocity measurements inside the flow might not be available in an experimental set-up. Therefore, we now consider the performance of the estimator when its input is instead the streamwise wall shear stress τ_x (see B.1).

Figure 4.7 is a repeat of figure 4.6 for streamwise wall shear stress measurements. (The quantity estimated still represents all three velocity components at $z = 0.1$

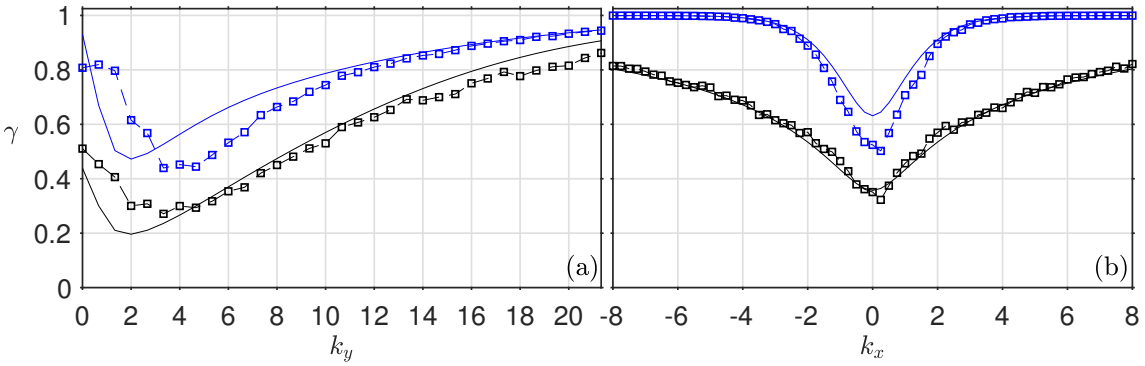

FIGURE 4.8: Normalized estimation error γ ($-\square-$) and its prediction γ_{pred}(—): (a) as a function of k_y averaged over all $k_x \leq |0.5|$; and (b) as a function of k_x averaged over all $4 \leq k_y \leq 8$. The set-up is the same as in figure 4.6 for the black results and in figure 4.7 for blue results. The DNS results have been averaged across the two halves of the channel.

and $z = 0.3$.) It is clear from figure 4.7 that the estimator performance is reduced significantly relative to figure 4.6 (i.e. relative to velocity measurements at $z = 0.2$).

To better compare results for these two measurement types, we now plot γ and its prediction γ_{pred} over a range of spanwise wavenumbers k_y for all $|k_x| \leq 0.5$. This comparison is shown in figure 4.8(a). The predicted performance, γ_{pred}, achieves its minimum for $1.4 < k_y < 2.1$, which is consistent with the results of Illingworth et al. (2018). This corresponds well with the range of k_y over which the potential for transient growth is greatest (Pujals et al., 2009); and over which the largest amplification is seen for both stochastic and harmonic forcing (Hwang and Cossu, 2010*a*). It appears, however, that the best performance (i.e. smallest γ) achieved by the estimator in DNS occurs at a slightly higher spanwise wavenumber of $k_y \approx 3.33$. In a similar way, in figure 4.8(b) we plot γ and γ_{pred}—this time as a function of the streamwise wavenumber k_x—for all k_y satisfying $4 \leq k_y \leq 8$ (again, averaged across these k_y to improve convergence). We see that, for both measurement types, the predicted performance agrees well with the performance actually achieved in DNS. For shear stress measurements, however, we do observe more significant differences between the predicted and true performance (up to 22% for the smallest values of $|k_x|$).

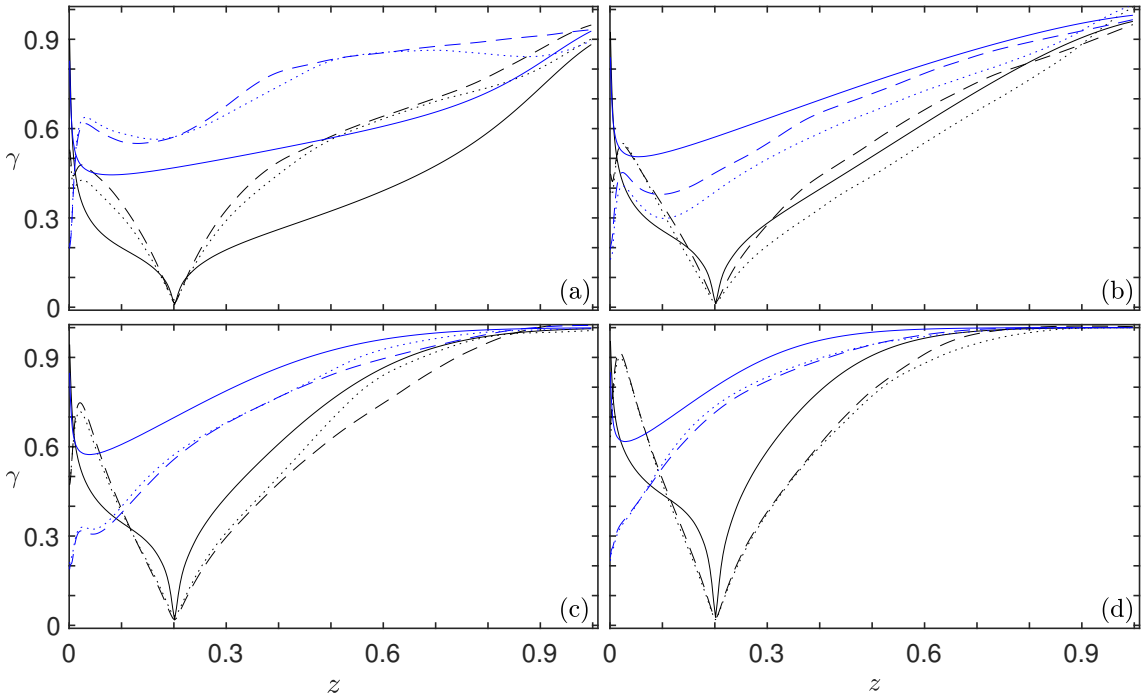

FIGURE 4.9: Normalized estimation error γ for the two halves of the channel $(--, \cdots)$ and its prediction γ_{pred} (—) as a function of wall normal estimation location z averaged over all $k_x \leq |0.5|$. This is plotted for (a) $k_y = 2$; (b) $k_y = 4$; (c) $k_y = 6$; (d) $k_y = 8$. The estimator measures either three velocity components (black) or the streamwise wall shear stress (blue).

4.4.4 Variation of estimation performance with wall-normal height

So far, we have looked at the estimator performance when the measurement location is fixed (at $z = 0.2$ or the wall) and when estimation is performed at $z = 0.1$ and $z = 0.3$. It is now interesting to investigate the estimator performance as these measurement and estimation locations are varied. To make the parameter space under consideration manageable, we will do this only for streamwise wavenumbers satisfying $|k_x| \leq 0.5$; and for four individual spanwise wavenumbers: $k_y = 2$, 4, 6 and 8.

We begin by fixing the measurement location at $z = 0.2$ as before, and plotting the variation of the estimator performance as the location of the (single) estimation plane is varied. This is shown in figure 4.9. We also show results when the measurement is instead the streamwise shear stress at the wall. The results are shown

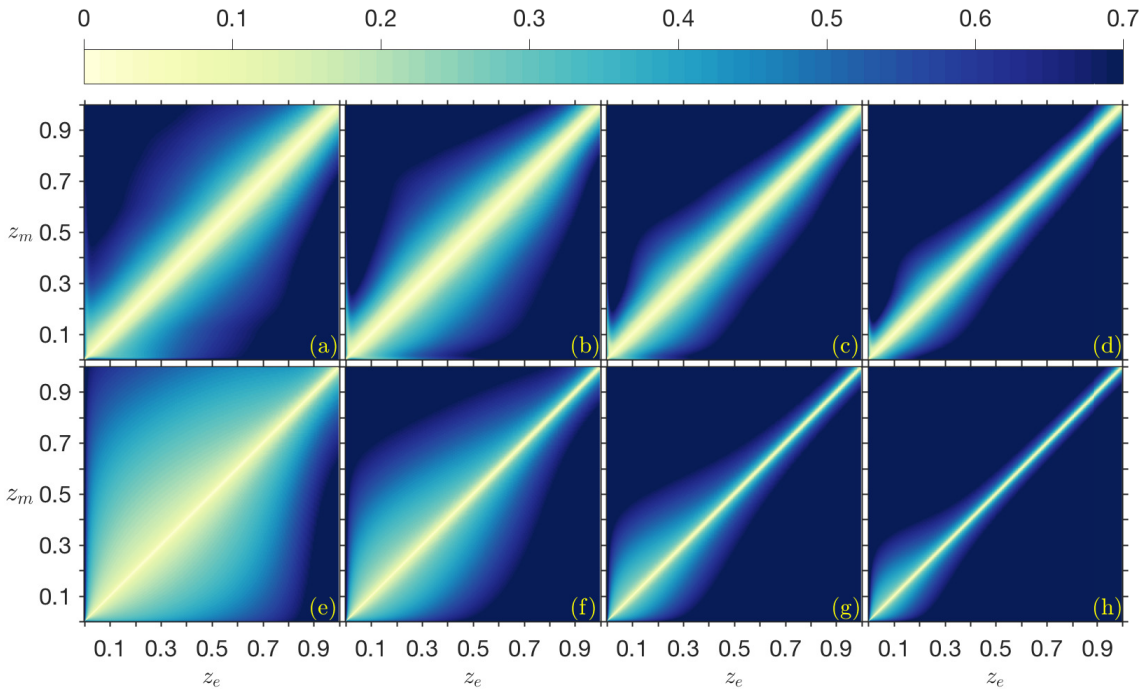

FIGURE 4.10: Normalized estimation error γ (top row) and its prediction γ_{pred} (bottom row) as function of the wall-normal measurement location z_m and the wall-normal estimation location z_e. This is plotted for (a,e) $k_y = 2$; (b,f) $k_y = 4$; (c,g) $k_y = 6$; (d,h) $k_y = 8$. All results are averaged over all $k_x \leq |0.5|$ and the two channel halves.

separately for the top half and bottom half of the channel to give some indication of the convergence of the results. We can make a number of observations that apply to all four spanwise wavenumbers: i) the best performance (obviously) occurs at the sensor location and decreases as we move away from it; ii) the worst performance occurs at the channel centre; iii) within the proximity of the measurement location, the true performance (γ) is always better than the predicted performance (γ_{pred}); and (iv) a local maximum of γ occurs in the logarithmic region at approximately $z = 0.025$ or $z^+ = 50$. An extra observation can be made for the $k_y = 2$ and $k_y = 4$ cases: (v) a local minimum of γ occurs in the buffer layer at approximately $z = 0.0075$ or $z^+ = 15$. This could be due to the wall signature of the (relatively large) eddies that are measured at certain measurement locations (Hoyas and Jiménez, 2006; Hutchins and Marusic, 2007*a*).

Having fixed the measurement location for the velocity sensor at a single plane,

we can now also vary it by adding a third dimension. This is shown in figure 4.10, where the estimator performance γ is plotted as a function of *both* the measurement location z_m and the estimation location z_e. As one would expect, the best performance is achieved when the measurement and estimation locations coincide, i.e. when $z_e = z_m$. It is interesting that, for estimation locations in the vicinity of a given measurement location, the true estimator performance (γ) is in general smaller (i.e. better) than that predicted by the linear model (γ_{pred}).

4.5 Discussion

We now give some broader discussion on the results obtained for the two measurement types considered (i.e. velocity measurements and wall shear stress measurements).

Using velocity measurements at a single wall-normal location, we are able to estimate the flow at other wall-normal locations with reasonable accuracy, as demonstrated in figures 4.2 - 4.6. This is consistent with the results observed in an earlier study by Illingworth et al. (2018) at $\mathrm{Re}_\tau = 1000$. The present study at $\mathrm{Re}_\tau = 2000$, however, benefits from the availability of significantly more time-resolved DNS data at more wall heights. We see significantly improved convergence in the normalized estimation error (γ) in figure 4.6. Importantly, the linear model (equation (4.1)) not only achieves good estimation performance but is also able to predict the range of wavenumber pairs (figures 4.6 and 4.8) and the range of wall heights (figures 4.9 and 4.10) over which the estimator should perform well. In this respect, the results in figure 4.6—which perhaps benefit most from the improved convergence described above—are particularly encouraging. Together, these results suggest that, for the largest scales considered, linear mechanisms are important, and that they are well-represented by the linear model.

By measuring instead the wall shear stress, it is still possible to achieve reasonable estimation performance for the largest scales. However, it is clear in figures 4.6 and 4.7 that the estimator is significantly less successful than its velocity-based counterpart. This finding is consistent with studies carried out for laminar profiles (Bewley and Liu, 1998; Hœpffner et al., 2005): the leading eigenvector of the linear

system includes several centred modes, with little support near the wall. (The modeshapes are only weak functions of Reynolds number.)

We also observe in figure 4.8 that the agreement between the true estimator performance (γ) and its prediction (γ_{pred}) is not as good as that seen for velocity measurements. This is an interesting observation, the cause of which is still under investigation. One possibility is that, for wall-based measurements, the assumption on $\boldsymbol{d}$ in equation (4.1) of delta-correlated forcing (in space and in time) is less appropriate—in other words, that second-order statistics become more important. Zare et al. (2017) have recently considered colored forcing in the linearized Navier Stokes equation to reproduce second-order dynamics. It would be interesting to see if this modified linear model is able to improve i) the estimator performance and ii) the agreement between the estimator performance (γ) and its prediction (γ_{pred})—both for velocity measurements and for wall shear stress measurements.

4.6 Conclusions of chapter

A linear Navier–Stokes-based model has been used to design a Kalman filter for a fully-developed turbulent channel flow. The Kalman filter is able to estimate the largest scales with reasonable accuracy at $\mathrm{Re}_\tau = 2000$. The results build on earlier work (Illingworth et al., 2018) that was performed at $\mathrm{Re}_\tau = 1000$, and for which significantly less time-resolved data at significantly fewer wall-normal locations were available. Using velocity measurements as input, the estimator is able to estimate the largest scales with reasonable accuracy for a range of wavenumber pairs, measurement planes, and estimation planes. Furthermore there is good agreement between the performance predicted by the model and the performance actually achieved in DNS. Using wall shear stress measurements as input, the estimator is still able to estimate the largest scales with reasonable accuracy, although the estimator's performance is significantly reduced relative to the velocity-based estimator. The results warrant further research on the linear model and its applications.

Chapter 5

Sensor and actuator placement in wall-bounded turbulence at $\mathrm{Re}_\tau = 2000$[1]

5.1 Abstract

We study the estimation and control problems for a fully-developed turbulent channel flow at $\mathrm{Re}_\tau = 2000$ with a focus on the largest scales ($[k_x \leq |0.5|, k_y \leq |6|]$). We anticipate that these scales will be the easiest to estimate and control. A Navier-Stokes-based linear model (which includes an eddy viscosity in the linear operator) is employed to design estimators and feedback controllers. We determine where sensors and actuators are most effective in two ways: first, by placing them some distance off the wall; and second, by placing them at the wall. The work is in three parts. First, we consider the optimal estimation problem in which a Kalman filter uses time-resolved measurements at a single wall-normal location (provided by DNS) to estimate the time-resolved streamwise velocity perturbations at other wall-normal locations. The estimator reproduces the velocity perturbations with reasonable accuracy for a range of measurement and estimation locations; the linear model is also able to predict with reasonable accuracy the performance that will be

[1]Based on Oehler, S. F., and Illingworth, S. J. (2018), 'Linear estimation and control of coherent structures in wall-bounded turbulence at $\mathrm{Re}_\tau = 2000$', *in* '21st Australasian Fluid Mechanics Conference', AFMS.

achieved by the estimator. Second, we consider the linear full information control problem in which the entire flow field is known; but actuation is at only a single wall-normal location. The linear model predicts that control is effective in reducing the streamwise velocity perturbations throughout the channel for a wide range of actuator locations. Third, we consider the linear input-output control problem with time-resolved measurements at only a single wall-normal location; and actuation at only a single wall-normal location.

5.2 Introduction

We consider a statistically steady incompressible turbulent channel flow at a friction Reynolds number $\mathrm{Re}_\tau = u_\tau h/\nu = 2000$, where ν is the kinematic viscosity, h the channel half-height, $u_\tau = \sqrt{\tau_w/\rho}$ the friction velocity, τ_w the wall shear stress, and ρ the density. Streamwise, spanwise, and wall-normal spatial coordinates are denoted by $[x, y, z]$ and the corresponding velocities by $\boldsymbol{u} = [u, v, w]$. We assume zero initial conditions and apply no-slip boundary conditions. Spatial variables are normalised by h, wavenumbers by $1/h$, velocities by the friction velocity u_τ, time by h/u_τ and pressure p by ρu_τ^2. This non-dimensionalisation sets the channel half-height to $h = 1$ so that $z \in [0, 2h]$.

Our focus is on estimating and controlling the largest structures. A linear Navier-Stokes-based model is used to design estimators and controllers which employ sensors and actuators. It is interesting to consider if we should choose off-wall placements over more traditional at-wall placements for potential performance gains. Therefore, a particular focus of this work is a comparison between off-wall and at-wall sensors and between off-wall and at-wall actuators. For simplicity, we focus on estimation and control set-ups which employ either a single-plane sensor, a single-plane actuator, or both.

The structure of this chapter is as follows: §5.2 introduces the linear model (LM) and DNS data employed; §5.3 considers the optimal estimation (OE) problem, §5.4 the full information control (FIC) problem and §5.5 the input-output (IOC) control problem. (A summary of the three problems is given in figure 5.1). We finish with a discussion in §5.6 and conclusions in §5.7.

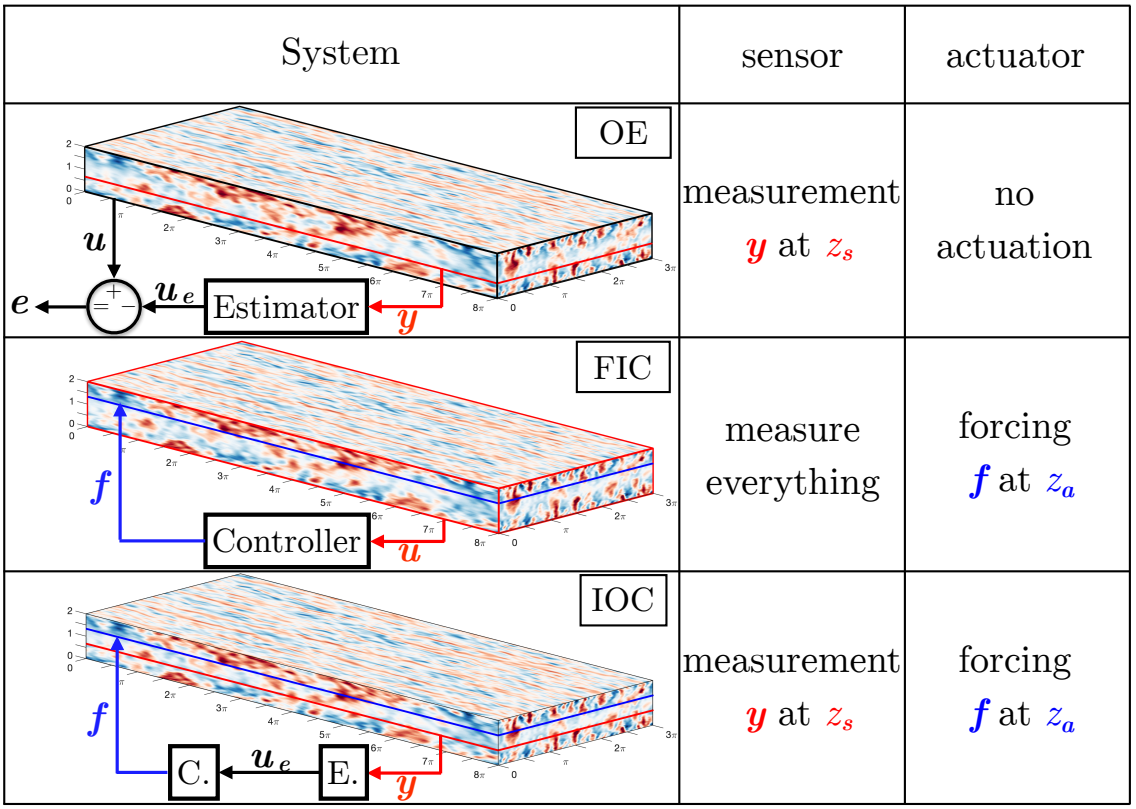

FIGURE 5.1: The OE, FIC, and IOC problems.

5.2.1 The direct numerical simulation (DNS) dataset[2]

We employ a direct numerical simulation (DNS) dataset provided by the Polytechnic University of Madrid (Hoyas and Jiménez, 2006; Encinar et al., 2018). The homogeneous streamwise and spanwise directions (extending $8\pi \times 3\pi$) are discretised by Fourier expansion (with a streamwise resolution of $\Delta k_x = 1/4$ and a spanwise resolution of $\Delta k_y = 2/3$), and the wall-normal direction is discretised using a compact difference scheme of 7th order. The data is real-valued in physical space, and therefore, the coefficients for modes $(k_x, +k_y)$ are the same as those for $(k_x, -k_y)$. We consider data for every $\delta t = 0.0111$ terminated at $t_{max} = 12.7$. A total of $t_{max}U_c/(8\pi) = 12.3$ channel flow-throughs ensures that any transients in the estimators and controllers are negligible (where U_c is the mean velocity at the channel

[2]This section is similar to §4.3.4 and §4.3.5.

centre). The largest temporal frequency is approximated using Taylor's hypothesis: $\omega_{max} = \max(|k_x|)U_c = 12.2$, where U_c is the velocity at the channel centre, and $\max(|k_x|)$ the largest streamwise wavenumber considered. Therefore, we have $2\pi/(\omega_{max}\Delta t) = 46.5$ samples per period for the highest frequency, which fulfils the Nyquist criterion.

To quantify the energy of the DNS data employed, we compute the 2−norm by integrating $\boldsymbol{u}^*\boldsymbol{u}$ in time and space:

$$\|\boldsymbol{u}\|_2 = \left[\int_0^{t_{max}} \left(\int_0^h \boldsymbol{u}^*(z,t)\boldsymbol{u}(z,t)dz\right) dt\right]^{1/2}, \tag{5.1}$$

which is the 2−norm for one channel half; and by integrating $\boldsymbol{u}^*\boldsymbol{u}$ in time only:

$$\|\boldsymbol{u}(z)\|_2 = \left[\int_0^{t_{max}} \boldsymbol{u}^*(z,t)\boldsymbol{u}(z,t)dt\right]^{1/2}, \tag{5.2}$$

which is the 2−norm at individual wall heights. All DNS based results are averaged for the top and bottom half of the channel.

5.2.2 The linear model (LM)[3]

Taking the incompressible Navier-Stokes equations we form a linear operator for the perturbations $\boldsymbol{u} = [u, v, w]$ about the turbulent mean flow $\boldsymbol{U} = [U(z), 0, 0]$, where the non-linear term $\boldsymbol{d} = -(\boldsymbol{u}\cdot\nabla)\boldsymbol{u} + \overline{(\boldsymbol{u}\cdot\nabla)\boldsymbol{u}}$ is treated as unknown forcing, $(\bar{\cdot})$ represents the time-averaged mean and an eddy viscosity $\nu_T(z)$ is introduced to model the effect of the incoherent motions (Reynolds and Hussain, 1972; del Alamo and Jiménez, 2006; Pujals et al., 2009):

$$\frac{\partial \boldsymbol{u}}{\partial t} = -\left(\boldsymbol{U}\cdot\nabla\right)\boldsymbol{u} - \left(\boldsymbol{u}\cdot\nabla\right)\boldsymbol{U} - \nabla p + \nabla\cdot\left[\frac{\nu_T}{\nu}(\nabla\boldsymbol{u} + \nabla\boldsymbol{u}^T)\right] + \boldsymbol{d}, \qquad \nabla\cdot\boldsymbol{u} = 0. \tag{5.3}$$

An analytical fit is used (Cess, 1958) for the eddy viscosity profile ν_T as in previous studies (Pujals et al., 2009; del Alamo and Jiménez, 2006; Moarref and

[3]This section is similar to §4.3.1 and §4.3.2.

Jovanović, 2012; Illingworth et al., 2018):

$$\nu_T(z) = \frac{\nu}{2}\left\{1 + \frac{\kappa^2 \mathrm{Re}_\tau^2}{9}(2z - z^2)^2(3 - 4z + 2z^2)^2 \times \left[1 - \exp\left(\frac{-\mathrm{Re}_\tau z}{A}\right)\right]^2\right\}^{1/2} + \frac{\nu}{2}. \tag{5.4}$$

Integrating $\mathrm{Re}_\tau(1-z)\nu/\nu_T(z)$ provides the mean velocity profile $U(z)$ at Re_τ. The constants $\kappa = 0.426$ and $A = 25.4$ give the best fit to the mean velocity profile at $\mathrm{Re}_\tau = 2003$ (del Alamo and Jiménez, 2006).

We take Fourier transforms in the homogeneous directions (x and y) to express the flow in Orr-Sommerfeld Squire form and then discretise in the wall-normal direction using Chebyshev collocation. Convergence has been checked for all set-ups by doubling the number of grid points; it was shown that the $\mathcal{H}_2$-norm has converged towards a finite value. Finally, we express the Orr-Sommerfeld Squire equations as a state-space model:

$$\dot{\boldsymbol{x}}(t) = \mathbf{A}\boldsymbol{x}(t) + \mathbf{B}_d\boldsymbol{d}(t), \tag{5.5a}$$

$$\boldsymbol{u}(t) = \mathbf{C}\boldsymbol{q}(t), \tag{5.5b}$$

where $\boldsymbol{x} = [\hat{\boldsymbol{w}}, \hat{\boldsymbol{\eta}}]^T$ represents the states of the system (wall-normal velocity and wall-normal vorticity), $\boldsymbol{d} = \left[\hat{\boldsymbol{d}}_x, \hat{\boldsymbol{d}}_y, \hat{\boldsymbol{d}}_z\right]^T$ is a forcing term representing all non-linearities and $\boldsymbol{u} = [\hat{u}, \hat{v}, \hat{w}]$ the velocities. ($\hat{}$) denotes signals in Fourier space. We generate velocity perturbations by randomly forcing the flow. To do so, we treat $\boldsymbol{d}$ as stochastic forces which are white in space and time. We set $\mathbf{B}_d = \mathbf{M}^{-1/2}\mathbf{B}$ to achieve grid-independence, where $\mathbf{M}$ is an integration matrix corresponding to

Clenshaw-Curtis quadrature (Trefethen, 2000). The matrices $\mathbf{A}$, $\mathbf{B}$, and $\mathbf{C}$ are:

$$\mathbf{A} = \begin{bmatrix} \Delta^{-1}\mathcal{L}_{OS} & 0 \\ -\mathrm{i}k_y U' & \mathcal{L}_{SQ} \end{bmatrix}, \tag{5.6a}$$

$$\mathbf{B} = \begin{bmatrix} -\mathrm{i}k_x\Delta^{-1}\mathcal{D} & -\mathrm{i}k_y\Delta^{-1}\mathcal{D} & -k^2\Delta^{-1} \\ \mathrm{i}k_y & -\mathrm{i}k_x & 0 \end{bmatrix}, \tag{5.6b}$$

$$\mathbf{C} = \frac{1}{k^2}\begin{bmatrix} \mathrm{i}k_x\mathcal{D} & -\mathrm{i}k_y \\ \mathrm{i}k_y\mathcal{D} & \mathrm{i}k_x \\ k^2 & 0 \end{bmatrix}, \tag{5.6c}$$

where $\mathcal{L}_{OS}$ and $\mathcal{L}_{SQ}$ are the Orr-Sommerfeld and Squire operators when the viscosity profile ν_T varies along the wall-normal direction (Betchov and Criminale, 1966):

$$\mathcal{L}_{OS} = \mathrm{i}k_x(U'' - U\Delta) + \nu_T\Delta^2 + 2\nu_T'\mathcal{D}\Delta + \nu_T''\left(\mathcal{D}^2 + k^2\right), \tag{5.7a}$$

$$\mathcal{L}_{SQ} = -\mathrm{i}k_x U + \nu_T\Delta + \nu_T'\mathcal{D}, \tag{5.7b}$$

$\mathcal{D} = \frac{\partial}{\partial z}$, $()' = \frac{\partial}{\partial z}()$, $k^2 = k_x^2 + k_y^2$, and $\Delta = \mathcal{D}^2 - k^2$. The boundary conditions are: $\hat{\boldsymbol{w}}_{wall}(t) = \hat{\boldsymbol{w}}'_{wall}(t) = \hat{\boldsymbol{\eta}}_{wall}(t) = 0$.

For the remainder of this chapter, we set $\mathbf{C}$ in equation 5.6c such that the output is the streamwise velocity at all wall-normal locations between $0 \leq z \leq h$.

To quantify the energy of the stochastically-forced linear model, we compute the $\mathcal{H}_2$-norm for one channel half:

$$\|\boldsymbol{u}\|_2 = \mathrm{tr}\left((\mathbf{M}^{1/2}\mathbf{C})^*\mathbf{X}(\mathbf{M}^{1/2}\mathbf{C})\right), \tag{5.8}$$

and at individual wall heights:

$$\|\boldsymbol{u}(z)\|_2 = \mathrm{diag}\left(\mathbf{C}^*\mathbf{X}\mathbf{C}\right), \tag{5.9}$$

where $\mathbf{X}$ is found by solving a Lyapunov equation, $\mathbf{A}\mathbf{X} + \mathbf{X}\mathbf{A}^* = -\mathbf{B}\mathbf{B}^*$ (Jovanović and Bamieh, 2005).

5.3 The optimal estimation problem

In this section, we employ measurements at a single wall-normal location to estimate the streamwise velocity field u at other wall-normal locations. (We consider LM-based and DNS-based measurements.) Specifically, we want to compare the performance between two different set-ups. The first set-up employs off-wall sensors which measure streamwise u_s, spanwise v_s, or wall-normal w_s velocity. Measuring all three velocity components might not be feasible. Thus, we will determine which velocity component and wall-normal location provide the best estimation performance. The second set-up considers at-wall sensors that measure streamwise (τ_x) or spanwise (τ_y) wall shear stress. As before, we determine the measurement quantity that provides the best estimation performance.

This section is in four parts: (i) we introduce the optimal estimation (OE) problem, (ii) we find the best sensor location and measurement type for linear estimation, (iii) we compare the estimation performance for off-wall measurements with that for at-wall measurements in physical space, and (iv) we look at the estimation performance at individual wall heights.

5.3.1 Estimator design[4]

Given a measurement $\boldsymbol{y}$ at a single wall-normal location z_s (which is contaminated by noise $\boldsymbol{n}$) the task in the optimal estimation (OE) problem is to estimate the entire flow field $\boldsymbol{u}$. *Therefore we know the flow at only one location but want to know it everywhere.* The estimate $\boldsymbol{u}_e$ is generated using a linear estimator designed to minimise the estimation error $\boldsymbol{e} = \boldsymbol{u} - \tilde{\boldsymbol{u}}$. The normalised $\mathcal{H}_2$-norm γ_{OE} quantifies the estimation performance. Refer to Appendix C.2 for a description of $\boldsymbol{y}$ and to Oehler and Illingworth (2018a) and Chapter 3 for more information on the design of the estimator.

We generate γ_{OE} for each measurement quantity ($[u_s, v_s, w_s, \tau_x, \tau_y]$), where γ_{OE} is defined as follows:

$$\gamma_{OE} = \sqrt{\frac{\sum_{i\in k_x, j\in k_y} \|\mathbf{e}(i,j)\|_2^2}{\sum_{i\in k_x, j\in k_y} \|\mathbf{u}(i,j)\|_2^2}}. \tag{5.10}$$

[4]This section is similar to §4.3.3.

Therefore, γ_{OE} represents the normalised estimation performance for all wavenumbers considered. Results generated from LM-based measurements are denoted as LM-OE and results generated from DNS-based measurements as DNS-OE.

We are interested in determining the optimal measurement location (z_s) for off-wall measurements. For LM-OE, the iterative gradient minimisation algorithm developed by Chen and Rowley (2011) is used (this was also employed in chapter 3 for the complex Ginzburg-Landau equation). For DNS-OE, we introduce a modified version of the iterative gradient minimisation algorithm, which is applicable to DNS data. The gradient formulation is:

$$\frac{\partial \gamma_{OE}}{\partial z_s} = \frac{\gamma_{OE}(z_s + \delta z_s) - \gamma_{OE}(z_s)}{\delta z_s}, \tag{5.11}$$

where δz_s represents a relatively small perturbation of z_s. The terms $\gamma_{OE}(z_s + \delta z_s)$ and $\gamma_{OE}(z_s)$ are obtained from time responses of the estimator system subject to measurements from DNS.

5.3.2 The best measurement type and location

We want to compare the best off-wall sensor performance to the best at-wall sensor performance. To do so, we have to first find the optimal measurement location z_{s-opt} for the off-wall sensor. The estimation error norm γ_{OE} is shown as a function of sensor location z_s in figure 5.2 for all three measurement types: u_s, v_s and w_s. The discrepancy between the results of DNS-OE and LM-OE is up to 30%. Measuring the streamwise velocity u_s provides the best linear estimates for all sensor locations. The optimal sensor location for LM-OE is $z_{s-opt} = 0.324$, for which $\gamma_{OE} = 0.363$, and for DNS-OE is $z_{s-opt} = 0.324$, for which $\gamma_{OE} = 0.491$.

We now repeat the analysis for wall-based sensing. The best at-wall measurement is provided by measuring τ_x: $\gamma_{OE} = 0.564$ for LM-OE and $\gamma_{OE} = 0.649$ for DNS-OE. These results are 55% (LM) and 24% (DNS) worse than the off-wall measurements. Therefore, measurements of u_s provide the overall best estimation performance.

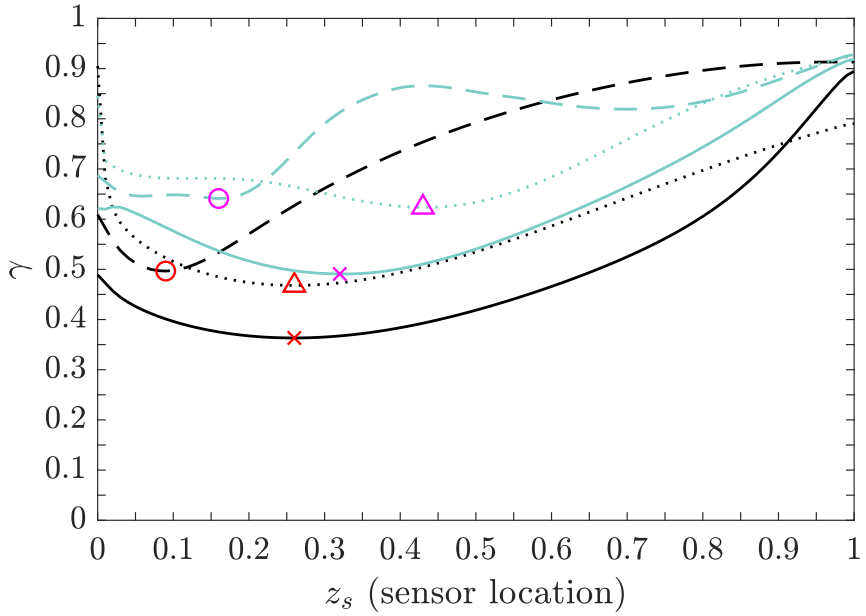

FIGURE 5.2: (a) The estimation error norm γ_{OE} as a function of sensor location z_s for DNS-based measurements of u_s(—), v_s(- - -) and w_s(· · ·) and its prediction as a function of sensor location z_s for LM-based measurements of u_s(—), v_s(- - -) and w_s(· · ·). Optimal locations are indicated (×,◯,△,×,◯,△).

5.3.3 Snapshots from physical space

To get a qualitative understanding of the estimation performance, we now look at physical domain plots of the streamwise velocity perturbations in two-dimensional planes ($z-y$ at $x = 1.5\pi$) at an instant in time ($t = 0.5$). Figure 5.3(a) shows the reference DNS data, figures 5.3(b) and 5.3(c) the estimates obtained for the optimal off-wall and at-wall sensor set-ups and figure 5.3(d) the streamwise velocity as a function of time at a point equidistant to the off-wall and the at-wall placement.

As we might expect, the estimates are best in the vicinity of the measurements. The magnitude of the velocity fluctuations is over-predicted in the proximity of the wall but under-predicted closer to the channel centre.

5.3.4 Estimation performance as a function of wall-height

We are also interested in the estimation performance at individual wall heights to see the dependence of the estimates on the wall-normal location. For that reason, we introduce the root-mean-square (RMS) value $\epsilon(z)$ (Appendix A.4), which is defined

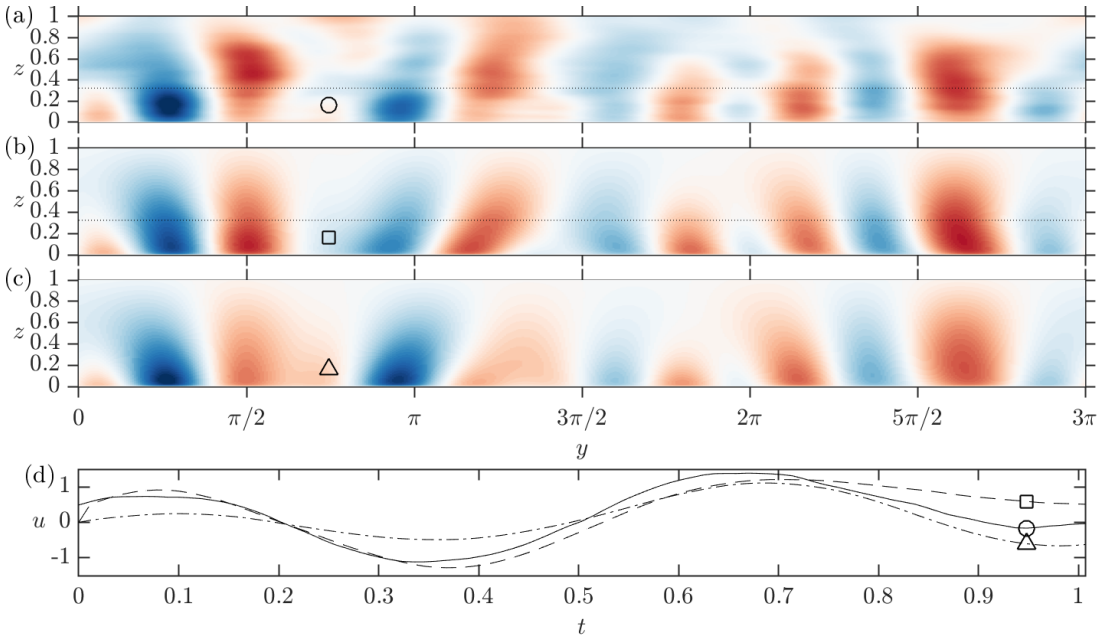

FIGURE 5.3: Streamwise velocity perturbations at $x = 3\pi/2$: (a) for the DNS reference data; (b) the estimate using off-wall measurements at $z_{s-opt} = 0.324(\cdots)$; and (c) the estimate using at-wall measurements. (d) The time history at $y = 3\pi/4$ and $z = 0.16$ ($\bigcirc, \square, \triangle$) for the DNS reference (—), the off-wall measurements ($--$), and the at-wall measurements ($\cdots$). Sixty-five contour levels are shown from $u = -3$ (red) to $u = 3$ (blue).

such that:

$$\gamma^2 = \int_0^h \epsilon^2(z) dz. \tag{5.12}$$

Figure 5.4 shows ϵ_{OE} as a function of the estimation location z for both DNS-OE and LM-OE. (We choose the best off-wall and at-wall measurement.) We see two things. First, ϵ_{OE} is slightly larger for DNS-OE than LM-OE everywhere except in the vicinity of its measurement planes. Nevertheless, there is good agreement between DNS-OE and LM-OE. Second, the RMS for DNS-OE matches with the physical domain plots: the estimation performance is best in the vicinity of the sensor location, and it degrades with distance from it.

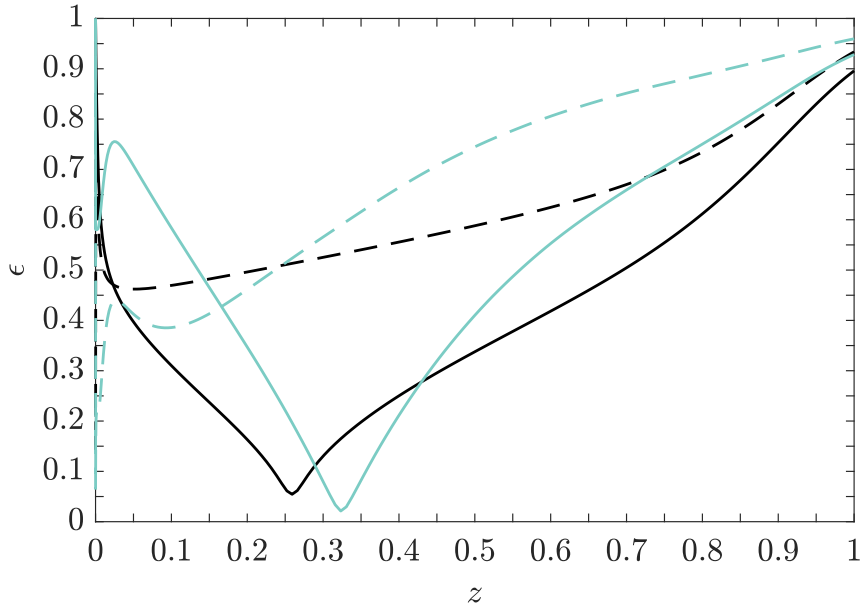

FIGURE 5.4: The estimation error norm ϵ_{OE} as a function of wall height z: for the best off-wall measurement u_s at $z_{s-opt} = 0.324$(—) and at-wall measurement τ_x(- - -) (DNS-OE); for the best off-wall measurement u_s at $z_{s-opt} = 0.259$(—) and at-wall measurement τ_x (- - -) (LM-OE).

5.3.5 Estimation at various Reynolds numbers

So far, we have only considered estimation at $\mathrm{Re}_\tau = 2000$. Now, we look at estimation results for different Re_τ. To do so, we repeat figure 5.2 by showing the estimation error norm γ_{OE} as a function of sensor location z_s for LM-based measurements of u_s at $\mathrm{Re}_\tau \in [500, 1000, 2000, 5000, 10000, 20000]$ in figure 5.5. The optimal sensor location shifts towards the channel centre up to $\mathrm{Re}_\tau = 2000$; and further increases in Reynolds number shift it back towards the wall. At the same time, the estimation performance marginally improves with increasing Reynolds number. Overall, the results are quite insensitive to Reynolds number across the range we have considered.

5.4 The full information control problem

Having looked at sensor selection for OE, it is now interesting to look at actuator selection for full information control (FIC): if we know the entire flow field (i.e.

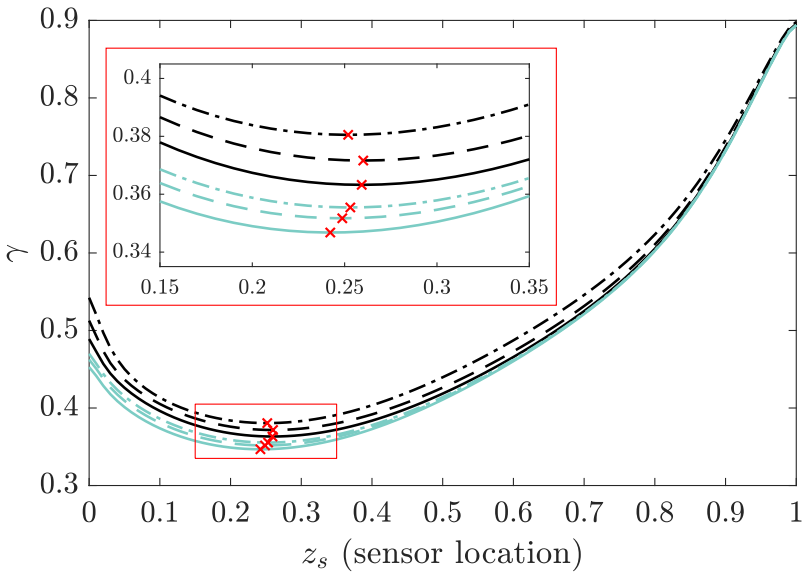

FIGURE 5.5: The norm γ_{OE} as a function of sensor location z_s (employing LM-based streamwise measurements u_s). Results are shown for Re_τ = [500(-·-), 1000(---), 2000(—), 5000(-··-), 10000(-·--), 20000(—)]. The optimal sensor locations z_{s-opt} are indicated (×).

perfect measurements everywhere) but actuate in only one location, what control performance can be achieved? We initially study the FIC problem, because it eliminates the challenges of measurements, and therefore, provides a benchmark for single actuator control. Currently, it is computationally too expensive to run DNS-based control studies for the turbulent channel flow at $Re_\tau = 2000$, which is why we consider LM-based predicted results only.

Similar to the estimation study, we want to compare an off-wall single actuator control set-up with an at-wall set-up. The off-wall actuation we consider is a body force applied in either the streamwise f_x, spanwise f_y or wall-normal f_z direction, and its control performance will depend on its placement location. The wall-based actuation is implemented by applying a Dirichlet boundary condition in the wall-normal direction $\hat{w}_{wall}$, which simulates unsteady blowing and suction with zero net mass flux (Bewley and Liu, 1998).

This section is in three parts: (i) we introduce the full information control (FIC) problem, (ii) we find the best forcing type and location for actuation, and (iii) we compare the control-performance (in physical space) for off-wall actuators to that

for at-wall actuators.

5.4.1 Controller design

Given knowledge of the entire flow field $\boldsymbol{u}_{FI}$, the task in the full information control (FIC) problem is to control the flow field $\boldsymbol{u}_{FI}$ using actuation at a single wall-normal plane z_a ($\boldsymbol{u}_{FI}$ is the flow field subject to FIC). *Therefore we know everything about the flow but can only force it at one location.* The actuation force $\boldsymbol{f}$ is generated by a controller designed to minimise the energy of $\boldsymbol{u}_{FI}$ while also penalising large magnitudes of $\boldsymbol{f}$. The normalised $\mathcal{H}_2$-norm γ_{FI} quantifies the FIC performance. For more information on the controller design, refer to (Oehler and Illingworth, 2018a) and Chapter 3.

We generate γ_{FI} for each forcing direction ($[f_x, f_y, f_z, w_{wall}]$, where γ_{FI} is defined over all wavenumbers considered:

$$\gamma_{FI} = \sqrt{\frac{\sum_{i\in k_x, j\in k_y} \|\boldsymbol{u}_{FI}(i,j)\|_2^2}{\sum_{i\in k_x, j\in k_y} \|\boldsymbol{u}(i,j)\|_2^2}}. \tag{5.13}$$

Refer to Appendix C.2 for the implementation of each forcing type.

As for OE, we utilise the iterative gradient minimisation algorithm of Chen and Rowley (2011) (which was also employed in chapter 3) to optimise the actuator location (z_a) for off-wall actuation in LM-FIC.

5.4.2 The best actuation type and location

We begin by looking for the best off-wall actuation location z_{a-opt}. The control norm γ_{FI} is shown as a function of actuator location z_a in figure 5.6 for all three forcing types (streamwise f_x, spanwise f_y, and wall-normal f_z). Applying a body force in the wall-normal direction f_z provides the best control performance for most actuator locations. The optimal actuator location is $z_{a-opt} = 0.325$, for which $\gamma_{FI} = 0.348$. Forcing f_y near the wall provides marginally better performance than f_z while forcing f_x is always worse than f_z. The at-wall control norm for blowing and suction is: $\gamma_{FI} = 0.387$. Therefore, forcing in the wall-normal direction f_z provides the overall best control performance.

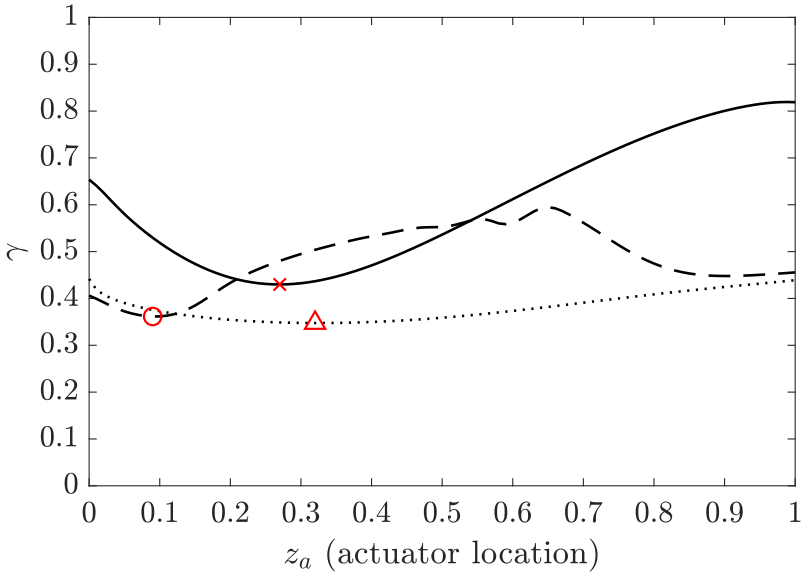

FIGURE 5.6: The energy norm γ_{FI} as a function of actuator location z_a with forcing f_x(—), f_y(- - -) and f_z(· · ·). Optimal locations for each forcing type are also indicated ([×, ◯, △]).

5.4.3 Snapshots from physical space

We now look at spatial domain plots of the streamwise velocity perturbations in two-dimensional planes ($z - y$ at $x = 1.5\pi$) at an instant in time ($t = 0.5$) to get a qualitative look at the control performance. (The results appear noisy due to the constant application of random disturbances everywhere.) Figure 5.7(a) shows the velocity perturbations of the reference LM data, figures 5.7(b) and 5.7(c) the controlled flow fields for off-wall and at-wall FIC. We can see that the off-wall placement performs better than the at-wall placement and that the process of suction and blowing introduces additional velocity perturbations at the wall.

We also consider the streamwise velocity perturbations as a function of time at a point equidistant to the off-wall and at-wall placement in 5.7(d). It shows that the actuators reduce the perturbations significantly at that location for all t.

5.4.4 Control at various Reynolds numbers

Having looked at estimation results for different Re_τ, we now do so for control. For this, we repeat figure 5.6 by showing γ_{FI} as a function of actuator location z_a with

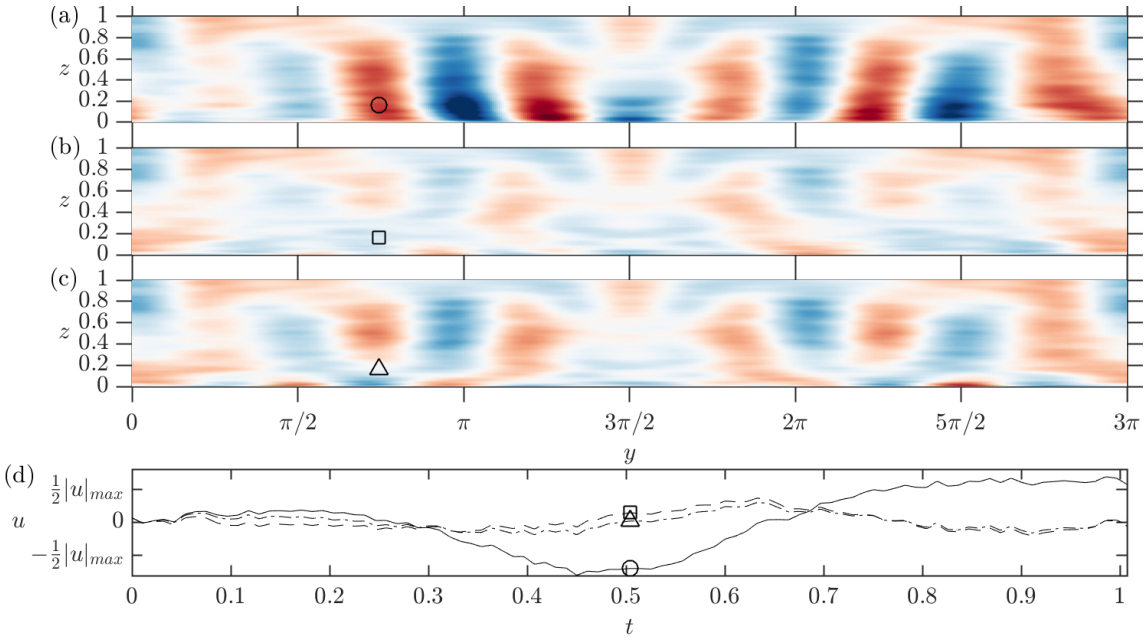

FIGURE 5.7: Streamwise velocity perturbation at $x = 3\pi/2$: (a) uncontrolled reference; (b) off-wall FIC ($z_a = 0.325$); (c) at-wall FIC; and (d) the time history at $y = 3\pi/4$ and $z = 0.16$ for the reference (—), off-wall FIC (−−) and at-wall FIC ($\cdots$). Sixty-five contour levels are shown from $-|u|_{max}$ (red) to $|u|_{max}$ (blue).

wall-normal forcing f_z at $\mathrm{Re}_\tau \in [500, 1000, 2000, 5000, 10000, 20000]$ in figure 5.8. We observe that, just as for estimation in figure 5.5, the optimal actuator location is closest to the channel centre at $\mathrm{Re}_\tau = 2000$ and that control performance marginally improves at higher Re_τ. Overall, the results are quite insensitive to Reynolds number across the range we have considered.

5.5 The input-output control problem

Having looked at sensor selection for estimation and actuator selection for control, we are now interested in the combined input-output control (IOC) problem, where, instead of giving the controller knowledge of the entire flow, time-resolved measurements at only a single wall-normal location are available.

This section is in three parts: (i) we introduce the input-output control (IOC) problem, (ii) we find the best off-wall sensor and actuator location, and (iii) we compare the IOC performance with OE and FIC.

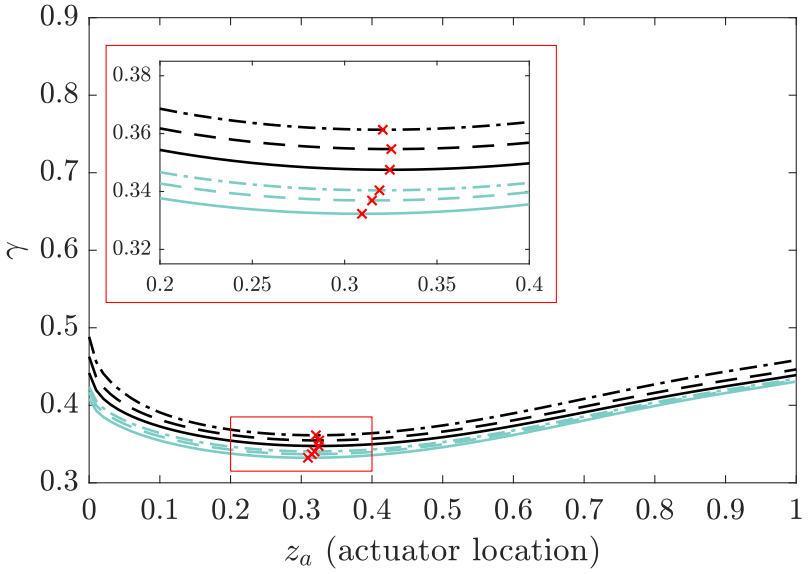

FIGURE 5.8: The norm γ_{FI} as a function of actuator location z_a (employing wall-normal forcing f_z). Results are shown for Re_τ = [500(-·-), 1000(---), 2000(—), 5000(-··-), 10000(-·--), 20000(—)]. The optimal actuator locations z_{a-opt} are indicated (×).

5.5.1 Controller design

Given a measurement $\boldsymbol{y}$ at a single wall-normal location z_s (which is contaminated by noise $\boldsymbol{n}$), the task in the input-output control (IOC) problem is to control the flow field $\boldsymbol{u}_{IO}$ using actuation at a single wall-normal plane z_a. The actuation force $\boldsymbol{f}$ is generated by a controller designed to minimise the energy of $\boldsymbol{u}_{IO}$ while penalising large magnitudes of $\boldsymbol{f}$. *Therefore we know the flow at only one location and can force it at only one location.* The normalised $\mathcal{H}_2$-norm γ_{IO} quantifies the control performance, which is defined in the same way as γ_{FI} (equation 5.13). For more information on the controller design, refer to (Oehler and Illingworth, 2018a) and Chapter 3.

The optimal off-wall placement problem now becomes two dimensional, with both sensor and actuator to be placed simultaneously. We apply a wall-normal body force f_z and measure streamwise velocity u_s because they have provided the best performance in chapters 5.3 and 5.4. As for OE and FIC, we utilise the iterative gradient minimisation algorithm by Chen and Rowley (2011) to optimise z_s and z_a for off-wall measurements in LM-IOC.

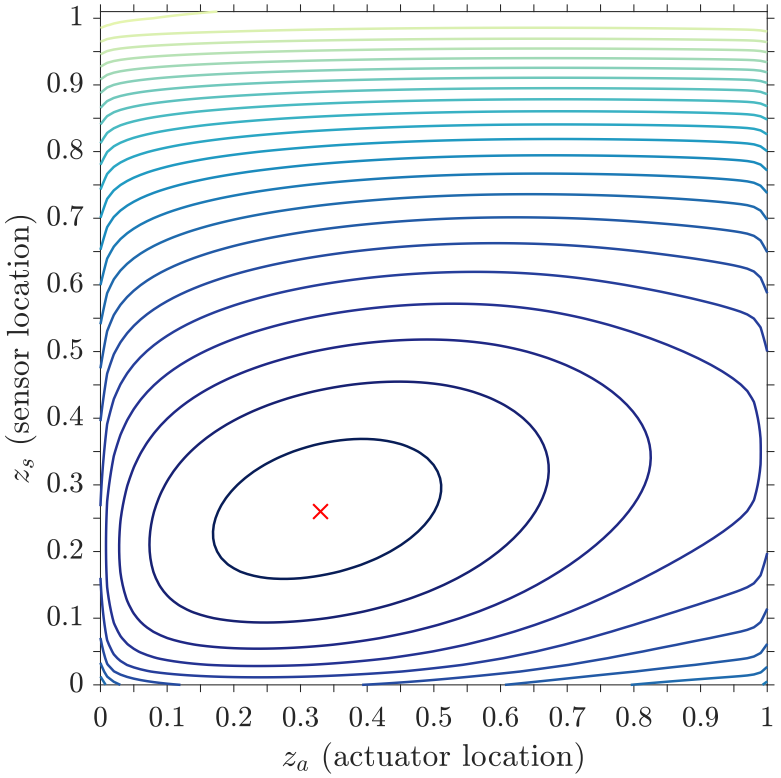

FIGURE 5.9: The energy norm γ_{IO} as a function of sensor z_s and actuator z_a location. The smallest contour is at 0.4 and contours increase in 0.025 steps. The optimal sensor and actuator locations are also indicated (×).

5.5.2 The best single sensor and single actuator set-up

We display the control performance norm γ_{IO} for a range of sensor z_s and actuator z_a locations in figure 5.9. The best performance of $\gamma_{IO} = 0.387$ is achieved at $z_{s-opt} = 0.259$ and $z_{a-opt} = 0.328$. These optimal locations do not coincide with OE and FIC, which is explained in section 3.6.4. For comparison, the best performance for at-wall sensing (τ_x) and at-wall actuating (blowing and suction) is $\gamma_{IO} = 0.620$. Thus measuring and actuating away from the wall gives better performance than measuring and actuating at the wall.

5.5.3 Control performance as a function of wall-height

To compare IOC with FIC and LM-OE, we show the estimation and control performance throughout the channel,ϵ_{IO}, ϵ_{FI}, and ϵ_{OE}, as a function of the estimation

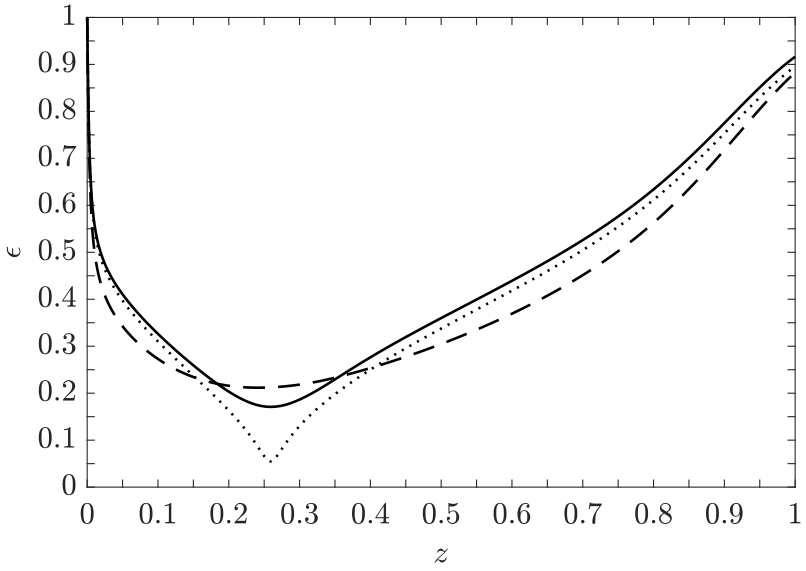

FIGURE 5.10: The energy norms $[\epsilon_{IO}(\text{—}), \epsilon_{FI}(\text{- - -}), \epsilon_{OE}(\cdots)]$ as a function of wall height z for the optimal off-wall placements.

location z in figure 5.10. The norms ϵ_{IO} and ϵ_{FI} quantify the energy of the remaining velocity fluctuations that we could not remove with control, while ϵ_{OE} shows the energy of the velocity fluctuations that we could not estimate (i.e. the estimation error). As a consequence, the interpretation of the three terms is similar. We see that IOC and OE achieve the best perturbation reduction at the sensor location ($z = 0.259$) and FIC achieves the best perturbation reduction at $z = 0.239$.

5.6 Discussion

Table 5.1 provides a summary of the placement results for DNS-OE, LM-OE, FIC and IOC. For all set-ups, the best off-wall placement yields better performance than the best at-wall placement. The differences between the off-wall and at-wall placement performances vary between 10% and 38%. Nevertheless, in an experimental set-up, at-wall sensors and actuators do not interfere with the flow and might be more straightforward to implement. At-wall placements might also be preferable if we are interested in only estimating and controlling structures close to the wall.

Type	Problem	γ (off-wall)	x_{s-opt}	x_{a-opt}	γ (at-wall)	difference
DNS	OE	0.491	0.324		0.649	24.4 %
LM	OE	0.363	0.259		0.564	35.6 %
LM	FIC	0.348		0.325	0.387	10.1 %
LM	IOC	0.387	0.259	0.328	0.620	37.6 %

TABLE 5.1: Summary of the results showing the best performance achieved for estimation and control.

In figure 5.4, the estimation error ϵ_{OE} for DNS degrades more rapidly with distance from the sensor location than its LM-based prediction, which results in a performance difference of 26% for off-wall placements and 13% for at-wall placements. Nevertheless, the linear model can predict the proximity where estimation performs best, and that streamwise velocity measurements provide the best estimates (figure 5.2a). (Presumably, streamwise velocity measurements provide the best estimates because u is the most energetic velocity component.)

The best control performance was achieved by actuating f_z everywhere (except near the wall where f_y provides the best performance). This is consistent with Jovanović and Bamieh (2005) and Hwang and Cossu (2010*b*) who studied the uncontrolled channel flow from an input-output point of view: the forcing components which best amplify the flow are spanwise forcing and wall-normal forcing. It is also consistent with Pujals et al. (2009), who showed that applying forces perpendicular to the streamwise flow direction amplifies velocity streaks more than applying forces parallel to the streamwise flow direction.

The effect of Reynolds number on estimation and control was also considered. It was observed that increasing the Reynolds number marginally improves the estimation and control performance.

5.7 Summary of chapter

Estimation (DNS-OE and LM-OE) and control (FIC and IOC) for a turbulent channel flow at $\mathrm{Re}_\tau = 2000$ was studied. We used a single-plane sensor arrangement for OE; a single-plane actuator arrangement for FIC; and a single-plane sensor and single-plane actuator arrangement for IOC. The estimation and control performance for set-ups in which the sensors and actuators are located inside the flow (off-wall

placement) was compared to set-ups in which the sensors and actuators are located at the wall (at-wall placement). For both estimation and control, the off-wall placements performed better than the at-wall placements (the streamwise velocity measurements and wall-normal body forces were best).

Chapter 6

Linear control of coherent structures in wall-bounded turbulence at $\mathrm{Re}_\tau = 2000$[1]

6.1 Abstract

We consider linear feedback flow control of the largest scales in an incompressible turbulent channel flow at a friction Reynolds number of $Re_\tau = 2000$. A linear model is formed by linearizing the Navier-Stokes equations about the turbulent mean and augmenting it with an eddy viscosity. Velocity perturbations are then generated by stochastically forcing the linear operator. The objective is to reduce the kinetic energy of these velocity perturbations at the largest scales using body forces. It is shown that a control set-up with a well-placed sensor and actuator performs comparably to either measuring the flow everywhere (while actuating it at a single wall height) or actuating the flow everywhere (while measuring it at a single wall height). In this way we gain insight (at low computational cost) into how specific scales of turbulence are most effectively estimated and controlled.

[1]Based on Oehler, S. F., and Illingworth, S. J. (2019), 'Linear control of coherent structures in wall-bounded turbulence at $\mathrm{Re}_\tau = 2000$', *in* 'arXiv preprint arXiv:1906.07462'.

6.2 Introduction

A growing number of studies have successfully utilized linear models for estimation (e.g. Chevalier et al., 2006; Jones et al., 2011; Illingworth et al., 2018; Oehler et al., 2018b; Sasaki et al., 2019) and control (e.g Cortelezzi et al., 1998*a*; Moarref and Jovanović, 2012; Luhar et al., 2014) of wall-bounded turbulent flows. The work of Luhar et al. (2014), in particular, suggests that linear models can qualitatively predict the effect of control on individual scales and also determine at which location they can best be measured. Linear model-based designs are an appealing alternative to direct numerical simulation (DNS) based designs since the cost is several orders of magnitude smaller. One reason for the success of linear models is that linear mechanisms play an important role in the sustenance of turbulence (Schoppa and Hussain, 2002; Kim, 2011). In the linearized Navier-Stokes (LNS) equations, where the flow is linearized around the turbulent mean, these linear mechanisms result in large transient growth that is due to the non-normality of the LNS operator (Trefethen et al., 1993). In particular, del Alamo and Jiménez (2006); Pujals et al. (2009); Hwang and Cossu (2010*b*) showed that the LNS operator could predict the typical widths of near-wall streaks and large-scale structures in the outer layer.

Linear mechanisms play a major role in the formation and maintenance of large-scale structures in turbulent wall-bounded flows. These large-scale structures contribute significantly to the turbulent kinetic energy and Reynolds stresses (in the outer region), and there is evidence that they affect the small scales near the wall (Hutchins and Marusic, 2007*b*; Mathis et al., 2009; Marusic et al., 2010*a*,*b*; Duvvuri and McKeon, 2015). Hence, the control of these structures is crucial for any efforts to control wall-bounded flows (see Kim and Bewley (2007) for a review). It was shown that linear estimation, which is closely related to linear control, performs best for those structures that have the greatest potential for transient growth (del Alamo and Jiménez, 2006; Pujals et al., 2009), are the most amplified in stochastically and harmonically forced settings (Hwang and Cossu, 2010*b*) and are coherent over large wall-normal distances (Madhusudanan et al., 2019). These observations presumably also apply to linear control, which would simplify the controller design process.

This work studies linear feedback control of the largest structures in a turbulent channel flow at a relatively high Reynolds number of $\mathrm{Re}_\tau = 2000$. It is in part motivated by experimental work that has achieved a reduction in skin-friction

drag through real-time control of large-scale structures (Abbassi et al., 2017). The particular focus is on the sensors and actuators needed for control. Specifically, we compare control performance when measuring or actuating the full channel (i.e. an ideal set-up) to control performance when measuring or actuating at only one specific wall height (which is a more realistic set-up in a practical application, e.g. hot-wire sensors and jet actuators). Consequently, it is possible to compare the ideal setting to what is achievable in a laboratory environment. Rather than testing various configurations through the use of DNS, the flow is modeled using the LNS operator for perturbations about the mean flow (§6.3). An eddy viscosity is included in the operator to model the effect of the incoherent scales. We introduce three specific control set-ups in §6.4 and analyze their performance in §6.5. Finally, we conclude the study in §6.6.

6.3 The linear model[2]

A statistically steady incompressible turbulent channel flow at a friction Reynolds number $\mathrm{Re}_\tau = u_\tau h/\nu = 2000$ is considered, where ν is the kinematic viscosity, h the channel half-height, $u_\tau = \sqrt{\tau_w/\rho}$ the friction velocity, τ_w the wall shear stress, and ρ the density. Streamwise, spanwise, and wall-normal spatial coordinates are denoted by $[x, y, z]$ and the corresponding velocities by $[u, v, w]$. We assume zero initial conditions and apply no-slip boundary conditions. Spatial variables are normalized by h, wavenumbers by $1/h$, velocities by the friction velocity u_τ, time by h/u_τ and pressure p by ρu_τ^2. This non-dimensionalization sets the channel half-height to $h = 1$ such that $z \in [0, 2h]$.

Taking the incompressible Navier-Stokes equations we form a linear operator for the perturbations $\boldsymbol{u} = [u, v, w]$ about the turbulent mean flow $\boldsymbol{U} = [U(z), 0, 0]$, where the non-linear term $\boldsymbol{d} = -(\boldsymbol{u}\cdot\nabla)\boldsymbol{u} + \overline{(\boldsymbol{u}\cdot\nabla)\boldsymbol{u}}$ is treated as stochastic forcing, $\bar{(\cdot)}$ represents the time-averaged mean and an eddy viscosity $\nu_T(z)$ is introduced to model the effect of incoherent motions (Reynolds and Hussain, 1972; del Alamo and

[2]This section is similar to §5.2.1.

Jiménez, 2006; Pujals et al., 2009):

$$\frac{\partial \boldsymbol{u}}{\partial t} = -\left(\boldsymbol{U}\cdot\nabla\right)\boldsymbol{u} - \left(\boldsymbol{u}\cdot\nabla\right)\boldsymbol{U} - \nabla p + \nabla\cdot\left[\frac{\nu_T}{\nu}(\nabla\boldsymbol{u}+\nabla\boldsymbol{u}^T)\right] + \boldsymbol{d}, \qquad \nabla\cdot\boldsymbol{u} = 0. \tag{6.1}$$

An analytical fit is used (Cess, 1958) for the eddy viscosity profile ν_T as in several previous studies (Pujals et al., 2009; del Alamo and Jiménez, 2006; Moarref and Jovanović, 2012; Illingworth et al., 2018):

$$\nu_T(z) = \frac{\nu}{2}\left\{1 + \frac{\kappa_1^2\mathrm{Re}_\tau^2}{9}(2z-z^2)^2(3-4z+2z^2)^2 \times \left[1-\exp\left(\frac{-\mathrm{Re}_\tau z}{\kappa_2}\right)\right]^2\right\}^{1/2} + \frac{\nu}{2}. \tag{6.2}$$

Integrating $\mathrm{Re}_\tau(1-z)\nu/\nu_T(z)$ provides the mean velocity profile $U(z)$. The constants $\kappa_1 = 0.426$ and $\kappa_2 = 25.4$ give the best fit to the mean velocity profile of a DNS simulation at $\mathrm{Re}_\tau = 2003$ (Hoyas and Jiménez, 2006; del Alamo and Jiménez, 2006). Controlling perturbations in the flow will alter the mean velocity profile and with it the linear model itself (which is formed about the mean). The controller, therefore, needs to be robust to account for any changes in the mean flow. It would be interesting to study robustness, but this is beyond the scope of this study.

We need to express the flow in state-space form to access standard tools from dynamics and control. To do so, we first take Fourier transforms in the homogeneous streamwise and spanwise directions to express the flow in the Orr-Sommerfeld Squire form and then discretize in the wall-normal direction using Chebyshev collocation of order 200. Convergence has been checked for all set-ups by doubling the number of grid points; it was shown that the $\mathcal{H}_2$-norm has converged towards a finite value. Finally, we express the Orr-Sommerfeld Squire equations as a linear state-space model:

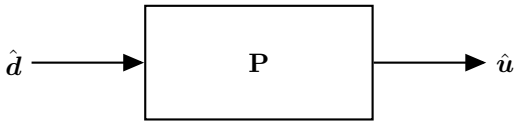

$$\dot{\hat{\boldsymbol{q}}}(t) = \mathbf{A}\hat{\boldsymbol{q}}(t) + \mathbf{B}_d\hat{\boldsymbol{d}}(t), \tag{6.3a}$$

$$\hat{\boldsymbol{u}}(t) = \mathbf{C}\hat{\boldsymbol{q}}(t), \tag{6.3b}$$

where $\hat{\boldsymbol{q}} = [\hat{\boldsymbol{w}}, \hat{\boldsymbol{\eta}}]^T$ represents the states of the system (wall-normal velocity and wall-normal vorticity), $\hat{\boldsymbol{d}} = \left[\hat{d}_x, \hat{d}_y, \hat{d}_z\right]^T$ all non-linearities and $\hat{\boldsymbol{u}} = [\hat{u}, \hat{v}, \hat{w}]$ the velocities ($\hat{}$) denotes signals in Fourier space). We treat $\hat{\boldsymbol{d}}$ as stochastic forcing that is white in space and time (Jovanović and Bamieh, 2005). Therefore, we account for the non-linearities by treating them as a source of intrinsic forcing to the LNS operator (McKeon and Sharma, 2010). We set $\mathbf{B}_d = \mathbf{M}^{-1/2}\mathbf{B}$ to achieve grid-independence, where $\mathbf{M}$ is an integration matrix corresponding to Clenshaw-Curtis quadrature (Trefethen, 2000), and we choose $\mathbf{C}$ in equation (6.3b) such that $\hat{\boldsymbol{u}}$ corresponds to the velocity field over one channel-half ($0 \leq z \leq h$). The matrices $\mathbf{A}$, $\mathbf{B}$, and $\mathbf{C}$ are:

$$\mathbf{A} = \begin{bmatrix} \Delta^{-1}\mathcal{L}_{OS} & 0 \\ -\mathrm{i}k_y U' & \mathcal{L}_{SQ} \end{bmatrix}, \tag{6.4}$$

$$\mathbf{B} = \begin{bmatrix} -\mathrm{i}k_x\Delta^{-1}\mathcal{D} & -\mathrm{i}k_y\Delta^{-1}\mathcal{D} & -k^2\Delta^{-1} \\ \mathrm{i}k_y & -\mathrm{i}k_x & 0 \end{bmatrix}, \tag{6.5}$$

$$\mathbf{C} = \frac{1}{k^2}\begin{bmatrix} \mathrm{i}k_x\mathcal{D} & -\mathrm{i}k_y \\ \mathrm{i}k_y\mathcal{D} & \mathrm{i}k_x \\ k^2 & 0 \end{bmatrix}, \tag{6.6}$$

where $\mathcal{L}_{OS}$ and $\mathcal{L}_{SQ}$ are the Orr-Sommerfeld and Squire operators for the eddy viscosity enhanced LNS equations (Betchov and Criminale, 1966):

$$\mathcal{L}_{OS} = \mathrm{i}k_x(U'' - U\Delta) + \nu_T\Delta^2 + 2\nu_T'\mathcal{D}\Delta + \nu_T''\left(\mathcal{D}^2 + k^2\right), \tag{6.7}$$

$$\mathcal{L}_{SQ} = -\mathrm{i}k_x U + \nu_T\Delta + \nu_T'\mathcal{D}. \tag{6.8}$$

Here $\mathcal{D} = \frac{\partial}{\partial z}$, $()' = \frac{\partial}{\partial z}()$, $k^2 = k_x^2 + k_y^2$, and $\Delta = \mathcal{D}^2 - k^2$. The boundary conditions are: $\hat{\boldsymbol{w}}_{wall}(t) = \hat{\boldsymbol{w}}'_{wall}(t) = \hat{\boldsymbol{\eta}}_{wall}(t) = 0$. (See Appendix D.1 for more information.) By taking Laplace transforms of equation (6.3) we obtain a transfer function $\mathbf{P}$ that relates the input $\hat{\boldsymbol{d}}$ to the output $\hat{\boldsymbol{u}}$:

$$\hat{\boldsymbol{u}}(s) = \mathbf{P}(s)\hat{\boldsymbol{d}}(s), \tag{6.9a}$$

$$\mathbf{P}(s) = \mathbf{C}\left(s\mathbf{I} - \mathbf{A}\right)^{-1}\mathbf{B}_d, \tag{6.9b}$$

where s is the Laplace variable. By setting $s = \mathrm{j}\omega$ the frequency response (i.e. the resolvent) is obtained.

We are interested in the energy of the flow, which we quantify using the $\mathcal{H}_2$-norm (Appendix D.3):

$$\|\hat{\boldsymbol{u}}\|_2 \equiv \sqrt{\frac{1}{2\pi}\int_{-\infty}^{\infty} \mathrm{trace}\left[\mathbf{P}^*(\mathrm{j}\omega)\mathbf{M}\mathbf{P}(\mathrm{j}\omega)\right] d\omega} \tag{6.10}$$

$$\equiv \left[\mathbb{E}\left\{\lim_{T\to\infty}\frac{1}{T}\int_0^T\left(\int_0^h \hat{\boldsymbol{u}}^*(z,t)\hat{\boldsymbol{u}}(z,t)dz\right)dt\right\}\right]^{1/2}, \tag{6.11}$$

where $\mathbb{E}$ is the expected value and $()^*$ is the complex conjugate transpose. In the Laplace domain, the $\mathcal{H}_2$-norm of $\mathbf{P}(s = \mathrm{j}\omega)$ can be seen as the average gain between the input $\hat{\boldsymbol{d}}(s = \mathrm{j}\omega)$ and the output $\hat{\boldsymbol{u}}(s = \mathrm{j}\omega)$ over all frequencies and all directions.

Figure 6.1 shows $\|\hat{\boldsymbol{u}}\|_2$ for a range of k_x and k_y. We see that $\|\hat{\boldsymbol{u}}\|_2$ is largest at $k_x = 0$ and $k_y = 4/3$. (See Hwang and Cossu (2010*b*,*a*) for a detailed analysis on the energy amplification of the laminar channel flow.) In §6.5.2–§6.5.4, we choose to study the streamwise and spanwise wavenumber pairs that are most amplified (we select them to be $|k_x| \leq 0.5$ and $|k_y| \leq 6$, which is marked in figure 6.1).

6.4 The control set-up[3]

So far, we have introduced the eddy-viscosity-enhanced Orr-Sommerfeld and Squire operators that are linearized about the mean velocity profile of a turbulent channel flow. We stochastically force the linear operator to generate velocity perturbations that we now want to control. To do so, we include three new signals ($\hat{\boldsymbol{m}}$, $\hat{\boldsymbol{f}}$ and $\hat{\boldsymbol{z}}$) into the state-space model (equation 6.3):

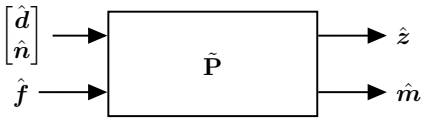

$$\dot{\hat{\boldsymbol{q}}}(t) = \mathbf{A}\hat{\boldsymbol{q}}(t) + \mathbf{B}_d\hat{\boldsymbol{d}}(t) + \mathbf{B}_f\hat{\boldsymbol{f}}(t), \tag{6.12a}$$

$$\hat{\boldsymbol{z}}(t) = \mathbf{C}_z\hat{\boldsymbol{q}}(t) + \alpha\hat{\boldsymbol{f}}(t), \tag{6.12b}$$

$$\hat{\boldsymbol{m}}(t) = \mathbf{C}_m\hat{\boldsymbol{q}}(t) + \hat{\boldsymbol{n}}(t). \tag{6.12c}$$

The first new signal $\hat{\boldsymbol{m}}$ represents a time-resolved velocity measurement at a single wall height ($\mathbf{C}_m\hat{\boldsymbol{q}}$) that is contaminated by sensor noise ($\hat{\boldsymbol{n}}$). We treat $\hat{\boldsymbol{n}}$ as an unknown forcing that is white in time with a covariance $\mathbb{E}(\hat{\boldsymbol{n}}\hat{\boldsymbol{n}}^*)$ of 10^{-4}. The second

[3]This section is similar to §3.4, §5.3.1, §5.4.1 and §5.5.1.

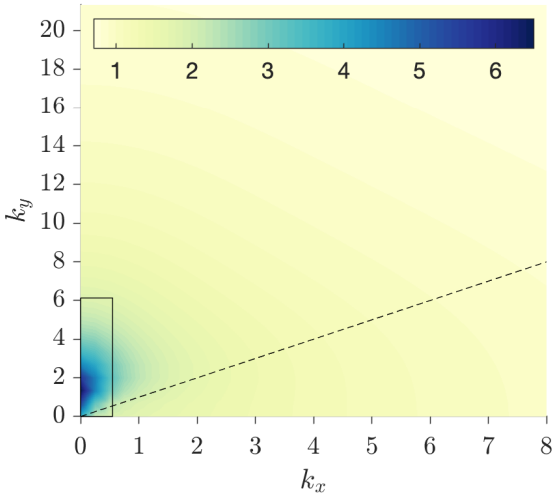

FIGURE 6.1: The energy norm of the uncontrolled flow $\|\hat{\boldsymbol{u}}\|_2$ as a function of streamwise k_x and spanwise k_y wavenumber represented by fifty-nine contour levels from 0.7 (yellow) to 6.5 (blue). Also denoted on the figure are the wavenumber pairs where $k_x = k_y(--)$ and the range of wavenumbers we consider in figures 6.4, 6.5, 6.6 and 6.7(□).

new signal $\hat{\boldsymbol{f}}$ represents a time-resolved body force at a single wall height to actuate the flow ($\mathbf{B}_f\hat{\boldsymbol{f}}$). Both $\hat{\boldsymbol{m}}$ and $\hat{\boldsymbol{f}}$ are defined in Appendix D.2. The third new signal $\hat{\boldsymbol{z}}$ (not to be confused with wall-normal variable z) represents the quantity to be minimized by control. We define $\hat{\boldsymbol{z}}$ to minimize the energy of the entire flow field ($\boldsymbol{C}_z\hat{\boldsymbol{q}}$) while also keeping the actuation force small ($\alpha\hat{\boldsymbol{f}}$, where α is a penalization on large $\hat{\boldsymbol{f}}$). We set the penalization to be insignificant ($\alpha = 10^{-4}$) because we want to achieve the best possible control performance. (Increasing α will gradually reduce the control performance and energy consumption of the actuator.) Minimizing the energy of the entire flow-field lets the control design process decide which perturbations to target for the best results. This is in contrast to opposition control, for example, which focuses on wall-normal velocity perturbations to eliminate streamwise streaks (Luhar et al., 2014). (See Appendix D.3 for a derivation of the cost signal.)

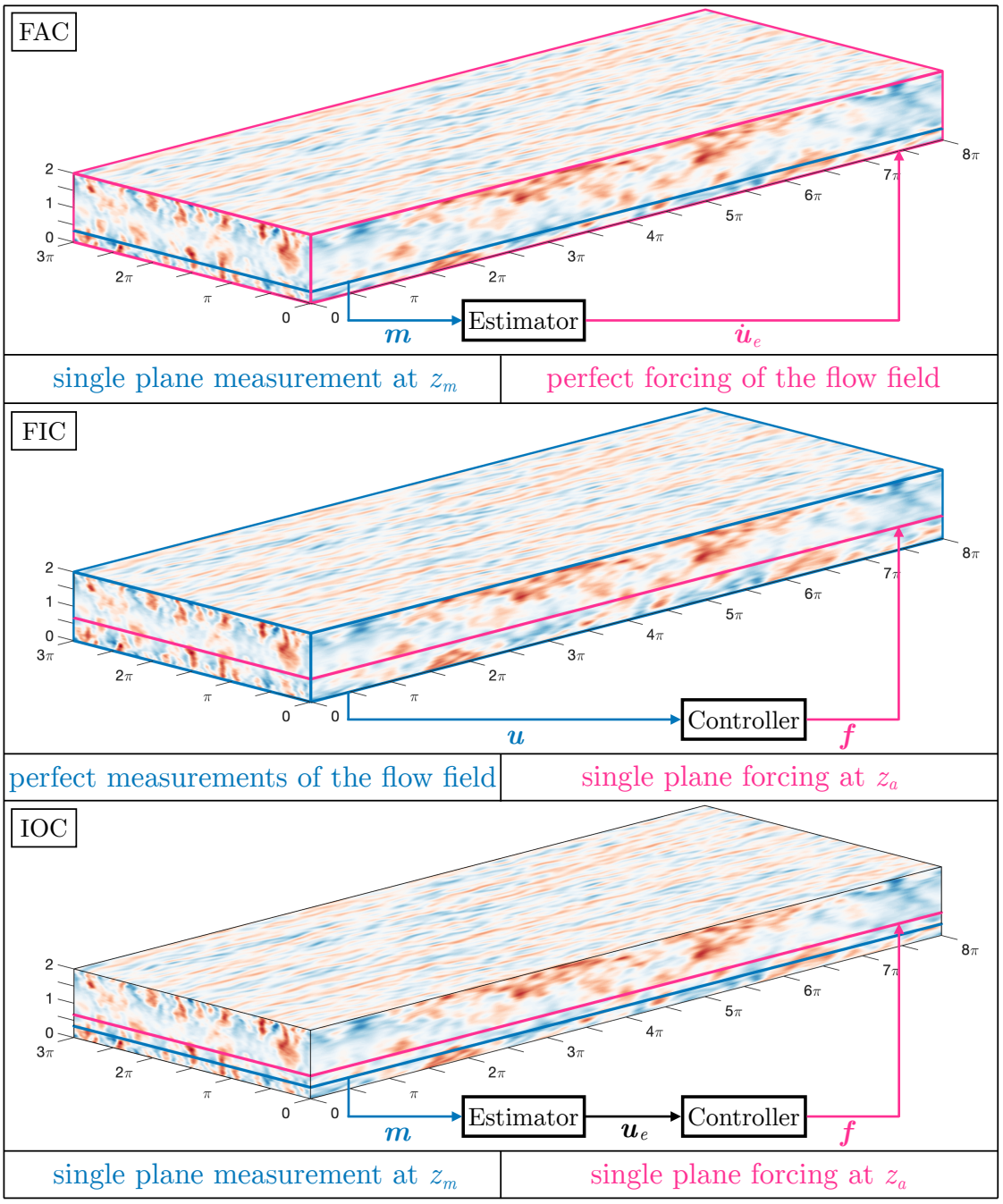

FIGURE 6.2: The FAC, FIC, and IOC problems.

6.4.1 The three control problems

We now want to use the system $\tilde{\mathbf{P}}$, defined in Equation (6.12), to investigate three different control problems of interest. The first of these is full actuation control (FAC), where the controller can actuate the flow everywhere but is limited to measurements at one wall height. The second is full information control (FIC), where the flow is measured everywhere, but now actuation is limited to one wall height. The third is input-output (IOC) control, where sensors and actuators are limited to one wall height. This final configuration is of particular interest since it is the most feasible experimental configuration. A fourth case, where there are no limitations on which sensors or actuators are available, is not considered since it can instantly set the flow to the desired state. The three configurations are illustrated in figure 6.2, and the details of their state-space models can be found in Appendix D.3. We study FAC, FIC and IOC because we want to know what price we have to pay when only a single actuator is available (as opposed to actuating the flow everywhere); and what price we have to pay when only a single sensor is available (as opposed to knowledge of the flow everywhere). This, in turn, provides insight on the extent to which control of the largest scales is fundamentally difficult; and on the extent to which control is limited by having only a single sensor or a single actuator.

6.4.1.1 Full actuation control

In the full actuation control (FAC) problem, we can actuate the flow everywhere but only have access to sensor measurements $\hat{\boldsymbol{m}}$ at a single location z_s[4]. These measurements are contaminated by sensor noise $\hat{\boldsymbol{n}}$. The task in the FAC problem is to estimate the entire state $\hat{\boldsymbol{q}}$, and then use the estimate $\hat{\boldsymbol{q}}_e$ to control the flow. *Thus we only have one sensor to measure the flow, and we want to use it to control the flow everywhere.*

The state estimate is generated using an estimator:

$$\dot{\hat{\boldsymbol{q}}}_e(t) = (\mathbf{A} - \mathbf{L}\mathbf{C}_m)\,\hat{\boldsymbol{q}}_e(t) + \mathbf{L}\hat{\boldsymbol{m}}(t), \tag{6.13a}$$

$$\hat{\boldsymbol{u}}_e(t) = \mathbf{C}\hat{\boldsymbol{q}}_e(t), \tag{6.13b}$$

[4]It could also be multiple sensors at various locations, multiple actuators at various locations, or both.

where $\mathbf{L}$ is the estimator gain value (designed in Appendix D.3). The estimator knows the dynamics of the system (represented by $\mathbf{A}\hat{\boldsymbol{q}}_e$), but it neither knows the initial conditions nor the stochastic disturbances $\hat{\boldsymbol{d}}$ that are applied to the linear operator. It corrects itself using the error between the measurement and its estimate: $\mathbf{L}(\hat{\boldsymbol{m}} - \mathbf{C}_m\hat{\boldsymbol{q}}_e)$. The estimate of the velocity field is applied as a body force to the entire flow, which immediately eliminates estimated perturbations from the flow, and therefore, acts as a perfect actuation set-up.

6.4.1.2 Full information control

In the full information control (FIC) problem, we have an actuator $\mathbf{B}_f\hat{\boldsymbol{f}}$ at a single location z_a[4], and we are given knowledge of the entire system state $\hat{\boldsymbol{q}}$. *Thus we know everything about the flow, but we only have one actuator to control the flow.* A controller generates the actuator force $\hat{\boldsymbol{f}}$:

$$\hat{\boldsymbol{f}}(t) = -\mathbf{K}\hat{\boldsymbol{q}}(t), \tag{6.14}$$

where $\mathbf{K}$ is the controller gain value (designed in Appendix D.3). The 'measurement' for this arrangement is the full flow field $\hat{\boldsymbol{q}}$, because it is assumed that the controller 'knows everything'.

6.4.1.3 Input-output control

In the input-output control (IOC) problem, we only have one measurement $\hat{\boldsymbol{m}}$ at z_s available to estimate the flow, and we only have one actuator $\mathbf{B}_f\hat{\boldsymbol{f}}$ at z_a available to control the flow[4]. The measurement $\hat{\boldsymbol{m}}$, which is contaminated by sensor noise $\hat{\boldsymbol{n}}$, is used to obtain an estimate $\hat{\boldsymbol{q}}_e$ (from an estimator), and the actuator force $\hat{\boldsymbol{f}}$ is generated with a controller that uses $\hat{\boldsymbol{q}}_e$. *(Thus we only have one sensor to estimate the flow, and we only have one actuator available to control the flow.)* To form a combined estimator and controller, we rewrite equation (6.14) to include $\hat{\boldsymbol{q}}_e$:

$$\dot{\hat{\boldsymbol{q}}}_e(t) = \left(\mathbf{A} - \mathbf{L}\mathbf{C}_m - \mathbf{B}_f\mathbf{K}\right)\hat{\boldsymbol{q}}_e(t) + \mathbf{L}\hat{\boldsymbol{m}}(t), \tag{6.15a}$$

$$\hat{\boldsymbol{f}}(t) = -\mathbf{K}\hat{\boldsymbol{q}}_e(t). \tag{6.15b}$$

6.4.2 Control performance

We quantify the magnitude of $\hat{\boldsymbol{z}}(s)$ with the $\mathcal{H}_2$-norm for a channel half $\|\hat{\boldsymbol{z}}\|_2$ similar to equation 6.11 (Appendix D.3). From this, we define the control performance parameter $\hat{\gamma}$:

$$\hat{\gamma} = \sqrt{\frac{\|\hat{\boldsymbol{z}}\|_2^2}{\|\hat{\boldsymbol{u}}_{ref}\|_2^2}} = \sqrt{\frac{\|\hat{\boldsymbol{u}}_{ctrl}\|_2^2 + \alpha\|\hat{\boldsymbol{f}}\|_2^2}{\|\hat{\boldsymbol{u}}_{ref}\|_2^2}}, \tag{6.16}$$

where $\|\hat{\boldsymbol{u}}_{ref}\|_2$ is the $\mathcal{H}_2$-norm of the uncontrolled reference flow, $\|\hat{\boldsymbol{u}}_{ctrl}\|_2$ the $\mathcal{H}_2$-norm of the controlled flow, and $\|\hat{\boldsymbol{f}}\|_2$ the $\mathcal{H}_2$-norm of the energy consumed by the actuator. The control performance parameter is defined such that $0 \leq \hat{\gamma} \leq 1$, where 0 indicates the best case scenario in which the controller eliminates all velocity perturbations, and 1 indicates the worst case scenario in which the controller achieves no reduction in the energy of the flow.

6.4.3 Optimal sensor and actuator placement

We want to place the sensors and actuators at the wall height that provides the best performance. To do so, we conduct an iterative minimization search across all possible sensor and actuator locations (z_s and z_a) to find the lowest $\hat{\gamma}$ possible. The iterative gradient minimization employed has been introduced and discussed in earlier studies (Chen and Rowley, 2011; Oehler and Illingworth, 2018a). By following the approach of Oehler and Illingworth (2018c) in chapter 5, it was determined that the optimal collocated placement for the sensor and actuator is at $z_a = z_s = 0.32$. (Note that only wavenumbers satisfying $|k_x| \leq 0.5$ and $|k_y| \leq 6$ are considered while computing these optimal placement locations). We choose to collocate the sensor and actuator to simplify the problem (collocation marginally affects the performance).

6.5 Control performance

This section is in four parts: §6.5.1 examines the control performance at individual wavenumber pairs; §6.5.2 looks at the overall performance; §6.5.3 at the performance across individual wall heights; and §6.5.4 considers the energy consumed by actuation.

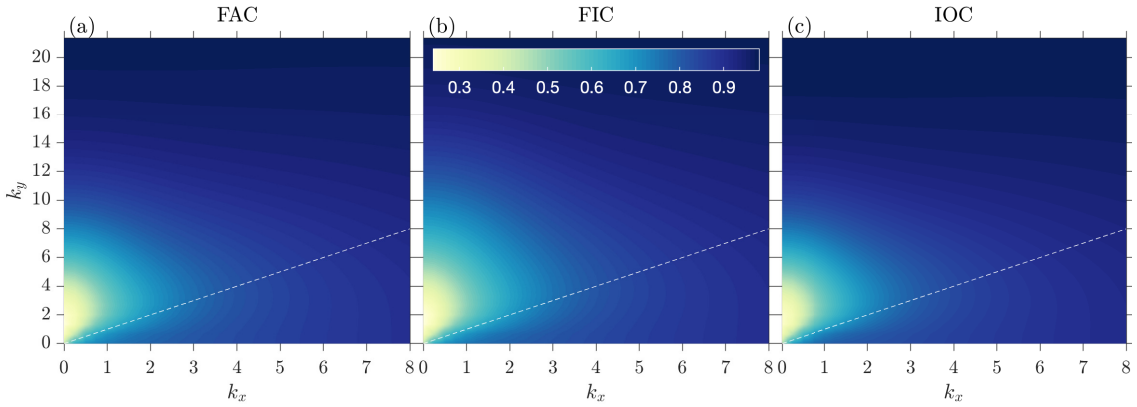

FIGURE 6.3: The energy norms $\hat{\gamma}_{FA}$(a), $\hat{\gamma}_{FI}$(b) and $\hat{\gamma}_{IO}$(c) as a function of streamwise k_x and spanwise k_y wavenumber represented by seventy-five contour levels from from 0.24 (yellow) to 0.98 (blue). Also denoted on the figure are the wavenumber pairs where $k_x = k_y(--)$.

6.5.1 Control at individual wavenumber pairs

In this section, we study the control performance of FAC, FIC and IOC over a range of wavenumber pairs (k_x,k_y). For this purpose, we use the parameter $\hat{\gamma}$, as defined in equation (6.16). In figure 6.3, $\hat{\gamma}$ is plotted as a function of k_x and k_y (the channel length is $x = 8\pi$ and width is $y = 3\pi$; the streamwise resolution is $\Delta k_x = 1/4$ and the spanwise resolution is $\Delta k_y = 2/3$). The contours of $\hat{\gamma}$ are almost identical for the three problems. Therefore, from figure 6.3, we see that the performance of the control scenario where we have one optimally placed sensor and actuator (IOC) is comparable to the cases where we actuate everywhere (FAC) or know everything (FIC). Hence, we observe that actuating everything does not significantly increase the control performance when we are limited to one sensor. Similarly, measuring everything does not significantly increase the control performance when we are limited to one actuator. We observe that, for all three problems, $\hat{\gamma}$ is the lowest for streamwise-constant structures ($k_x = 0$) with a spanwise wavenumber of $k_y = 4/3$. As the structures become smaller (k_x and k_y increase), $\hat{\gamma}$ increases. This behavior can partly be explained by the smaller scales being less coherent across wall-normal distances (Madhusudanan et al., 2019). As a consequence, single sensor and actuator control at the smaller scales might not be feasible, even if we consider second-order statistics (Zare et al., 2017) or non-linear controller designs (Lauga and

Bewley, 2004).

It is important to assess whether the controllers perform well for the most energetic scales. For this, we compare figure 6.3, which shows the normalized $\mathcal{H}_2$-norm for the controlled flow, with figure 6.1, which shows the $\mathcal{H}_2$-norm of the uncontrolled flow. We observe that, in all three cases, the performance of the controller is the best (low $\hat{\gamma}$) for the wavenumber pairs (k_x,k_y) that are most amplified (high $\|\hat{\boldsymbol{u}}\|_2$). This result is important because it shows that we can reduce the energy of the largest, most amplified scales with a limited number of sensors and actuators. The same relationship has been observed in the estimation literature (Illingworth et al., 2018; Oehler et al., 2018b; Madhusudanan et al., 2019): linear estimation performs best for the wavenumber pairs (k_x,k_y) that are most amplified (high $\|\hat{\boldsymbol{u}}\|_2$). Therefore, the scales that we can estimate well are also those we can control well.

6.5.2 Control in physical space

We now look at control for a set of large-scale structures: $|k_x| \leq 0.5$ and $|k_y| \leq 6$, the range of which is indicated in figure 6.1. The figure shows that these structures are the most amplified in the stochastically forced LNS model, and we can see in figure 6.3 that they are also the best for control.

We begin by looking at snapshots of the velocity perturbations in two-dimensional planes ($z-y$ at $x = 1.5\pi$) at an instance in time ($t = 0.5$, i.e. after half a channel flow-through). The data is generated from the linear model. Figure 6.4a shows the flow field of the uncontrolled (reference) flow. Figures 6.4b–6.4d show the controlled flow fields for each of the three cases FAC, FIC and IOC, respectively. We observe that all three controllers achieve a significant reduction of the streamwise velocity perturbations everywhere. The spanwise and wall-normal velocity components are also reduced, most notably at $z_s = z_a = 0.32$ (corresponding to the location of the sensor and actuator).

It is difficult to quantify and compare the control performances from a snapshot in time. For that reason, we sum the $\mathcal{H}_2$-norm across all the wavenumber pairs (k_x, k_y) considered. The parameter γ is the ratio of these summed $\mathcal{H}_2$-norms computed from

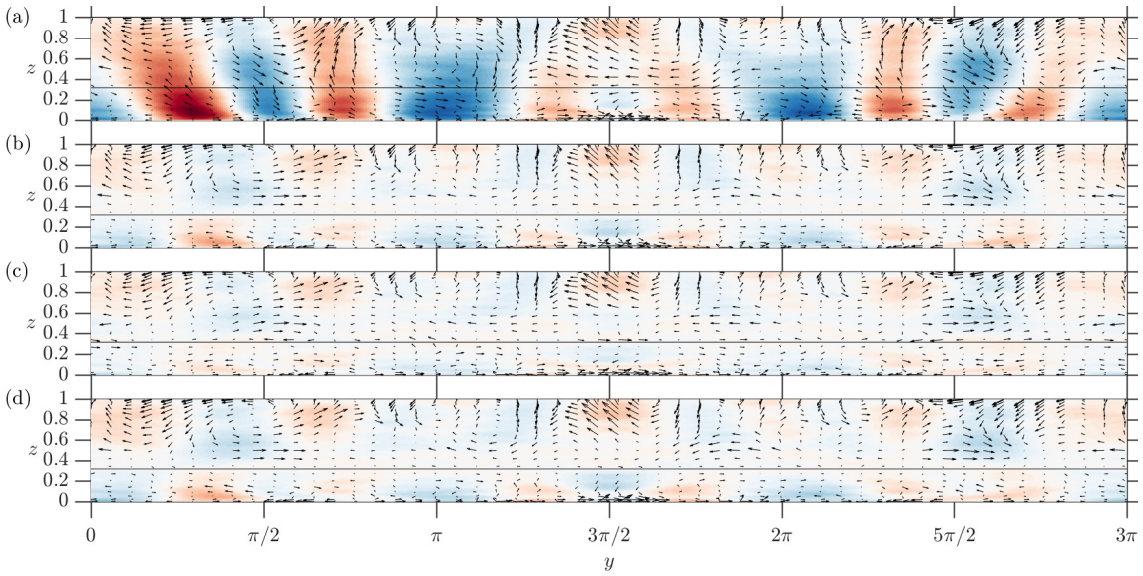

FIGURE 6.4: Velocity perturbations (streamwise: contour; spanwise and wall-normal: vector plot) at $x = 3\pi/2$: (a) uncontrolled reference, (b) FAC, (c) FIC, and (d) IOC. The sensor and actuator are placed at $z_s = z_a = 0.32$. Sixty-five contour levels are shown from $-|u|_{max}$ (blue) to $|u|_{max}$ (red).

γ_{FA}	γ_{FI}	γ_{IO}
0.387	0.368	0.404

TABLE 6.1: The control performance for FAC, FIC and IOC.

the controlled and the uncontrolled cases, respectively:

$$\gamma = \sqrt{\frac{\sum_{i\in k_x, j\in k_y} \|\hat{\boldsymbol{z}}(i,j)\|_2^2}{\sum_{i\in k_x, j\in k_y} \|\hat{\boldsymbol{u}}_{ref}(i,j)\|_2^2}}. \tag{6.17}$$

As a consequence, γ represents the normalised performance of the controller integrated across all three velocity components u, v and w. The values of γ are shown in table 6.1, and they tell us that the overall performance is similar, although FIC slightly outperforms FAC and IOC.

To further understand the control results, it is important to look at the impact of the controllers on each velocity component $[u, v, w]$ separately. Thus, we look at the kinetic energy (i.e. the squared $\mathcal{H}_2$-norm) of each velocity component relative to

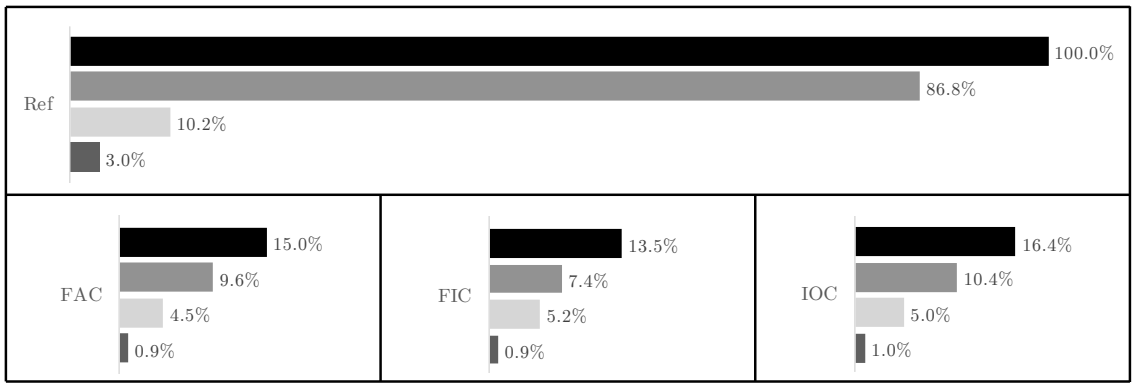

FIGURE 6.5: The reduction of the kinetic energy relative to the entire flow: $\mathbf{E}_{u,v,w}$ (■), $\mathbf{E}_u$(■), $\mathbf{E}_v$(■) and $\mathbf{E}_w$(■), where $\mathbf{E}_{u,v,w} = \mathbf{E}_u + \mathbf{E}_v + \mathbf{E}_w$.

the energy of the entire uncontrolled flow-field:

$$\mathbf{E} = \frac{\sum_{i\in k_x, j\in k_y} \|\hat{\boldsymbol{y}}(i,j)\|_2^2}{\sum_{i\in k_x, j\in k_y} \|\hat{\boldsymbol{u}}_{ref}(i,j)\|_2^2}. \tag{6.18}$$

By setting $\hat{\boldsymbol{y}}$ to be different velocity components, $\mathbf{E}$ is defined in four different ways: (i) $\mathbf{E}_{u,v,w}$, where $\hat{\boldsymbol{y}}$ represents all the three velocity components, (ii) $\mathbf{E}_u$ where $\hat{\boldsymbol{y}}$ represents the streamwise velocity component, (iii) $\mathbf{E}_v$, where $\hat{\boldsymbol{y}}$ represents the spanwise velocity component, and (iv) $\mathbf{E}_w$, where $\hat{\boldsymbol{y}}$ represents the wall-normal velocity component. Figure 6.5 shows $\mathbf{E}$ for the uncontrolled reference flow (denoted as Ref) and for the flow subject to FAC, FIC and IOC. In the reference flow, the majority of the energy is contained in u (87%) and the remaining energy in v (10%) and w (3%). After we apply control, we see that, consistent with figures 6.3 and 6.4 and table 6.1, the performances of FAC, FIC and IOC are all similar to each other. The overall reduction of energy ($\mathbf{E}_{u,v,w}$) is $\approx$ 85%, where $\mathbf{E}_u$ is reduced by $\approx$ 90%, $\mathbf{E}_v$ by $\approx$ 50% and $\mathbf{E}_w$ by $\approx$ 67%. Therefore, the control system is most effective in reducing the streamwise velocity component, which also carries most of the energy.

6.5.3 Control across wall heights

So far, we have looked at the control performance over an entire channel half. It is also important to study the performance of the controllers across wall heights.

For reference, we first compute the normalized kinetic energy of the uncontrolled flow $\mathbf{E}_z$ as a function of wall-normal location z:

$$\mathbf{E}_z(z) = \frac{\sum_{i\in k_x, j\in k_y} \|\hat{\boldsymbol{y}}_{ref}(i,j,z)\|_2^2}{\max(\sum_{i\in k_x, j\in k_y} \|\hat{\boldsymbol{y}}_{ref}(u,j,z)\|_2^2)}. \tag{6.19}$$

Figure 6.6 shows $\mathbf{E}_z$ as a function of z on the right axis. As in the previous section, the signal $\hat{\boldsymbol{y}}$ represents: all the three velocity components (figure 6.6a), the streamwise velocity component (figure 6.6b), the spanwise velocity component (figure 6.6c), or the wall-normal velocity component (figure 6.6d). From the plot of $\mathbf{E}_z$ (in blue), we observe that u and v are strongest near the wall (figures 6.6b and 6.6c), while w is strongest near the channel center (figure 6.6d).

We now look at the reduction in the kinetic energy of the controlled flow ϵ as a function of wall-normal location z:

$$\epsilon(z) = 1 - \frac{\sum_{i\in k_x, j\in k_y} \|\hat{\boldsymbol{y}}_{ctrl}(i,j,z)\|_2^2}{\sum_{i\in k_x, j\in k_y} \|\hat{\boldsymbol{y}}_{ref}(i,j,z)\|_2^2}. \tag{6.20}$$

There are four different definitions of ϵ (depending on $\hat{\boldsymbol{y}}$), which are shown in figures 6.6a-6.6d on the left axis. As before, $\hat{\boldsymbol{y}}$ represents either all three (figure 6.6a) or individual (figure 6.6b-d) velocity components. Parameter ϵ is shown for FAC (ϵ_{FA}), FIC (ϵ_{FI}), and IOC (ϵ_{IO}). By definition, ϵ is between $0 \leq \epsilon \leq 1$, where 1 (100%) indicates the elimination of all kinetic energy and 0 (0%) indicates that there is no reduction in kinetic energy.

From figure 6.6a we observe that the performance for all control problems is best near $z_s = z_a = 0.32$ (where $\epsilon(z)$ is lowest) and decreases with distance from it. A significant reduction of velocity perturbations is observed at all wall heights. Similar values of ϵ are achieved in figure 6.6b for the streamwise velocity component, which can be explained by u being the most energetic component (figure 6.5). FAC and IOC set v in figure 6.6c close to zero around $z_s = z_a = 0.32$. While FIC also reduced the energy carried by v, the reduction is not as strong as in the case of FAC and IOC. Figure 6.6d shows that all three problems set the wall-normal velocity close to zero at one wall height. The transport of momentum in the vicinity of this wall height is attenuated, which prevents the formation of streamwise structures (Sadayoshi and Tomoaki, 2005). This mechanism is employed in opposition-controlled wall-bounded

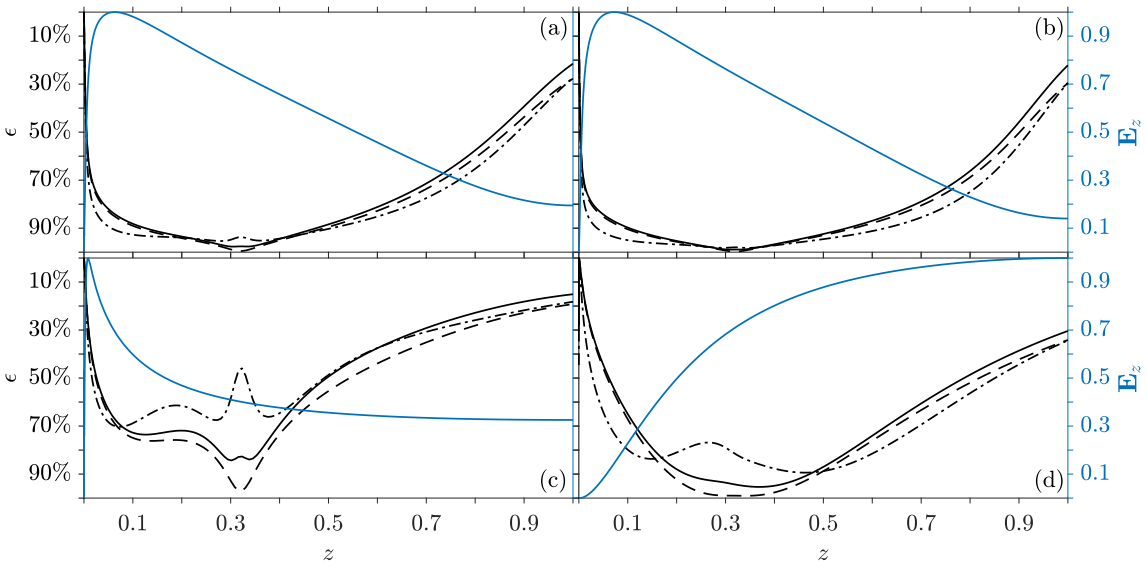

FIGURE 6.6: Left axis: The reduction of kinetic energy ($\epsilon_{FA}(--)$,$\epsilon_{FI}(-\cdot-)$ and $\epsilon_{IO}(—)$) as a function of z. Right axis: the normalized kinetic energy $\mathbf{E}_z(—)$ as a function of z. Results are shown for (a) $[u, v, w]$, (b) $[u]$, (c) $[v]$ and (d) $[w]$.

flows (Hammond et al., 1998), where the controller is specifically designed to create a plane of zero wall-normal momentum that is referred to as a "virtual wall". We did not choose an opposition control design but instead selected a general cost function to reduce velocity perturbations everywhere. Since the three $\mathcal{H}_2$-optimal control designs seem to all create a "virtual wall", the results suggest that this approach is the most effective one in the control of turbulent channel flows utilizing single-plane sensors and single-plane actuators.

Let us compare ϵ_{FI}, where the flow field is known everywhere, to ϵ_{IO}, where only one location is known. We see that FIC performs marginally better than IOC everywhere outside the vicinity of the sensor at $z = 0.32$. This suggests that IOC is focusing its control efforts on the region near $z = 0.32$ (that it 'knows well') at the expense of a slight reduction in control performance everywhere else. If we compare ϵ_{FA}, where actuation is provided everywhere, to ϵ_{IO}, where actuation is provided at only one location, we can see that they are almost identical to each other except in the vicinity of the single actuator at $z = 0.32$. Therefore, near $z = 0.32$, the performance of IOC must be primarily limited by the single actuator; while at all other locations its performance is limited by the single sensor.

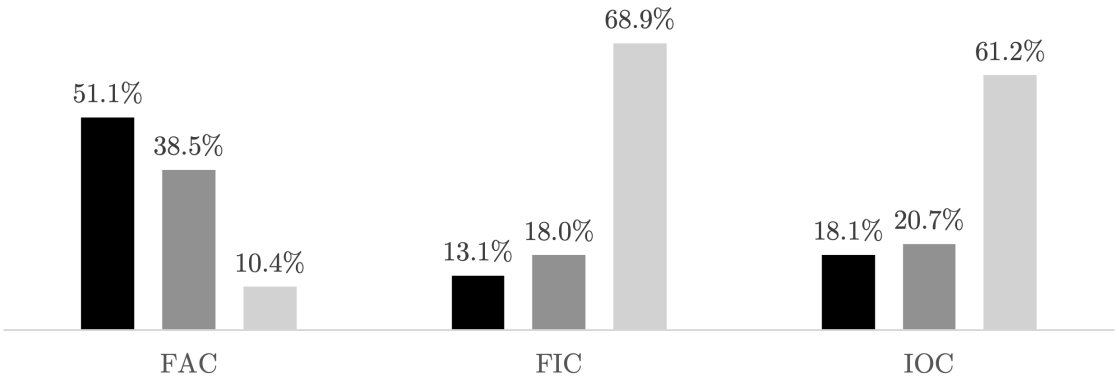

FIGURE 6.7: The distribution of forcing between $\mathbf{E}_{f_x}$ (■), $\mathbf{E}_{f_y}$(■) and $\mathbf{E}_{f_z}$(■), where $\mathbf{E}_{f_x} + \mathbf{E}_{f_y} + \mathbf{E}_{f_z} = 1$.

6.5.4 Control forces

So far, we have studied the effect that the three control problems have on the velocity perturbations. Each problem continuously forces the flow to prevent perturbations from growing. In this section, we study these continuous forces. In particular, we look at the percentage of the forcing that is applied to the streamwise, spanwise and wall-normal directions. For this purpose, in figure 6.7, we plot the energy consumed by f_x, f_y and f_z as a percentage of the total $\boldsymbol{f}$, which we refer to as $\mathbf{E}_{f_x}$, $\mathbf{E}_{f_y}$ and $\mathbf{E}_{f_z}$ (see Appendix D.3 for the $\mathcal{H}_2$-norms):

$$\mathbf{E}_f = \frac{\sum_{i\in k_x, j\in k_y} \|\hat{f}(i,j)\|_2^2}{\sum_{i\in k_x, j\in k_y} \|\hat{\boldsymbol{f}}(i,j)\|_2^2}. \tag{6.21}$$

We observe that in FAC, which actuates the flow everywhere, the largest forcing component is $\mathbf{E}_{f_x}$ (streamwise), and the smallest forcing component is $\mathbf{E}_{f_z}$ (wall-normal). In FIC and IOC, which actuate the flow at only one location, the largest forcing component is $\mathbf{E}_{f_z}$ (wall-normal) and the smallest forcing component is $\mathbf{E}_{f_x}$ (streamwise). We can explain these results using two mechanisms:

(i) Direct elimination: velocity perturbations are counter-perturbed as soon as they are detected, which is mostly employed by FAC. One may ask why FAC only allocates $\mathbf{E}_{f_x} \approx 51\%$ of energy to f_x even though the energy reduction in the streamwise direction is responsible for $\approx 91\%$ of the overall energy reduction. The answer is that, once we apply control, streamwise perturbations

are not given a chance to amplify, which allows the controller to allocate more energy to f_y and f_z.

(ii) Indirect elimination: is used for wall heights at which actuation is not available. As soon as velocity perturbations are detected, the actuator introduces counter-perturbations in the wall-normal direction. These counter-perturbations help to suppress the streamwise vorticity perturbations that give rise to the energetic streamwise velocity perturbations. The indirect elimination technique is employed by FIC and IOC, and explains their high allocation of energy to f_z ($\mathbf{E}_{f_z} = 68.9\%$ in FIC and $\mathbf{E}_{f_z} = 61.2\%$ in IOC). The streamwise f_x and spanwise f_y forces primarily affect control locally around the actuator location and as a consequence are given less priority.

6.6 Conclusions

We have considered linear feedback control of a turbulent channel at $\mathrm{Re}_\tau = 2000$ using the linearized Navier-Stokes equations (LNS). The linear operator is augmented with an eddy viscosity (following many previous studies) and is assumed to be stochastically forced. The LNS equation was employed because it provides insight into control, without the requirement of running costly DNS or experimental studies. The particular focus was on three control problems: (i) FAC, where measurements are limited to one optimal wall height, but actuation is available everywhere; (ii) FIC, where actuators are limited to one optimal wall height, but measurements are available everywhere; and (iii) IOC, where sensors and actuators are limited to one optimal wall height. All three problems performed similarly. From these results, we can infer that measuring everywhere does not significantly increase the control performance when we are limited to one actuator location. Likewise, actuating everywhere does not significantly increase the control performance when we are limited to one sensor location. Our three control problems perform best for the largest scales that (i) are high in energy when stochastically forced, (ii) exhibit large transient growth and (iii) are coherent over large wall-normal distances. Therefore, we choose to look at a specific range of wavenumbers ($|k_x| \leq 0.5$ and $|k_y| \leq 6$), corresponding to the largest scales, in more detail. We saw an overall reduction in kinetic energy of $\approx 85\%$, where the streamwise velocity component was most attenuated

(by $\approx 90\%$). To further analyze the largest scales, we looked at the effect of control at individual wall heights. The performance was best near the sensor and actuator location ($z = 0.32$, which was based on the optimal placement results of chapter 5) and deteriorated with distance from it. Finally, we looked at the distribution of the forcing between the streamwise f_x, spanwise f_y and wall-normal f_z components. For FAC, f_x was strongest and f_z weakest, while for FIC and IOC, f_z was strongest and f_x weakest. FAC, which forces the flow everywhere, relies on directly eliminating structures as soon as they are detected, which is why it prioritizes streamwise forcing f_x. Meanwhile FIC and IOC, which only force the flow at a single location, mainly employ wall-normal forcing (f_z), thereby eliminating velocity perturbations by leveraging the mean wall-normal shear.

Chapter 7

Conclusions

7.1 Complex Ginzburg-Landau equation

The first part of the thesis (chapter 3) studied sensor and actuator placement in the complex Ginzburg-Landau equation. Specifically, the optimal placement of a single sensor, a single actuator, or both was considered. Looking at the physical characteristics of the flow, although useful for understanding inherent limitations, did not by itself reveal the optimal placements. Instead, as in previous studies, they had to be found iteratively because of the following predicament: one can neither design a controller without placement nor determine the placement performance before designing the controller.

Studying the placement problem made clear two conflicting trade-offs:

- The sensor needs to be placed far enough downstream to estimate the most perturbed region of the domain; and far enough upstream to estimate the remaining domain. This trade-off causes the optimal sensor location to move downstream as the stability decreases.

- The actuator needs to be placed far enough upstream to control the region of the domain where the external disturbances have the greatest potential for amplification; and far enough downstream to control the remaining domain. This trade-off causes the optimal actuator location to move upstream as the stability decreases.

In the future, it would be interesting to see if these two trade-offs are also observed in similar flows, such as jets, wakes or cavities. (A recent study by Jin et al. (2018), which looked at the control of vortex shedding behind a cylinder, found that the optimal sensor location shifts downstream as the Reynolds number increases, which is consistent with the results of this thesis.)

7.2 Turbulent channel flow

The second part of this thesis (chapters 4, 5 and 6) considered linear estimation and control of the largest scales in an incompressible turbulent channel flow at a friction Reynolds number of $\mathrm{Re}_\tau = 2000$. A linear Navier-Stokes (LNS) model was obtained by forming a linear Navier-Stokes operator about the turbulent mean and augmenting it with an eddy viscosity. Velocity perturbations were then generated by stochastically forcing the LNS operator at the largest scales; and the objective was to then estimate and control these perturbations. The LNS equations were employed because they provide insight into estimation and control, without the requirement of running costly DNS or experimental studies. The work was described in three chapters.

Chapter 4 looked at linear estimation. The results built on earlier work by Illingworth et al. (2018) which was performed at $\mathrm{Re}_\tau = 1000$ (with significantly less time-resolved data available). Using velocity measurements as an input, it was possible to estimate the largest scales with reasonable accuracy for a range of wavenumber pairs, measurement planes, and estimation planes. When replacing the velocity measurements with wall shear stress measurements, it was still possible to estimate the largest scales with reasonable accuracy, although the estimator's performance was significantly reduced. The two measurement types showed consistent estimation results of (i) an under-prediction near the channel centre, (ii) an over-prediction near the channel wall, and (iii) degradation of the estimation performance close to the wall. Furthermore, the results were verified by replacing the measurements generated by stochastically forcing the LNS model with data from direct numerical simulations (DNS).

Chapter 5 looked at sensor and actuator placement for estimation and control. The wall-normal locations for which single-plane sensors and single-plane actuators

were most effective were determined by considering two arrangements: (i) placing them at the wall; and (ii) placing them some distance off the wall. To do so, the iterative gradient minimisation algorithm from chapter 3 was employed to optimise the off-wall placement (a modified version of the iterative minimisation algorithm was used for DNS-based measurements). It was found that (i) the off-wall placements perform better than the at-wall placements, (ii) streamwise velocity measurements are best for estimation and (iii) wall-normal body forces are best for control.

Chapter 6 looked at control, with a particular focus on three set-ups (which are similar to the set-ups employed in chapter 3): (i) the controller can actuate the flow everywhere but is limited to measurements at a single optimal wall height; the controller has access to measurements everywhere, but actuation is limited to a single optimal wall height; and (iii) the controller is limited to sensors and actuators at a single optimal wall height. The control problems performed best for the largest scales that (i) are high in energy when stochastically forced, (ii) exhibit large transient growth and (iii) are coherent over large wall-normal distances. Overall, all three problems performed similarly. These results are based on an analysis conducted upon the linearized Navier Stokes equations and for the particular disturbance model employed. They suggest that measuring everywhere does not significantly increase the control performance when control is limited to a single actuator location. Likewise, actuating everywhere does not significantly increase the control performance when control is limited to a single sensor location. As a consequence, control does not improve when we add more sensors (when a single actuator is available) or when we add more actuators (when a single sensor is available).

7.2.1 Future research

We now consider four possible areas for future research.

The first possible area for future research is the replication of the estimation and control results of chapters 4, 5 and 6 in DNS and experiments. While the thesis has successfully used linear estimation with DNS data, it has not done so with experimental data. Additionally, control was not considered in either DNS or experiments due to the high cost. The number of sensors and actuators required would depend on the number of wavenumber pairs (k_x k_y). For sensing, arrays of

hot wires could be employed, and for actuation, blowing and suction at the wall could be employed.

The second possible area for future research is to study linear estimation and control at different Reynolds numbers. The results from the LNS operator have shown that both estimation and control improve in performance as the Reynolds number increases (§5.3.5 and §5.4.4). It suggests that linear mechanisms play a more important role in the linear Navier-Stokes operator at higher Reynolds numbers.

The third possible area for future research is the study of robustness. Controlling perturbations in the flow will alter the mean velocity profile and with it the linear model itself (which is formed about the mean flow). The controller needs to be robust to account for the changes in the mean flow due to the action of control. Controller robustness can be achieved through the linear model, e.g. by by accounting for the fluctuating mean velocity (Moarref and Jovanović, 2012), and through the controller design process itself (e.g. Zhou and Doyle, 1998; Doyle et al., 2013).

The fourth possible area for future research involves the implementation of more advanced estimators and controllers, which becomes important (i) when considering the effect of Reynolds stresses and (ii) when estimating and controlling structures at smaller scales. Examples include spectral linear stochastic estimation (Baars et al., 2016), the inclusion of the second-order statistics in the linear model (Zare et al., 2017) and non-linear estimator and controller designs (Lauga and Bewley, 2004). Certain designs, such as the Extended Kalman Filter (EKF) (Fowler, 2012), are not feasible in the foreseeable future due to their high computational cost (of the order of DNS studies). However, the high resolution of the EKF may not be necessary because (i) introduced modelling errors can be compensated for by the feedback loop and (ii) one only needs to discretise the model enough to capture the features of interest (Jones et al., 2015). Therefore, low-cost alternatives, such as the Ensemble Kalman Filter (EnKF), exist. The EnKF is a statistical approximation to the EKF (Fowler, 2012); it would be interesting to compare EnKF to existing estimators.

Appendix A

Sensor and actuator placement trade-offs for a linear model of spatially developing flows[1]

A.1 Spectral discretisation of the continuous equation

For this study, we considered three discretisation methods: Hermite collocation on an infinite domain (Weideman and Reddy, 2000), Chebyshev collocation on a finite domain (Trefethen, 2000) and Chebyshev collocation on an infinite domain (Schmid and Henningson, 2012). Convergence and scaling studies showed convergence for all three methods. We selected the finite Chebyshev collocation methods for this study because it requires the lowest order for convergence.

We employ Chebyshev collocation of order $N_c = N + 1 = 151$, scale the Chebyshev points by $L = 25$ and enforce boundary conditions to obtain at a system with N grid points, i.e. $\boldsymbol{x} = [x_1, x_2, \cdots x_i, \cdots x_N]^T$, extending from $-L < x_i < L$. Discrete integration is implemented using the Clenshaw–Curtis quadrature, which provides weights w_i at each Chebyshev point and is used to form the integration matrix:

$$\mathbf{M} = \mathrm{diag}(L[w_1, w_2, \ldots w_i \ldots, w_N]). \tag{A.1}$$

[1] Appendix of Chapter 3

P	$\boldsymbol{w}$	$\boldsymbol{z}$	$\boldsymbol{y}$	$\boldsymbol{u}$	$\mathbf{B}_w$	$\mathbf{B}_u$	$\mathbf{C}_z$	$\mathbf{C}_y$	$\mathbf{D}_u$	$\mathbf{D}_w$
OE	$\begin{bmatrix}\boldsymbol{d}\\ \boldsymbol{n}\end{bmatrix}$	$\boldsymbol{e}$	$\boldsymbol{y}$	$\hat{\boldsymbol{q}}$	$\begin{bmatrix}\mathbf{B}_d\\ \mathbf{0}\end{bmatrix}^T$	$\mathbf{0}$	$\mathbf{M}^{\frac{1}{2}}$	$\mathbf{C}_y$	$-\mathbf{M}^{\frac{1}{2}}$	$\begin{bmatrix}\mathbf{0}\\ v\end{bmatrix}^T$
FIC	$\boldsymbol{d}$	$\boldsymbol{z}$	$\boldsymbol{q}$	$\boldsymbol{u}$	$\mathbf{B}_d$	$\mathbf{B}_u$	$\begin{bmatrix}\mathbf{M}^{\frac{1}{2}}\\ 0\end{bmatrix}$	0	$\begin{bmatrix}\mathbf{0}\\ \alpha\end{bmatrix}$	0
IOC	$\begin{bmatrix}\boldsymbol{d}\\ \boldsymbol{n}\end{bmatrix}$	$\boldsymbol{z}$	$\boldsymbol{y}$	$\boldsymbol{u}$	$\begin{bmatrix}\mathbf{B}_d\\ \mathbf{0}\end{bmatrix}^T$	$\boldsymbol{B}_u$	$\begin{bmatrix}\mathbf{M}^{\frac{1}{2}}\\ 0\end{bmatrix}$	$\mathbf{C}_y$	$\begin{bmatrix}\mathbf{0}\\ \alpha\end{bmatrix}$	$\begin{bmatrix}\mathbf{0}\\ v\end{bmatrix}^T$

TABLE A.1: The inputs, outputs, and matrices for the OE, FIC and IOC problems.

The discrete representation is then of the form:

$$\dot{\boldsymbol{q}}(t) = (-\nu\mathbf{D} + \kappa\boldsymbol{\Delta} + \mathrm{diag}(\boldsymbol{\mu}))\,\boldsymbol{q}(t) + \mathbf{B}_d\boldsymbol{d}(t) = \mathbf{A}\mathbf{q}(t) + \mathbf{B}_d\boldsymbol{d}(t), \tag{A.2}$$

where $\mathbf{D}$ and $\boldsymbol{\Delta}$ are the first- and second-order Chebyshev differentiation matrices with suitable boundary conditions and $\mathbf{A}$ is the discrete complex Ginzburg-Landau operator. At each grid point i, we apply stochastic forcing which is white in space and time with a covariance $\mathbb{E}(d_i\bar{d}_i) = 1$, where $\mathbb{E}$ the expected value. Setting $\mathbf{B}_d = \mathbf{M}^{-\frac{1}{2}}$ ensures that the disturbances are grid size independent.

A.2 The systems for estimation and control

This section will supplement §3.4 by describing the OE, FIC and IOC problems (Kim and Bewley, 2007; Skogestad and Postlethwaite, 2007; Aström and Murray, 2010). The OE, FIC and IOC three problems can be cast into the same general form:

$$\mathbf{P}: \begin{bmatrix}\dot{\boldsymbol{q}}(t)\\ \boldsymbol{z}(t)\\ \boldsymbol{y}(t)\end{bmatrix} = \begin{bmatrix}\mathbf{A} & \mathbf{B}_w & \mathbf{B}_u\\ \mathbf{C}_z & \mathbf{0} & \mathbf{D}_u\\ \mathbf{C}_y & \mathbf{D}_w & \mathbf{0}\end{bmatrix}\begin{bmatrix}\boldsymbol{q}(t)\\ \boldsymbol{w}(t)\\ \boldsymbol{u}(t)\end{bmatrix}. \tag{A.3}$$

Table A.1 lists the inputs, outputs and system matrices for the OE, FI and IOC problems. These signals and matrices were already introduced in equation (3.4) and

§3.4. A single sensor is placed at x_s and a single actuator is placed at x_a. We use the expressions from the previous literature (Bagheri et al., 2009; Chen and Rowley, 2011) to define the spatial extent of the sensor $\mathbf{C}_y$ and actuator $\mathbf{B}_u$ as Gaussian functions:

$$\mathbf{C}_y = \exp\left\{-\left(\frac{\boldsymbol{x}-x_s}{\sqrt{2}\sigma}\right)^2\right\}^T \mathbf{M}, \tag{A.4a}$$

$$\mathbf{B}_u = \exp\left\{-\left(\frac{\boldsymbol{x}-x_a}{\sqrt{2}\sigma}\right)^2\right\}, \tag{A.4b}$$

where $\sigma = 0.4$ is the variance of the Gaussian function.

A.3 Optimal placement

Following the work of Chen and Rowley (2011, 2014, 2015) we use a location perturbation technique to calculate changes of γ with respect to the sensor and actuator locations. These derivatives can be employed with a gradient minimisation technique to solve for the optimal γ. Examples of gradient minimisation techniques include the Polak–Ribiere conjugate gradient method or the Broyden–Fletcher–Goldfarb-Shannon quasi-Newton algorithm.

We obtained the IOC problem's derivatives with respect to the sensor and actuator location from Chen and Rowley (2011). To obtain the OE problem's derivative with respect to the sensor location and the FIC problem's derivatives with respect to the actuator location we adapted the work of Chen and Rowley (2011):

$$\frac{\delta(\gamma_{OE}^2)}{\delta x_s} = \frac{\mathrm{tr}(\mathbf{C}_z \delta\mathbf{Y}\mathbf{C}_z^*)}{\delta x_s}, \qquad \frac{\delta(\gamma_{FI}^2)}{\delta x_a} = \frac{\mathrm{tr}(\mathbf{B}_w^* \delta\mathbf{X}\mathbf{B}_w)}{\delta x_a}. \tag{A.5}$$

A.4 The root mean square of the norm

The root mean square (rms) value $\epsilon(x)$ is defined to have the following property:

$$\gamma^2 = \int_{-\infty}^{\infty} \epsilon^2(x)dx = \mathrm{sum}\left(\mathrm{diag}\left(\mathbf{\Gamma}\right)\right) = \mathrm{sum}\left(\mathbf{M}\boldsymbol{\epsilon} \odot \boldsymbol{\epsilon}\right), \tag{A.6}$$

where $\mathbf{\Gamma}$ describes the covariance matrix (Bagheri et al. (2009) and §A.5), $\boldsymbol{\epsilon}$ describes the discrete rms values and $\odot$ the Hadamard product. We can solve for $\boldsymbol{\epsilon}$ by rearranging (A.6):

$$\boldsymbol{\epsilon} = \left(\mathbf{M}^{-1}\mathrm{diag}\left(\mathbf{\Gamma}\right)\right)^{\odot\frac{1}{2}}, \tag{A.7}$$

where $()^{\odot}$ is the Hadamard power.

A.5 Covariance matrix

This section shows how the covariance matrix $\mathbf{\Gamma}$ is derived. It is used in Appendix A.4 to derive the R.M.S. values introduced in equation= 3.8.

The covariance matrix can either be in correlation to the inputs ($\mathbf{\Gamma}_O$) using the Observability Gramian $\mathbf{W}_O$ or in correlation to the outputs ($\mathbf{\Gamma}_C$) using the Controllability Gramian $\mathbf{W}_C$. To find $\mathbf{W}_O$ or $\mathbf{W}_C$ we form the LFT. The general structure of LFT is:

$$\begin{bmatrix}\dot{\boldsymbol{x}}(t)\\ \boldsymbol{z}(t)\end{bmatrix} = \begin{bmatrix}\mathbf{Z_A} & \mathbf{Z_B}\\ \mathbf{Z_C} & \mathbf{0}\end{bmatrix}\begin{bmatrix}\boldsymbol{x}(t)\\ \boldsymbol{w}(t)\end{bmatrix}, \tag{A.8}$$

where $\boldsymbol{x}$ represents the system's internal states, $\boldsymbol{w}$ the external inputs and $\boldsymbol{z}$ the external outputs.

With (A.8) we can solve the two Lyapunov equations shown in A.9 and A.10:

$$\mathbf{Z_A}\mathbf{W}_C + \mathbf{W}_C\mathbf{Z_A}^* + \mathbf{Z_B}\mathbf{Z_B}^*, \tag{A.9}$$

$$\mathbf{Z_A}^*\mathbf{W}_O + \mathbf{W}_O\mathbf{Z_A} + \mathbf{Z_C}^*\mathbf{Z_C}, \tag{A.10}$$

to obtain the Gramians:

$$\mathbf{\Gamma}_C = \mathbf{Z_C}\mathbf{W}_C\mathbf{Z_C}^*, \qquad \mathbf{\Gamma}_O = \mathbf{Z_B}\mathbf{W}_O\mathbf{Z_B}^*. \tag{A.11}$$

We use the first $N \times N$ elements of these Grammians to solve for $\boldsymbol{\epsilon}$ in equation A.7. The remaining elements correspond to the contributions of the sensors noise $\mathbf{V}^{1/2}\boldsymbol{n}$ or actuator cost $\mathbf{R}^{1/2}\boldsymbol{u}$ to the overall norms γ.

Appendix B

Linear estimation of coherent structures in wall-bounded turbulence at $\mathrm{Re}_\tau = 2000$[1]

B.1 Linear state space model of the flow

The state-space model (equation (4.3)) of the linear model is (equation (4.1)):

$$\frac{d}{dt}\begin{bmatrix}\hat{\boldsymbol{w}}\\ \hat{\boldsymbol{\eta}}\end{bmatrix} = \begin{bmatrix}\Delta^{-1}\mathcal{L}_{OS} & 0\\ -\mathrm{j}k_y U' & \mathcal{L}_{SQ}\end{bmatrix}\begin{bmatrix}\hat{\boldsymbol{w}}\\ \hat{\boldsymbol{\eta}}\end{bmatrix} + \mathbf{M}^{-\frac{1}{2}}\begin{bmatrix}-\mathrm{j}k_x\Delta^{-1}\mathcal{D} & -\mathrm{j}k_y\Delta^{-1}\mathcal{D} & -k^2\Delta^{-1}\\ \mathrm{j}k_y & -\mathrm{j}k_x & 0\end{bmatrix}\begin{bmatrix}\hat{\boldsymbol{d}}_x\\ \hat{\boldsymbol{d}}_y\\ \hat{\boldsymbol{d}}_z\end{bmatrix}, \tag{B.1a}$$

$$\begin{bmatrix}\hat{\boldsymbol{u}}\\ \hat{\boldsymbol{v}}\\ \hat{\boldsymbol{w}}\end{bmatrix} = \frac{1}{k^2}\begin{bmatrix}\mathrm{j}k_x\mathcal{D} & -\mathrm{j}k_y\\ \mathrm{j}k_y\mathcal{D} & \mathrm{j}k_x\\ k^2 & 0\end{bmatrix}\begin{bmatrix}\hat{\boldsymbol{w}}\\ \hat{\boldsymbol{\eta}}\end{bmatrix}, \tag{B.1b}$$

where

$$\mathcal{L}_{OS} = -\mathrm{j}k_x U(z)\Delta + \mathrm{j}k_x U''(z) + \nu_T\Delta^2 + 2\nu_T'\mathcal{D}\Delta + \nu_T''\left(\mathcal{D}^2 + k^2\right), \tag{B.2a}$$

$$\mathcal{L}_{SQ} = -\mathrm{j}k_x U(z) + \nu_T\Delta + \nu_T'\mathcal{D}, \tag{B.2b}$$

[1] Appendix of Chapter 4

$\mathcal{D} = \frac{\partial}{\partial z}$, $()' = \frac{\partial}{\partial z}()$, $k^2 = k_x^2 + k_y^2$, and $\Delta = \mathcal{D}^2 - k^2$. The boundary conditions are: $\hat{\boldsymbol{w}}_{wall}(t) = \hat{\boldsymbol{w}}'_{wall}(t) = \hat{\boldsymbol{\eta}}_{wall}(t) = 0$. We set $\mathbf{B}_d = \mathbf{M}^{-1/2}\mathbf{B}$ to achieve grid-independence, where $\mathbf{M}$ is an integration matrix corresponding to Clenshaw-Curtis quadrature (Trefethen, 2000).

The obtain instead the wall shear stress (Hœpffner et al., 2005; Bewley and Protas, 2004) we replace equation (B.1b) with:

$$\tau_x = \frac{1}{\mathrm{Re}_\tau}\frac{du}{dz}\bigg|_{wall} = \frac{\mathrm{j}}{\mathrm{Re}_\tau k^2}\begin{bmatrix} k_x\mathcal{D}^2 & -k_y\mathcal{D} \end{bmatrix}\begin{bmatrix} \hat{\boldsymbol{w}} \\ \hat{\boldsymbol{\eta}} \end{bmatrix}\bigg|_{wall}. \tag{B.3}$$

Appendix C

Sensor and actuator placement in wall-bounded turbulence at $\mathrm{Re}_\tau = 2000$[1]

C.1 Spectral discretisation of the channel equation

We generate the eddy viscosity profile and mean velocity profile (equation 5.4) for one channel half using Chebyshev collocation of order $N_\nu = 200$ (except for figures 5.5 and 5.8, where $N_\nu = 600$) (Trefethen, 2000). Barycentric Lagrange interpolation (Berrut and Trefethen, 2004) is used to map the results to both channel halves. For the main channel flow (equation 5.5), we employ Chebyshev collocation of order $N_c = 200$. When looking at results for a single channel half, we employ barycentric interpolation to map the outputs of ($\boldsymbol{u} = \mathbf{C}\boldsymbol{q}$) onto a Chebyshev grid of order $N_{out} = 200$. (Convergence studies show convergence for all grids at the wavenumber pairs considered.) We linearly interpolate the DNS data onto a high-resolution Chebyshev-grid before we employ barycentric interpolation to map the DNS-data onto the grid used for the channel-half ($N_{out} = 200$).

[1] Appendix of Chapter 5

Integration is implemented with the Clenshaw-Curtis quadrature (Trefethen, 2000), which provides weights w_i at each Chebyshev point and is used to form the integration matrix: $\mathbf{M} = \mathrm{diag}([w_1, w_2, \dots w_i \dots, w_N])$.

When looking at predicted LM results and for the estimator and controller design, we apply random forcing at each grid point i which is white in space and time with a covariance $\mathbb{E}(d_i \bar{d}_i) = 1$, where $\mathbb{E}$ the expected value.

C.2 Sensor and actuator signals

The velocity field $\boldsymbol{u}$ is either provided by the DNS data, which we refer to as DNS-OE, or the LM, which we refer to as LM-OE. We can use $\mathbf{C}_y$ to generate any measurement types that are considered:

$$\boldsymbol{y} = \mathbf{C}_y \mathbf{C} \boldsymbol{q} + \boldsymbol{n}, \tag{C.1}$$

where $\mathbf{C}_y$ represents the sensor matrix and $\boldsymbol{n}$ the sensor noise.

The off-wall measurement signals are:

$$\boldsymbol{y}|_{flow} = \begin{bmatrix} u_s \\ v_s \\ w_s \end{bmatrix} + \boldsymbol{n} = \begin{bmatrix} \mathbf{g}(z_s) & 0 & 0 \\ 0 & \mathbf{g}(z_s) & 0 \\ 0 & 0 & \mathbf{g}(z_s) \end{bmatrix} \begin{bmatrix} \hat{u} \\ \hat{v} \\ \hat{w} \end{bmatrix} + \boldsymbol{n}, \tag{C.2}$$

where

$$\mathbf{g}(z_s) = \exp\left\{ -\left(\frac{\mathbf{z} - z_s}{2\sigma_s} \right)^2 \right\}^T \mathbf{M}, \tag{C.3}$$

is a Gaussian function, $\mathbf{z} = [z_1, z_2 \cdots z_{N_{out}+1}]^T$ are Chebyshev grid points, z_s is the sensor location and σ_s defines the width. We set $\sigma_s = 0.01$, which is wide enough for the sensor to be independent of the output-grid resolution (N_{out}).

The at-wall measurement signals are:

$$\boldsymbol{y}|_{wall} = \begin{bmatrix} \tau_x \\ \tau_y \end{bmatrix} + \boldsymbol{n} = \frac{\mathcal{D}}{\mathrm{Re}_\tau} \begin{bmatrix} \hat{\boldsymbol{u}} \\ \hat{\boldsymbol{v}} \end{bmatrix}_{wall} + \boldsymbol{n}, \tag{C.4}$$

which represent streamwise τ_x and spanwise τ_y shear (Bewley and Liu, 1998). We set the covariance $\mathbb{E}(\boldsymbol{n}\boldsymbol{n}^*) = v = 10^{-4}$ such that the sensor noise is negligible for both off-wall and at-wall measurements.

The actuator force $\boldsymbol{f}$ is directly applied to the main flow (equation 5.5):

$$\dot{\boldsymbol{q}}(t) = \mathbf{A}\boldsymbol{q}(t) + \mathbf{B}_d\boldsymbol{d}(t) + \boldsymbol{f}(t) \tag{C.5}$$

at a single wall-normal location (z_a) for off-wall forcing:

$$\boldsymbol{f}|_{flow} = \begin{bmatrix} f_x \\ f_y \\ f_z \end{bmatrix} = \mathbf{B} \begin{bmatrix} \mathbf{h}(z_a) & 0 & 0 \\ 0 & \mathbf{h}(z_a) & 0 \\ 0 & 0 & \mathbf{h}(z_a) \end{bmatrix} \boldsymbol{b}, \tag{C.6}$$

where

$$\mathbf{h}(z_a) = \exp\left\{ -\left(\frac{\mathbf{z} - z_a}{2\sigma_a} \right)^2 \right\}, \tag{C.7}$$

is a Gaussian function, $\mathbf{z} = [z_1, z_2 \cdots z_{N_c+1}]^T$ are Chebyshev grid points, $\boldsymbol{b}$ is the control signal, and σ_a defines the width. We set $\sigma_a = 0.02$, which is wide enough to be independent of the system-grid resolution (N_c).

At-wall forcing is set by the first Dirichlet boundary condition (see Hoepffner (2007) for an explanation):

$$\boldsymbol{f}|_{wall} = \hat{w}_{wall} = \mathbf{H}_1\boldsymbol{b} - \mathbf{H}_2\dot{\boldsymbol{b}}, \tag{C.8}$$

where $\mathbf{H}_1$ and $\mathbf{H}_2$ relate the control signal $\boldsymbol{b}$ to the states $\boldsymbol{q}$ of the system.

The control signal's magnitude penalisation for both off-wall and at-wall forcing is set to be negligible ($\alpha = 10^{-4}$) but large enough to avoid ill-posedness of the system (Oehler and Illingworth, 2018a).

Appendix D

Linear control of coherent structures in wall-bounded turbulence at $\mathrm{Re}_\tau = 2000$[1]

D.1 Spectral discretisation of the channel equation

We generate the eddy viscosity profile and mean velocity profile (equation (6.2)) for one channel half using Chebyshev collocation of order $N_\nu = 200$ (Trefethen, 2000). Barycentric Lagrange interpolation (Berrut and Trefethen, 2004) is used to map the results to both channel halves. For the main channel flow (equation (6.3)) we employ Chebyshev collocation of order $N_c = 200$. When looking at results for a single channel half, we employ barycentric interpolation to map the outputs onto a Chebyshev grid of order $N_{out} = 200$. We apply stochastic forcing, which is white in space and time, at each grid point i with a covariance $\mathbb{E}(\hat{d}_i \hat{d}_i^*) = 1$, where $\mathbb{E}$ the expected value. Integration is implemented with the Clenshaw-Curtis quadrature (Trefethen, 2000), which provides weights w_i at each Chebyshev point and is used to form the integration matrix: $\mathbf{M} = \mathrm{diag}([w_1, w_2, \ldots w_i \ldots, w_N])$.

[1] Appendix of Chapter 6

D.2 Sensor and actuator matrices

The measurement signal is defined as:

$$\hat{\boldsymbol{m}} = \mathbf{C}_y \hat{\boldsymbol{u}} + \hat{\boldsymbol{n}} = \mathbf{C}_y \mathbf{C} \hat{\boldsymbol{q}} + \hat{\boldsymbol{n}} = \mathbf{C}_m \hat{\boldsymbol{q}} + \hat{\boldsymbol{n}}, \tag{D.1}$$

where $\hat{\boldsymbol{n}}$ is the sensor noise and $\mathbf{C}_y$ represents the sensor matrix. We treat $\hat{\boldsymbol{n}}$ as an unknown forcing that is white in time, and we set the covariance $\mathbb{E}(\hat{\boldsymbol{n}}\hat{\boldsymbol{n}}^*) = (10^{-4})\mathbf{I} = \mathbf{V}^{1/2}$ such that the sensor noise is negligible but the system is well-posed. The sensor matrix $\mathbf{C}_y$ is defined as:

$$\mathbf{C}_y = \begin{bmatrix} \mathbf{g}(z_s) & 0 & 0 \\ 0 & \mathbf{g}(z_s) & 0 \\ 0 & 0 & \mathbf{g}(z_s) \end{bmatrix}, \tag{D.2}$$

where

$$\mathbf{g}(z_s) = \exp\left\{ -\left(\frac{z - z_s}{\sigma_s} \right)^2 \right\}^T \mathbf{M} \tag{D.3}$$

is a Gaussian function, $z = [z_1, z_2 \cdots z_{N_{out}+1}]^T$ are Chebyshev grid points, z_s is the sensor location and σ_s defines the width of the Gaussian. We set $\sigma_s = 0.02$, which is sufficiently wide for the sensor to be independent of the output-grid resolution.

The actuator force is $\hat{\boldsymbol{f}}$, and it is applied at a single wall-normal location (z_a) via the matrix $\mathbf{B}_f$ (equation (6.12a)):

$$\mathbf{B}_f \hat{\boldsymbol{f}} = \mathbf{B} \begin{bmatrix} \mathbf{h}(z_a) & 0 & 0 \\ 0 & \mathbf{h}(z_a) & 0 \\ 0 & 0 & \mathbf{h}(z_a) \end{bmatrix} \begin{bmatrix} \hat{f}_x \\ \hat{f}_y \\ \hat{f}_z \end{bmatrix}, \tag{D.4}$$

where

$$\mathbf{h}(z_a) = \exp\left\{ -\left(\frac{z - z_a}{\sigma_a} \right)^2 \right\} \tag{D.5}$$

is a Gaussian function, $z = [z_1, z_2 \cdots z_{N_c+1}]^T$ are Chebyshev grid points and σ_a defines the width of the Gaussian. We set $\sigma_a = 0.02$, which is sufficiently wide to

be independent of the system-grid resolution.

D.3 Control

D.3.1 Control objective

The following cost function is derived from the control objective $\hat{\boldsymbol{z}}$ (equation (6.12b)) and is used for the $\mathcal{H}_2$-optimal control problems:

$$J = \mathbb{E}\left\{\lim_{t\to\infty}\frac{1}{T}\int_0^T\left(\int_0^h \hat{\boldsymbol{u}}(z,t)^*\hat{\boldsymbol{u}}(z,t)dz + \alpha^2\hat{\boldsymbol{f}}(t)^*\hat{\boldsymbol{f}}(t)\right)dt\right\}, \tag{D.6}$$

where

$$\begin{aligned}\int_0^h \hat{\boldsymbol{u}}(z,t)^*\hat{\boldsymbol{u}}(z,t)dz + \alpha^2\hat{\boldsymbol{f}}(t)^*\hat{\boldsymbol{f}}(t) &\equiv \left[\mathbf{M}^{1/2}\mathbf{C}\hat{\boldsymbol{q}}(t)\right]^*\left[\mathbf{M}^{1/2}\mathbf{C}\hat{\boldsymbol{q}}(t)\right] + \left[\alpha\hat{\boldsymbol{f}}(t)\right]^*\left[\alpha\hat{\boldsymbol{f}}(t)\right] \\ &\equiv \left[\hat{\boldsymbol{z}}(t)\right]^*\left[\hat{\boldsymbol{z}}(t)\right]. \end{aligned} \tag{D.7}$$

D.3.2 The estimator and controller gain matrices

The gain matrix $\mathbf{L}$ for FAC is designed by solving the following Ricatti equation:

$$\mathbf{A}\mathbf{Y} + \mathbf{Y}\mathbf{A}^* - \mathbf{Y}\mathbf{C}_m^*\mathbf{V}^{-1}\mathbf{C}_m\mathbf{Y} + \mathbf{B}_d\mathbf{B}_d^* = 0, \tag{D.8a}$$

$$\mathbf{L} = \mathbf{Y}\mathbf{C}_m^*\mathbf{V}^{-1}. \tag{D.8b}$$

The gain matrix $\mathbf{K}$ for FIC is designed by solving the following Ricatti equation:

$$\mathbf{A}^*\mathbf{X} + \mathbf{X}\mathbf{A} - \mathbf{X}\mathbf{B}_f\mathbf{R}^{-1}\mathbf{B}_f^*\mathbf{X} + \mathbf{C}_z^*\mathbf{C}_z = 0, \tag{D.9a}$$

$$\mathbf{K} = \mathbf{R}^{-1}\mathbf{B}_f^*\mathbf{X}, \tag{D.9b}$$

where $\mathbf{R} = \alpha^2\mathbf{I}$. The principle of separation for estimation and control states that the independently designed $\mathbf{L}$ and $\mathbf{K}$ are still optimal when combined (Kalman, 1960). Therefore, we do not have to find them again for IOC.

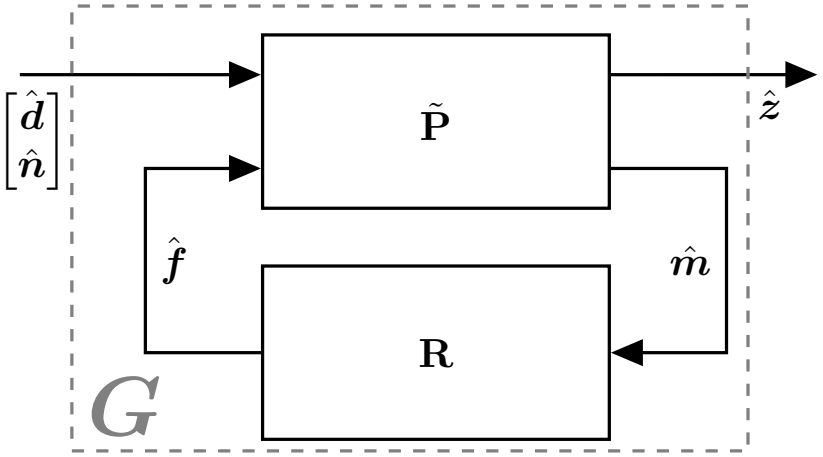

FIGURE D.1: Block diagram of $\mathbf{G}$.

flow $\boldsymbol{f}$ input / flow $\boldsymbol{m}$ output	single plane forcing at z_a	perfect forcing of the flow field
single plane measurement at z_s	*IOC*	*FAC*
perfect measurements of the flow field	*FIC*	*not considered*

FIGURE D.2: Inputs and outputs of the control problems.

D.3.3 State-space model

The FAC, FIC and IOC problems introduce a secondary system $\mathbf{R}$ to the flow $\tilde{\mathbf{P}}$ (figure D.1), where $\mathbf{R}$ is either an estimator, a controller or both (figure 6.2). To quantify the control performance of the three problems, we need to express the feedback interconnection of $\tilde{\mathbf{P}}$ and $\mathbf{R}$ as a single transfer function.

The measurement signal $\hat{\boldsymbol{m}}$ acts as an input and the force signal $\hat{\boldsymbol{f}}$ as an output to the secondary system:

$$\hat{\boldsymbol{f}}(t) = \mathbf{R}(t)\hat{\boldsymbol{m}}(t). \tag{D.10}$$

The signals $\hat{\boldsymbol{m}}$ and $\hat{\boldsymbol{f}}$ depend on the problem we consider (figure D.2). By substituting $\mathbf{R}\hat{\boldsymbol{m}}$ for $\hat{\boldsymbol{f}}$ in $\tilde{\mathbf{P}}$ (equation (6.12)), we can form the overall state-space model $\mathbf{G}$ (figure D.1), using a linear fractional transformation (LFT) (Aström and Murray, 2010):

$$\dot{\hat{\boldsymbol{x}}} = \mathbf{A}_L\hat{\boldsymbol{x}} + \mathbf{B}_L\hat{\boldsymbol{w}}, \tag{D.11a}$$

$$\hat{\boldsymbol{z}} = \mathbf{C}_L\hat{\boldsymbol{x}}, \tag{D.11b}$$

where $\mathbf{A}_L\hat{\boldsymbol{x}}$ describes the state dynamics, $\mathbf{B}_L\hat{\boldsymbol{w}}$ the input dynamics and $\mathbf{C}_L\hat{\boldsymbol{x}}$ the output dynamics of the LFT.

To form the LFT for FAC we ignore $\hat{\boldsymbol{f}}$ in $\tilde{\mathbf{P}}$ (equation (6.12)) and directly apply $\dot{\boldsymbol{q}}_e$ (equation (6.13b)) to $\dot{\boldsymbol{q}}$. The state-space model of $\mathbf{G}_{FAC}(t)$ is:

$$\dot{\hat{\boldsymbol{q}}} = (\mathbf{A} - \mathbf{L}\mathbf{C}_m)\,\hat{\boldsymbol{q}} + \begin{bmatrix} \mathbf{B}_d & -\mathbf{L}\mathbf{V}^{1/2} \end{bmatrix} \begin{bmatrix} \hat{\boldsymbol{d}} \\ \hat{\boldsymbol{n}} \end{bmatrix}, \tag{D.12}$$

$$\hat{\boldsymbol{z}} = \mathbf{C}_z\hat{\boldsymbol{q}}. \tag{D.13}$$

To form the LFT for FIC we ignore $\hat{\boldsymbol{m}}$ in $\tilde{\mathbf{P}}$ (equation (6.12)) and directly form $\hat{\mathbf{f}}$ from $\hat{\boldsymbol{q}}$ (equation (6.14)). The state-space model of $\mathbf{G}_{FIC}$ is:

$$\dot{\hat{\boldsymbol{q}}} = (\mathbf{A} - \mathbf{B}_f\mathbf{K})\,\hat{\boldsymbol{q}} + \mathbf{B}_d\hat{\boldsymbol{d}},$$

$$\hat{\boldsymbol{z}} = \begin{bmatrix} \mathbf{C}_z \\ -\mathbf{R}^{1/2}\mathbf{K} \end{bmatrix} \hat{\boldsymbol{q}}.$$

To form the LFT for IOC we combine $\mathbf{R}$ (equation (6.15)) with $\tilde{\mathbf{P}}$ (equation (6.12)). The state-space model of $\mathbf{G}_{IOC}$ is:

$$\begin{bmatrix} \dot{\hat{\boldsymbol{q}}} \\ \dot{\hat{\boldsymbol{q}}}_e \end{bmatrix} = \begin{bmatrix} \mathbf{A} & -\mathbf{B}_f\mathbf{F} \\ \mathbf{L}\mathbf{C}_m & \mathbf{A} - \mathbf{B}_f\mathbf{F} - \mathbf{L}\mathbf{C}_m \end{bmatrix} \begin{bmatrix} \hat{\boldsymbol{q}} \\ \hat{\boldsymbol{q}}_e \end{bmatrix} + \begin{bmatrix} \mathbf{B}_d & \mathbf{0} \\ \mathbf{0} & \mathbf{L}\mathbf{V}^{1/2} \end{bmatrix} \begin{bmatrix} \hat{\boldsymbol{d}} \\ \hat{\boldsymbol{n}} \end{bmatrix},$$

$$\hat{\boldsymbol{z}} = \begin{bmatrix} \mathbf{C}_z & \mathbf{0} \\ \mathbf{0} & -\mathbf{R}^{1/2}\mathbf{K} \end{bmatrix} \begin{bmatrix} \hat{\boldsymbol{q}} \\ \hat{\boldsymbol{q}}_e \end{bmatrix}.$$

D.3.4 $\mathcal{H}_2$-norms: Uncontrolled flow

The $\mathcal{H}_2$-norm for one channel half is

$$\|\hat{\boldsymbol{u}}\|_2 = \sqrt{\mathrm{tr}(\mathbf{C}_z\mathbf{Z}\mathbf{C}_z^*)}, \tag{D.14}$$

and at individual heights it is

$$\|\hat{\boldsymbol{u}}(z)\|_2 = \sqrt{\mathrm{diag}(\mathbf{C}\mathbf{Z}\mathbf{C}^*)}, \tag{D.15}$$

where $\mathbf{Z}$ is found by solving the following Lyapunov equation:

$$\mathbf{A}\mathbf{Z} + \mathbf{Z}\mathbf{A}^* = -\mathbf{B}_d\mathbf{B}_d^*. \tag{D.16}$$

D.3.5 $\mathcal{H}_2$-norms: Controlled flow

The $\mathcal{H}_2$-norms for one channel half are

$$\|\hat{\boldsymbol{z}}_{FAC}\|_2 = \sqrt{\mathrm{tr}(\mathbf{C}_z\mathbf{Y}\mathbf{C}_z^*)}, \tag{D.17}$$

$$\|\hat{\boldsymbol{z}}_{FI}\|_2 = \sqrt{\mathrm{tr}(\mathbf{B}_d^*\mathbf{X}\mathbf{B}_d)}, \tag{D.18}$$

$$\|\hat{\boldsymbol{z}}_{IO}\|_2 = \sqrt{\mathrm{tr}(\mathbf{C}_z\mathbf{Y}\mathbf{C}_z^*) + \mathrm{tr}(\mathbf{C}_m\mathbf{Y}\mathbf{X}\mathbf{L})} = \sqrt{\mathrm{tr}(\mathbf{B}_d^*\mathbf{X}\mathbf{B}_d) + \mathrm{tr}(\mathbf{K}\mathbf{Y}\mathbf{X}\mathbf{B}_f)}. \tag{D.19}$$

The $\mathcal{H}_2$-norms at individual wall heights are

$$\|\hat{\boldsymbol{z}}_{FA}(z)\|_2 = \sqrt{\mathrm{diag}(\mathbf{C}\mathbf{W}_c\mathbf{C}^*)} = \sqrt{\mathrm{diag}(\mathbf{C}\mathbf{Y}\mathbf{C}^*)}, \tag{D.20}$$

$$\|\hat{\boldsymbol{z}}_{FI}(z)\|_2 = \sqrt{\mathrm{diag}\left(\begin{bmatrix}\mathbf{C}\\ \mathbf{0}\end{bmatrix}\mathbf{W}_c\begin{bmatrix}\mathbf{C}\\ \mathbf{0}\end{bmatrix}^*\right)}, \tag{D.21}$$

$$\|\hat{\boldsymbol{z}}_{IO}(z)\|_2 = \sqrt{\mathrm{diag}\left(\begin{bmatrix}\mathbf{C} & \mathbf{0}\\ \mathbf{0} & \mathbf{0}\end{bmatrix}\mathbf{W}_c\begin{bmatrix}\mathbf{C} & \mathbf{0}\\ \mathbf{0} & \mathbf{0}\end{bmatrix}^*\right)}, \tag{D.22}$$

where $\mathbf{W}_c$ is the controllability Gramian that is found by solving the following Lyapunov equation (based on the LFT):

$$\mathbf{A}_L\mathbf{W}_c + \mathbf{W}_c\mathbf{A}_L^* = -\mathbf{B}_L\mathbf{B}_L^*. \tag{D.23}$$

D.3.6 $\mathcal{H}_2$-norms: Actuation force

The $\mathcal{H}_2$-norms for the actuator forces are

$$\|\hat{\boldsymbol{f}}_{FA}\|_2 = \sqrt{\mathrm{tr}((\mathbf{C}_z\mathbf{L}\mathbf{C}_m)\mathbf{W}_c(\mathbf{C}_z\mathbf{L}\mathbf{C}_m)^*)} = \sqrt{\mathrm{tr}((\mathbf{C}_z\mathbf{L}\mathbf{C}_m)\mathbf{Y}(\mathbf{C}_z\mathbf{L}\mathbf{C}_m)^*)}, \quad \text{(D.24)}$$

$$\|\hat{\boldsymbol{f}}_{FI}(z)\|_2 = \sqrt{\mathrm{tr}\left(\begin{bmatrix}\mathbf{0}\\ \mathbf{R}^{1/2}\mathbf{K}\end{bmatrix}\mathbf{W}_c\begin{bmatrix}\mathbf{0}\\ \mathbf{R}^{1/2}\mathbf{K}\end{bmatrix}^*\right)}, \quad \text{(D.25)}$$

$$\|\hat{\boldsymbol{f}}_{IO}(z)\|_2 = \sqrt{\mathrm{tr}\left(\begin{bmatrix}\mathbf{0} & \mathbf{0}\\ \mathbf{0} & \mathbf{R}^{1/2}\mathbf{K}\end{bmatrix}\mathbf{W}_c\begin{bmatrix}\mathbf{0} & \mathbf{0}\\ \mathbf{0} & \mathbf{R}^{1/2}\mathbf{K}\end{bmatrix}^*\right)}. \quad \text{(D.26)}$$

Bibliography

Abbassi, M. R., Baars, W. J., Hutchins, N. and Marusic, I. (2017), 'Skin-friction drag reduction in a high-Reynolds-number turbulent boundary layer via real-time control of large-scale structures', *Int. J. Heat Fluid Flow* **67**, 30–41.

Abe, H., Kawamura, H. and Choi, H. (2004), 'Very large-scale structures and their effects on the wall shear-stress fluctuations in a turbulent channel flow up to Re_τ= 640', *J. Fluids Eng.* **126**(5), 835–843.

Adrian, R. J., Meinhart, C. D. and Tomkins, C. D. (2000), 'Vortex organization in the outer region of the turbulent boundary layer', *J. Fluid Mech.* **422**, 1–54.

Åkervik, E., Hœpffner, J., Ehrenstein, U. and Henningson, D. S. (2007), 'Optimal growth, model reduction and control in a separated boundary-layer flow using global eigenmodes', *J. Fluid Mech.* **579**, 305–314.

Akhtar, I., Borggaard, J., Burns, J. A., Imtiaz, H. and Zietsman, L. (2015), 'Using functional gains for effective sensor location in flow control: a reduced-order modelling approach', *J. Fluid Mech.* **781**, 622–656.

Antonia, R. A., Zhu, Y. and Sokolov, M. (1995), 'Effect of concentrated wall suction on a turbulent boundary layer', *Phys. Fluids* **7**(10), 2465–2474.

Aström, K. J. and Murray, R. M. (2010), *Feedback systems: an introduction for scientists and engineers*, Princeton University Press.

Baars, W. J., Hutchins, N. and Marusic, I. (2016), 'Spectral stochastic estimation of high-Reynolds-number wall-bounded turbulence for a refined inner-outer interaction model', *Phys. Rev. Fluids* **1**(5), 054406.

Bagheri, S. and Henningson, D. S. (2011), 'Transition delay using control theory', *Philos. Trans. Royal Soc. A* **369**(1940), 1365–1381.

Bagheri, S., Henningson, D. S., Hœpffner, J. and Schmid, P. J. (2009), 'Input-output analysis and control design applied to a linear model of spatially developing flows', *Appl. Mech. Rev.* **62**(2), 020803.

Bai, H. L., Zhou, Y., Zhang, W. G., Xu, S. J., Wang, Y. and Antonia, R. A. (2014), 'Active control of a turbulent boundary layer based on local surface perturbation', *J. Fluid Mech.* **750**, 316–354.

Balakumar, B. J. and Adrian, R. J. (2007), 'Large-and very-large-scale motions in channel and boundary-layer flows', *Philos. Trans. Royal Soc. A* **365**(1852), 665–681.

Belson, B. A. (2014), Control of the Transitional Boundary Layer, PhD thesis, Princeton University.

Belson, B. A., Semeraro, O., Rowley, C. W. and Henningson, D. S. (2013), 'Feedback control of instabilities in the two-dimensional Blasius boundary layer: the role of sensors and actuators', *Phys. Fluids* **25**(5), 054106.

Bensoussan, A. (1972), Optimization of sensors' location in a distributed filtering problem, *in* 'Stability of Stochastic Dynamical Systems', Springer, pp. 62–84.

Berger, E. (1967), 'Suppression of vortex shedding and turbulence behind oscillating cylinders', *Phys. Fluids* **10**(9), S191–S193.

Berrut, J. P. and Trefethen, L. N. (2004), 'Barycentric Lagrange Interpolation', *SIAM Rev.* **46**(3), 501–517.

Betchov, R. and Criminale, W. O. (1966), 'Spatial instability of the inviscid jet and wake', *Phys. Fluids* **9**(2), 359–362.

Bewley, T. R. (2001), 'Flow control: new challenges for a new renaissance', *Prog. Aerosp. Sci.* **37**(1), 21–58.

Bewley, T. R. and Liu, S. (1998), 'Optimal and robust control and estimation of linear paths to transition', *J. Fluid Mech.* **365**, 305–349.

Bewley, T. R., Moin, P. and Temam, R. (2001), 'DNS-based predictive control of turbulence: an optimal benchmark for feedback algorithms', *J. Fluid Mech.* **447**, 179–225.

Bewley, T. R. and Protas, B. (2004), 'Skin friction and pressure: The "footprints" of turbulence', *Phys. D Nonlinear Phenom.* **196**(1-2), 28–44.

Brunton, S. L. and Noack, B. R. (2015), 'Closed-loop turbulence control: progress and challenges', *Appl. Mech. Rev* **67**(5), 050801.

Burns, J. A. and King, B. B. (1994), Optimal sensor location for robust control of distributed parameter systems, *in* 'Proc. 33rd IEEE Conf. Decision Control', IEEE, pp. 3967–3972.

Cantwell, B. J. (1981), 'Organized motion in turbulent flow', *Ann. Rev. Fluid Mech.* **13**(1), 457–515.

Cattafesta III, L. N. and Sheplak, M. (2011), 'Actuators for active flow control', *Ann. Rev. Fluid Mech.* **43**, 247–272.

Cess, R. D. (1958), *A survey of the literature on heat transfer in turbulent tube flow*, Westinghouse Research.

Chang, Y., Collis, S. S. and Ramakrishnan, S. (2002), 'Viscous effects in control of near-wall turbulence', *Phys. Fluids* **14**(11), 4069–4080.

Chen, K. K. and Rowley, C. W. (2011), 'H_2 optimal actuator and sensor placement in the linearised complex Ginzburg-Landau system', *J. Fluid Mech.* **681**, 241–260.

Chen, K. K. and Rowley, C. W. (2014), Fluid flow control applications of H_2 optimal actuator and sensor placement, *in* 'American Control Conference (ACC)', IEEE, pp. 4044–4049.

Chen, K. K. and Rowley, C. W. (2015), Heuristics for effective actuator and sensor placement in feedback flow control, *in* 'Active Flow and Combustion Control 2014', Springer, pp. 115–129.

Chen, W. H. and Seinfeld, J. H. (1975), 'Optimal location of process measurements', *Int. J. Control* **21**(6), 1003–1014.

Chevalier, M., Hoepffner, J., Bewley, T. R. and Henningson, D. S. (2006), 'State estimation in wall-bounded flow systems. Part 2. Turbulent flows', *J. Fluid Mech.* **552**, 167–187.

Choi, H., Jeon, W. and Kim, J. (2008), 'Control of flow over a bluff body', *Annu. Rev. Fluid Mech.* **40**, 113–139.

Chomaz, J. M. (2005), 'Global instabilities in spatially developing flows: non-normality and nonlinearity', *Annu. Rev. Fluid Mech.* **37**, 357–392.

Chomaz, J. M., Huerre, P. and Redekopp, L. (1987), Models of hydrodynamic resonances in separated shear flows, *in* 'Proc. 6th Symp. on Turbulent Shear Flows, Toulouse', ADS, pp. 321–326.

Chomaz, J. M., Huerre, P. and Redekopp, L. G. (1988), 'Bifurcations to local and global modes in spatially developing flows', *Phys. Rev. Lett.* **60**(1), 25.

Chomaz, J. M., Huerre, P. and Redekopp, L. G. (1990), The effect of nonlinearity and forcing on global modes, *in* 'New trends in nonlinear dynamics and pattern-forming phenomena', Springer, pp. 259–274.

Chomaz, J. M., Huerre, P. and Redekopp, L. G. (1991), 'A frequency selection criterion in spatially developing flows', *Stud. App. Maths* **84**(2), 119–144.

Cohen, K., Siegel, S., McLaughlin, T., Gillies, E. and Myatt, J. (2005), 'Closed-loop approaches to control of a wake flow modeled by the Ginzburg-Landau equation', *Comput. Fluids* **34**(8), 927–949.

Cohen, K., Siegel, S., McLaughlin, T. and Myatt, J. (2003), Fuzzy logic control of a circular cylinder vortex shedding model, *in* '41st Aerospace Sciences Meeting and Exhibit', p. 1290.

Colburn, C. H. (2011), Estimation techniques for large-scale turbulent fluid systems, PhD thesis, University of California, San Diego.

Cortelezzi, L., Speyer, J. L., Lee, K. H. and Kim, J. (1998*a*), Robust reduced-order control of turbulent channel flows via distributed sensors and actuators, *in* 'Proc. 37th IEEE Conf. Decis. Control', Vol. 2, IEEE, pp. 1906–1911.

Cortelezzi, L., Speyer, J. L., Lee, K. H. and Kim, J. (1998*b*), 'Skin-friction drag reduction via robust reduced-order linear feedback control', *Int. J. Comput. Fluid D.* **11**(1-2), 79–92.

Cossu, C. and Chomaz, J. M. (1997), 'Global measures of local convective instabilities', *Phys. Rev. Lett.* **78**(23), 4387.

da Silva, A. F. C. and Colonius, T. (2018), 'Ensemble-based state estimator for aerodynamic flows', *AIAA J.* **56**(7), 2568–2578.

del Alamo, J. C. and Jiménez, J. (2006), 'Linear energy amplification in turbulent channels', *J. Fluid Mech.* **559**, 205–213.

Doyle, J. C., Francis, B. A. and Tannenbaum, A. R. (2013), *Feedback control theory*, Courier Corporation.

Duvvuri, S. and McKeon, B. J. (2015), 'Triadic scale interactions in a turbulent boundary layer', *J. Fluid Mech.* **767, R4**.

Encinar, M. P., Vela-Martín, A., García-Gutiérrez, A. and Jiménez, J. (2018), 'A second-order consistent, low-storage method for time-resolved channel flow simulations', *arXiv preprint: flu-dyn/1808.06461* pp. 1–14.

Evensen, G. (2009), *Data assimilation: the ensemble Kalman filter*, Springer Science & Business Media.

Farrell, B. F. and Ioannou, P. J. (1993), 'Stocastic forcing of the linearized Navier-Stokes equations', *Phys. Fluids* **5**(11), 2600–2609.

Farrell, B. F. and Ioannou, P. J. (1996), 'Generalized stability theory. Part I: Autonomous operators', *J. Atmos. Sci.* **53**(14), 2025–2040.

Fowler, A. (2012), 'Data assimilation tutorial on the Kalman filter.'.

Gad-el-Hak, M. (1996), 'Modern developments in flow control', *Appl. Mech. Rev.* **49**(7).

Gad-el Hak, M. (2001), 'Flow control: t he future', *J. Aircraft* **38**(3), 402–418.

Gad-el Hak, M. (2006), *Flow control: passive, active, and reactive flow management*, Cambridge University Press.

Gad-el Hak, M. and Bandyopadhyay, P. R. (1994), 'Reynolds number effects in wall-bounded turbulent flows', *App. Mech. Rev.* **47**(8), 307–365.

Gad-el-Hak, M., Pollard, A. and Bonnet, J. (2003), *Flow control: fundamentals and practices*, Springer Science & Business Media.

García-Mayoral, R. and Jiménez, J. (2011), 'Drag reduction by riblets', *Philos. Trans. Royal Soc. A* **369**(1940), 1412–1427.

Gatti, D. and Quadrio, M. (2013), 'Performance losses of drag-reducing spanwise forcing at moderate values of the Reynolds number', *Phys. Fluids* **25**(12), 125109.

Giannetti, F. and Luchini, P. (2007), 'Structural sensitivity of the first instability of the cylinder wake', *J. Fluid Mech.* **581**, 167–197.

Gillies, E. A. (1998), 'Low-dimensional control of the circular cylinder wake', *J. Fluid Mech.* **371**, 157–178.

Gillies, E. A. (2001), 'Multiple sensor control of vortex shedding', *AIAA J.* **39**(4), 748–750.

Gouder, K., Potter, M. and Morrison, J. F. (2013), 'Turbulent friction drag reduction using electroactive polymer and electromagnetically driven surfaces', *Exp. Fluids* **54**(1), 1441.

Guala, M., Hommema, S. E. and Adrian, R. J. (2006), 'Large-scale and very-large-scale motions in turbulent pipe flow', *J. Fluid Mech.* **554**, 521–542.

Gustavsson, L. H. (1991), 'Energy growth of three-dimensional disturbances in plane Poiseuille flow', *J. Fluid Mech.* **224**, 241–260.

Hamilton, J. M., Kim, J. and Waleffe, F. (1995), 'Regeneration mechanisms of near-wall turbulence structures', *J. Fluid Mech.* **287**, 317–348.

Hammond, E. P., Bewley, T. R. and Moin, P. (1998), 'Observed mechanisms for turbulence attenuation and enhancement in opposition-controlled wall-bounded flows', *Phys. Fluids* **10**(9), 2421–2423.

Head, M. R. and Bandyopadhyay, P. (1981), 'New aspects of turbulent boundary-layer structure', *J. Fluid Mech.* **107**, 297–338.

Henningson, D. S. and Reddy, S. C. (1994), 'On the role of linear mechanisms in transition to turbulence', *Phys. Fluids* **6**(3), 1396–1398.

Herculano-Houzel, S. (2009), 'The human brain in numbers: a linearly scaled-up primate brain', *Front. hum. neurosci.* **3**, 31.

Hiramoto, K., Doki, H. and Obinata, G. (2000), 'Optimal sensor/actuator placement for active vibration control using explicit solution of Algebraic Riccati Equation', *J. Sound Vib.* **229**(5), 1057–1075.

Hoepffner, J. (2007), 'Implementation of boundary conditions'.

Hœpffner, J., Chevalier, M., Bewley, T. R. and Henningson, D. S. (2005), 'State estimation in wall-bounded flow systems. Part 1. perturbed laminar flows', *J. Fluid Mech.* **534**, 263–294.

Högberg, M. and Bewley, T. R. (2000), Spatially localized convolution kernels for feedback control of transitional flows, *in* 'Proc. 39th IEEE Conf. Decision Control', Vol. 4, IEEE, pp. 3278–3283.

Högberg, M., Bewley, T. R. and Henningson, D. S. (2003*a*), 'Linear feedback control and estimation of transition in plane channel flow', *J. Fluid Mech.* **481**, 149–175.

Högberg, M., Bewley, T. R. and Henningson, D. S. (2003*b*), 'Relaminarization of $\mathrm{Re}_\tau = 100$ turbulence using gain scheduling and linear state-feedback control', *Phys. Fluids* **15**(11), 3572–3575.

Hoyas, S. and Jiménez, J. (2006), 'Scaling of the velocity fluctuations in turbulent channels up to $\mathrm{Re}_\tau = 2003$', *Phys. Fluids* **18**(1), 1–4.

Hu, W., Morris, K. and Zhang, Y. (2016), Sensor location in a controlled thermal fluid, *in* '55th Conf. on Decision and Control (CDC)', IEEE, pp. 2259–2264.

Huerre, P. and Monkewitz, P. A. (1990), 'Local and global instabilities in spatially developing flows', **22**, 473–537.

Hurst, E., Yang, Q. and Chung, Y. M. (2014), 'The effect of Reynolds number on turbulent drag reduction by streamwise travelling waves', *J. Fluid Mech.* **759**, 28–55.

Hutchins, N. and Marusic, I. (2007*a*), 'Evidence of very long meandering features in the logarithmic region of turbulent boundary layers', *J. Fluid Mech.* **579**, 1–28.

Hutchins, N. and Marusic, I. (2007*b*), 'Large-scale influences in near-wall turbulence', *Philos. Trans. Royal Soc. A* **365**(1852), 647–664.

Hwang, Y. and Cossu, C. (2010*a*), 'Amplification of coherent streaks in the turbulent Couette flow: an input–output analysis at low Reynolds number', *J. Fluid Mech.* **643**, 333–348.

Hwang, Y. and Cossu, C. (2010*b*), 'Linear non-normal energy amplification of harmonic and stochastic forcing in the turbulent channel flow', *J. Fluid Mech.* **664**, 51–73.

Hwang, Y. and Cossu, C. (2010*c*), 'Self-sustained process at large scales in turbulent channel flow', *Phys. Rev. Lett.* **105**(4), 044505.

Illingworth, S. J. (2014), Estimation and control of vortex shedding at low Reynolds numbers, *in* '19th Australasian Fluid Mechanics Conference', AFMS.

Illingworth, S. J. (2015), Dynamic estimation of vortex shedding, *in* 'Tenth Intl. Symp. on Turbulence and Shear Flow Phenomena', TSFP9.

Illingworth, S. J. (2016), 'Model-based control of vortex shedding at low Reynolds numbers', *Theor. Comput. Fluid Dyn.* **30**(5), 429–448.

Illingworth, S. J., Monty, J. P. and Marusic, I. (2018), 'Estimating large-scale structures in wall turbulence using linear models', *J. Fluid Mech.* **842**, 146–162.

Illingworth, S. J., Morgans, A. S. and Rowley, C. W. (2012), 'Feedback control of cavity flow oscillations using simple linear models', *J. Fluid Mech.* **709**, 223–248.

Iwamoto, K., Suzuki, Y. and Kasagi, N. (2002), 'Reynolds number effect on wall turbulence: toward effective feedback control', *Int. J. Heat Fluid Flow* **23**(5), 678–689.

Jiménez, J. (2012), 'Cascades in wall-bounded turbulence', *Ann. Rev. Fluid Mech.* **44**, 27–45.

Jiménez, J. and Moin, P. (1991), 'The minimal flow unit in near-wall turbulence', *J. Fluid Mech.* **225**, 213–240.

Jin, B., Sandberg, R. D. and Illingworth, S. (2018), Resolvent-based feedback control of vortex shedding at low reynolds numbers, *in* '21st Australasian Fluid Mechanics Conference', AFMS.

Jones, B. L., Heins, P. H., Kerrigan, E. C., Morrison, J. F. and Sharma, A. S. (2015), 'Modelling for robust feedback control of fluid flows', *J. Fluid Mech.* **769**, 687–722.

Jones, B. L., Kerrigan, E. C., Morrison, J. F. and Zaki, T. A. (2011), 'Flow estimation of boundary layers using DNS-based wall shear information', *Int. J. Control* **84**(8), 1310–1325.

Joshi, S. S., Speyer, J. L. and Kim, J. (1997), 'A systems theory approach to the feedback stabilization of infinitesimal and finite-amplitude disturbances in plane Poiseuille flow', *J. Fluid Mech.* **332**, 157–184.

Jovanović, M. R. and Bamieh, B. (2001), The spatio-temporal impulse response of the linearized Navier-Stokes equations, *in* 'Am. Control Conf.', pp. 1948–1953.

Jovanović, M. R. and Bamieh, B. (2005), 'Componentwise energy amplification in channel flows', *J. Fluid Mech.* **534**, 145–183.

Juillet, F., McKeon, B. J. and Schmid, P. J. (2014), 'Experimental control of natural perturbations in channel flow', *J. Fluid Mech.* **752**, 296–309.

Juillet, F., Schmid, P. J. and Huerre, P. (2013), 'Control of amplifier flows using subspace identification techniques', *J. Fluid Mech.* **725**, 522–565.

Kalman, R. E. (1960), 'Contributions to the theory of optimal control', *Bol. soc. mat. mexicana* **5**(2), 102–119.

Karniadakis, G. E. and Choi, K. (2003), 'Mechanisms on transverse motions in turbulent wall flows', *Ann. Rev. Fluid Mech.* **35**(1), 45–62.

Kasagi, N., Hasegawa, Y. and Fukagata, K. (2009), Toward cost-effective control of wall turbulence for skin friction drag reduction, *in* 'Advances in turbulence XII', Springer, pp. 189–200.

Kasinathan, D. and Morris, K. (2013), '$\mathscr{H}_\infty$-optimal actuator location', *IEEE Trans. Autom. Control.* **58**(10), 2522–2535.

Khan, T., Morris, K. and Stastna, M. (2015), Computation of the optimal sensor location for the estimation of an 1-D linear dispersive wave equation, *in* 'American Control Conference (ACC), 2015', IEEE, pp. 5270–5275.

Kim, J. (2003), 'Control of turbulent boundary layers', *Phys. Fluids* **15**(5), 1093–1105.

Kim, J. (2011), 'Physics and control of wall turbulence for drag reduction', *Philos. Trans. Royal Soc. A* **369**(1940), 1396–1411.

Kim, J. and Bewley, T. R. (2007), 'A linear systems approach to flow control', *Annu. Rev. Fluid Mech.* **39**(1), 383–417.

Kim, J. and Lim, J. (2000), 'A linear process in wall-bounded turbulent shear flows', *Phys. Fluids* **12**(8), 1885–1888.

Komminaho, J., Lundbladh, A. and Johansson, A. V. (1996), 'Very large structures in plane turbulent couette flow', *J. Fluid Mech.* **320**, 259–285.

Koumoutsakos, P. (1999), 'Vorticity flux control for a turbulent channel flow', *Phys. Fluids* **11**(2), 248–250.

Kumar, S. and Seinfeld, J. (1978), 'Optimal location of measurements for distributed parameter estimation', *IEEE Trans. Autom. Control.* **23**(4), 690–698.

Lang, A. W., Motta, P., Hidalgo, P. and Westcott, M. (2008), 'Bristled shark skin: a microgeometry for boundary layer control?', *Bioinspiration Biomim.* **3**(4), 046005.

Lauga, E. and Bewley, T. R. (2003), 'The decay of stabilizability with Reynolds number in a linear model of spatially developing flows', *Proc. Royal Soc. A: Mathematical, Physical and Engineering Sciences* **459**(2036), 2077–2095.

Lauga, E. and Bewley, T. R. (2004), 'Performance of a linear robust control strategy on a nonlinear model of spatially developing flows', *J. Fluid Mech.* **512**, 343–374.

Liepmann, H. W. and Nosenchuck, D. M. (1982), 'Active control of laminar-turbulent transition', *J. Fluid Mech.* **118**, 201–204.

Litrico, X. and Georges, D. (1999), 'Robust continuous-time and discrete-time flow control of a dam–river system. (ii) controller design', *Appl. Math. Model.* **23**(11), 829–846.

Luhar, M., Sharma, A. S. and McKeon, B. J. (2014), 'Opposition control within the resolvent analysis framework', *J. Fluid Mech.* **749**, 597–626.

Luhar, M., Sharma, A. S. and McKeon, B. J. (2015), 'A framework for studying the effect of compliant surfaces on wall turbulence', *J. Fluid Mech* **768**, 415–441.

Lumley, J. L. (1973), 'Drag reduction in turbulent flow by polymer additives', *J. Polym. Sci: Macromol. Rev.* **7**(1), 263–290.

Madhusudanan, A., Illingworth, S. J. and Marusic, I. (2019), 'Coherent large-scale structures from the linearized Navier-Stokes equations', *J. Fluid Mech.* **873**, 89–109.

Malkus, W. V. R. (1956), 'Outline of a theory of turbulent shear flow', *J. Fluid Mech.* **1**(5), 521–539.

Marusic, I., Mathis, R. and Hutchins, N. (2010*a*), 'High Reynolds number effects in wall turbulence', *Int. J. Heat Fluid Fl.* **3**(31), 418–428.

Marusic, I., Mathis, R. and Hutchins, N. (2010*b*), 'Predictive model for wall-bounded turbulent flow', *Science* **329**(5988), 193–196.

Mathis, R., Hutchins, N. and Marusic, I. (2009), 'Large-scale amplitude modulation of the small-scale structures in turbulent boundary layers', *J. Fluid Mech.* **628**, 311–337.

McKeon, B. J. and Sharma, A. S. (2010), 'A critical-layer framework for turbulent pipe flow', *J. Fluid Mech.* **658**, 336–382.

McKeon, B. J., Sharma, A. S. and Jacobi, I. (2013), 'Experimental manipulation of wall turbulence: A systems approach', *Phys. Fluids* **25**(3), 031301.

McKernan, J., Whidborne, J. F. and Papadakis, G. (2007), 'Linear quadratic control of plane Poiseuille flow–the transient behaviour', *Int. J. Control* **80**(12), 1912–1930.

Moarref, R. and Jovanović, M. R. (2012), 'Model-based design of transverse wall oscillations for turbulent drag reduction', *J. Fluid Mech.* **707**, 205–240.

Moarref, R., Jovanović, M. R., Tropp, J. A., Sharma, A. S. and McKeon, B. J. (2014), 'A low-order decomposition of turbulent channel flow via resolvent analysis and convex optimization', *Phys. Fluids* **26**(5), 051701.

Moarref, R., Sharma, A. S., Tropp, J. A. and McKeon, B. J. (2013), 'Model-based scaling of the streamwise energy density in high-Reynolds-number turbulent channels', *J. Fluid Mech.* **734**, 275–316.

Moin, P. and Bewley, T. (1994), 'Feedback control of turbulence', *Appl. Mech. Rev.* **47**(6S), S3–S13.

Monkewitz, P. (1989), Feedback control of global oscillations in fluid systems, *in* '2nd Shear Flow Conference', p. 991.

Mons, V., Chassaing, J. and Sagaut, P. (2017), 'Optimal sensor placement for variational data assimilation of unsteady flows past a rotationally oscillating cylinder', *J. Fluid Mech.* **823**, 230–277.

Monty, J. P., Stewart, J. A., Williams, R. C. and Chong, M. S. (2007), 'Large-scale features in turbulent pipe and channel flows', *J. Fluid Mech.* **589**, 147–156.

Morris, K. (2011), 'Linear-quadratic optimal actuator location', *IEEE Trans. Autom. Control.* **56**(1), 113–124.

Naguib, A. M., Morrison, J. F. and Zaki, T. A. (2010), 'On the relationship between the wall-shear-stress and transient-growth disturbances in a laminar boundary layer', *Phys. Fluids* **22**(5), 054103.

Natarajan, M., Freund, J. B. and Bodony, D. J. (2016), 'Actuator selection and placement for localized feedback flow control', *J. Fluid Mech.* **809**, 775–792.

Noack, B. R., Morzynski, M. and Tadmor, G. (2011), *Reduced-order modelling for flow control*, Springer Science & Business Media.

Oehler, S. F. and Illingworth, S. (2018c), Linear estimation and control of coherent structures in wall-bounded turbulence at Reτ= 2000, *in* '21st Australasian Fluid Mechanics Conference', AFMS.

Oehler, S. F. and Illingworth, S. J. (2018a), 'Sensor and actuator placement trade-offs for a linear model of spatially developing flows', *J. Fluid Mech.* **854**, 34–55.

Oehler, S., Garcia-Gutiérrez, A. and Illingworth, S. (2018b), 'Linear estimation of coherent structures in wall-bounded turbulence at $\mathrm{Re}_\tau = 2000$', *J. Phys. Conf. Ser.* **1001**, 012006.

Oehler, S., Ooi, A. and Illingworth, S. J. (2016), Actuator and sensor selection for feedback control of the linearised Ginzburg-Landau equation, *in* '20th Australasian Fluid Mechanics Conference', AFMS.

Park, D. S., Ladd, D. and Hendricks, E. W. (1994), 'Feedback control of von Kármán vortex shedding behind a circular cylinder at low Reynolds numbers', *Phys. Fluids* **6**(7), 2390–2405.

Park, D. S., Ladd, D. M. and Hendricks, E. W. (1993), 'Feedback control of a global mode in spatially developing flows', *Phys. Lett. A* **182**(2-3), 244–248.

Pope, S. B. (2000), *Turbulent flows*, Cambridge University Press.

Prandtl, L. (1904), 'Über Flussigkeitsbewegung bei sehr kleiner Reibung', *Verhandl. III, Internat. Math.-Kong., Heidelberg, Teubner, Leipzig, 1904* pp. 484–491.

Pujals, G., García-Villalba, M., Cossu, C. and Depardon, S. (2009), 'A note on optimal transient growth in turbulent channel flows', *Phys. Fluids* **21**(1), 015109.

Rathnasingham, R. and Breuer, K. S. (1997), 'System identification and control of a turbulent boundary layer', *Phys. Fluids* **9**(7), 1867–1869.

Rathnasingham, R. and Breuer, K. S. (2003), 'Active control of turbulent boundary layers', *J. Fluid Mech.* **495**, 209–233.

Reddy, S. C., Schmid, P. J. and Henningson, D. S. (1993), 'Pseudospectra of the orr–sommerfeld operator', *SIAM J. Appl. Math.* **53**(1), 15–47.

Reinschke, J. (1999), $\mathcal{H}_\infty$-control of spatially distributed systems., PhD thesis, University of Cambridge.

Reinschke, J. and Smith, M. C. (2003), 'Designing robustly stabilising controllers for lti spatially distributed systems using coprime factor synthesis', *Automatica* **39**(2), 193–203.

Reynolds, W. C. and Hussain, A. K. M. F. (1972), 'The mechanics of an organized wave in turbulent shear flow. Part 3. Theoretical models and comparisons with experiments', *J. Fluid Mech.* **54**, 263–288.

Reynolds, W. C. and Tiederman, W. G. (1967), 'Stability of turbulent channel flow, with application to Malkus's theory', *J. Fluid Mech.* **27**(1967), 253–272.

Robinson, S. K. (1991), 'The kinematics of turbulent boundary layer structure', *NASA STI/Recon Technical Report N* **91**.

Roussopoulos, K. (1993), 'Feedback control of vortex shedding at low Reynolds numbers', *J. Fluid Mech.* **248**(1993), 267–296.

Rowley, C. W. and Juttijudata, V. (2005), Model-based control and estimation of cavity flow oscillations, *in* '44th IEEE Conference on Decision and Control, and the European Control Conference 2005', IEEE, pp. 512–517.

Sadayoshi, T. and Tomoaki, I. (2005), 'Interaction between a large-scale structure and near-wall structures in channel flow', *J. Fluid Mech.* **524**, 249–262.

Sasaki, K., Vinuesa, R., Cavalieri, A. V. G., Schlatter, P. and Henningson, D. S. (2019), 'Transfer functions for flow predictions in wall-bounded turbulence', *J. Fluid Mech.* **864**, 708–745.

Schmid, P. J. (2007), 'Nonmodal Stability Theory', *Annu. Rev. Fluid Mech* **39**, 129–62.

Schmid, P. J. and Brandt, L. (2014), 'Analysis of fluid systems: stability, receptivity, sensitivity lecture notes from the FLOW-NORDITA summer school on advanced instability methods for complex flows, Stockholm, Sweden, 2013', *Appl. Mech. Rev.* **66**(2), 024803.

Schmid, P. J. and Henningson, D. S. (2012), *Stability and transition in shear flows*, Springer Science & Business Media.

Schoppa, W. and Hussain, F. (2002), 'Coherent structure generation in near-wall turbulence', *J. Fluid Mech.* **453**, 57–108.

Semeraro, O., Bagheri, S., Brandt, L. and Henningson, D. S. (2013), 'Transition delay in a boundary layer flow using active control', *J. Fluid Mech.* **731**, 288–311.

Seron, M. M., Braslavsky, J. H. and Goodwin, G. C. (1997), *Fundamental Limitations in Filtering and Control*, Springer.

Sharma, A. S., Morrison, J. F., McKeon, B. J., Limebeer, D. J. N., Koberg, W. H. and Sherwin, S. J. (2011), 'Relaminarisation of $\mathrm{Re}_\tau = 100$ channel flow with globally stabilising linear feedback control', *Phys. Fluids* **23**(12), 125105.

Skogestad, S. and Postlethwaite, I. (2007), *Multivariable feedback control: analysis and design*, Wiley New York.

Smits, A. J., McKeon, B. J. and Marusic, I. (2011), 'High–Reynolds number wall turbulence', *Ann. Rev. Fluid Mech.* **43**.

Son, D., Jeon, S. and Choi, H. (2011), 'A proportional–integral–differential control of flow over a circular cylinder', *Philos. Trans. Royal Soc. A* **369**(1940), 1540–1555.

Stein, G. (2003), 'Respect the unstable', *IEEE Control Systems Magazine* **23**(4), 12–25.

Stroh, A., Frohnapfel, B., Schlatter, P. and Hasegawa, Y. (2015), 'A comparison of opposition control in turbulent boundary layer and turbulent channel flow', *Phys. Fluids* **27**(7), 075101.

Taira, K., Brunton, S. L., Dawson, S. T. M., Rowley, C. W., Colonius, T., McKeon, B. J., Schmidt, O. T., Gordeyev, S., Theofilis, V. and Ukeiley, L. S. (2017), 'Modal analysis of fluid flows: An overview', *AIAA J.* pp. 1–29.

Tomkins, C. D. and Adrian, R. J. (2005), 'Energetic spanwise modes in the logarithmic layer of a turbulent boundary layer', *J. Fluid Mech.* **545**, 141–162.

Trefethen, L. N. (2000), *Spectral methods in MATLAB*, Society for Industrial and Applied Mathematics.

Trefethen, L. N., Trefethen, A. E., Reddy, S. C. and Driscoll, T. A. (1993), 'Hydrodynamic stability without eigenvalues', *Science* **261**(5121), 578–584.

Walsh, M. J. (1983), 'Riblets as a viscous drag reduction technique', *AIAA J.* **21**(4), 485–486.

Wehrmann, O. H. (1965), 'Reduction of velocity fluctuations in a Karman Vortex Street by a vibrating cylinder', *Phys. Fluids* **8**(4), 760–761.

Weideman, J. A. and Reddy, S. C. (2000), 'A MATLAB differentiation matrix suite', *ACM Trans. Math. Softw.* **26**(4), 465–519.

White, C. M. and Mungal, M. G. (2008), 'Mechanics and prediction of turbulent drag reduction with polymer additives', *Annu. Rev. Fluid Mech.* **40**, 235–256.

Williams, J. E. F. and Zhao, B. C. (1989), 'The active control of vortex shedding', *J. Fluids Struct.* **3**(2), 115–122.

Yu, T. K. and Seinfeld, J. H. (1973), 'Observability and optimal measurement location in linear distributed parameter systems', *Int. J. Control* **18**(4), 785–799.

Zare, A., Jovanović, M. R. and Georgiou, T. T. (2017), 'Colour of turbulence', *J. Fluid Mech.* **812**, 636–680.

Zhou, K. and Doyle, J. C. (1998), *Essentials of robust control*, Vol. 104, Prentice hall Upper Saddle River, NJ.